



universität
wien

DIPLOMARBEIT

Titel der Diplomarbeit

Temperature dependence of heterogeneous nucleation.
Experiments on polar seed particles and nonpolar vapor.

angestrebter akademischer Grad

Magister der Naturwissenschaften (Mag. rer.nat.)

Verfasser:	Lukas Pichelstorfer
Matrikel-Nummer:	0508559
Studienrichtung:	411 Physik
Betreuer:	Ao. Univ.-Prof. Dr. h.c. Dr. Paul E. Wagner

Wien, am 15. Juli 2010

Ich möchte mich ganz besonders bei meinem Betreuer Prof. Paul Wagner für seine Unterstützung bedanken. Mein Dank gilt auch Dr. Paul Winkler und Dr. Aron Vrtala, die mir in vielen Belangen mit Rat zur Seite standen. Weiters darf ich mich bei meinen Kollegen Mag.a Tamara Pinterich, Dipl. Ing. Agnieszka Kupc, Mag. Gerhard Steiner, Johannes Bednar und Max Horejs für Ihre Hilfe bedanken. Besonderer Dank gebührt auch meiner Freundin Katharina Schabauer, die immer verständnisvoll war und mich stets bestärkt hat. Zuletzt möchte ich meinen Eltern Ilona und Gerhard Pichelstorfer dafür danken, dass Sie mich immer unterstützen und mir das Studieren ermöglicht haben.

Kurzfassung

In dieser Arbeit wurde die Temperaturabhängigkeit der Nukleation von n-Nonan Dampf an Natriumchlorid Teilchen untersucht. Nukleation ist ein statistischer Prozess, bei dem Teilchen aus der Dampfphase gebildet werden. Im Fall der heterogenen Nukleation bilden sich die Teilchen nicht spontan aus der Dampfphase, sondern mit Hilfe von sogenannten Kondensationskernen. Vorangegangene Experimente, durchgeführt von Schobesberger[42], welche sich auf die Temperaturabhängigkeit des Prozesses konzentriert haben, zeigten einen Temperaturtrend, der sowohl der Kelvin- als auch der Fletchertheorie widersprach. Die Aktivierung der Kondensationskerne findet laut Theorie für höhere Temperaturen bei niedrigeren Sättigungsverhältnissen statt. Um herauszufinden, ob dieser umgekehrte Temperaturtrend ein Kochsalzspezifischer Effekt ist, oder ob er auf elektrostatischer Wechselwirkung zwischen den Kondensationskernen und dem Dampf beruht (Schobesberger verwendete n-Propanol und Kochsalz, die beide polare Substanzen sind), wurde für diese Arbeit eine nicht polare Flüssigkeit verwendet.

Bei der Durchführung der Experimente wurde das n-Nonan verdampft, mit nahezu monodispersen NaCl Teilchen gemischt und in eine zylindrische Messkammer geleitet, welche durch ein Magnetventil mit einem Unterdruckbehälter verbunden war. Durch öffnen des Magnetventils wurde in der Messkammer ein adiabatischer Druckabfall erzeugt, der zu einem Anstieg des Sättigungsverhältnisses führte. Für ausreichend große Sättigungsverhältnisse bildeten sich n-Nonan Tröpfchen an den Kondensationskernen. Dieser Vorgang wurde mit Hilfe von monochromatischer Lichtstreuung untersucht.

Der Dampf wurde erzeugt, indem n-Nonan durch eine Mikrodüse geleitet wurde. Der auf diese Weise generierte Flüssigkeitsstrahl verdampfte in einem erhitzten Glaszylinder. Um die Nukleationskeime in der Größenordnung von einigen Nanometern zu erzeugen wurde Kochsalz in einem Rohrofen auf ca. 630°C erhitzt, was zur Folge hatte, dass eine nicht unwesentliche Anzahl von NaCl Molekülen den Kristall verlassen und eine breite Teilchenverteilung bildeten. Ein Elektrostatischer Klassifikator diente dazu, eine beinahe monodisperse Fraktion aus der Teilchenverteilung zu extrahieren. Die auf diese Weise klassifizierten Teilchen wurden mit dem Dampf vermischt und in den Size Analyzing Nucleus Counter (SANC) geleitet. Die Aerosolgenerierung ist empfindlich gegenüber Veränderungen der Masseflüsse. Kleine Schwankungen in Flüssigkeits- und Gasmasseflüssen können einen großen Einfluss auf den Nukleationsprozess haben.

Der SANC ist ein prozessgesteuertes Messsystem, in dessen Messkammer eine adiabatische Expansion stattfindet, wobei gleichzeitig Druck, Temperatur, gestreutes und transmittiertes Licht gemessen werden. Sind Temperatur, Druckabfall und die

genannten Masseflüsse bekannt, kann damit das Sättigungsverhältnis nach der Expansion berechnet werden. Die Messung von gestreutem und transmittiertem Licht kann, unter Verwendung der Constant Angle Mie Scattering (CAMS) Methode, welche auf der mathematischen Beschreibung der Streuung von ebenen Wellen an Sphären basiert, herangezogen werden, um Teilchenwachstum und Konzentration zu ermitteln. Der Vergleich von berechneten Wachstumskurven mit den experimentell ermittelten lässt auf die Aussagekraft des Experiments schließen.

In dieser Arbeit wurden Anzahlkonzentrationen aktivierter Teilchen gemessen. Durch Nukleation bildeten sich kritische Cluster an der Oberfläche der NaCl Teilchen, die in der Folge durch Kondensation zu sichtbarer Größe anwuchsen. Je größer das Sättigungsverhältnis ist, umso höher die Anzahl der aktivierten Teilchen. Da die Teilchenzahl in der Messkammer endlich ist, tritt ab einem gewissen Sättigungsverhältnis totale Aktivierung auf. Das Verhältnis von aktivierten zur gesamten Teilchenzahl wird als Aktivierungswahrscheinlichkeit bezeichnet. Die Abhängigkeit der Aktivierung des Sättigungsverhältnisses bei konstanter Temperatur darzustellen, war das Ziel der Messungen. Sie bildet den Ausgangspunkt für weitere Auswertungen der Daten.

Aktivierungswahrscheinlichkeitskurven wurden für drei verschiedene NaCl Teilchengrößen (7nm, 10nm und 15nm) und Temperaturen (-10°C , 0°C und $+10^{\circ}\text{C}$) ermittelt. Da diese Kurven sehr steil sind, war es vergleichsweise einfach jenes Sättigungsverhältnis zu ermitteln, bei dem 50% aller Teilchen aktiviert wurden, das sogenannte Onset Sättigungsverhältnis. Dieses zeigte, entgegen der theoretischen Vorhersage, basierend auf der klassischen Nukleationstheorie[7], keinen eindeutigen Temperaturtrend. Die Theorie sagt für größere Temperaturen kleinere Onset Sättigungsverhältnisse vorher, zudem waren die experimentell ermittelten Onset Sättigungsverhältnisse deutlich kleiner als die berechneten. Eine mögliche Erklärung dafür könnte die sogenannte Line Tension oder das Surface Diffusion Modell bieten, welche in der klassischen Nukleationstheorie vernachlässigt werden. Die Kelvin Gleichung gibt jene Oberflächenkrümmung eines Tröpfchens an, bei der dieses sich im thermischen Gleichgewicht mit seiner Umgebung befindet. Sie gibt einen Temperaturtrend vor, welcher auch experimentell gefunden werden konnte. Diese Untersuchungen legen nahe, dass die klassische Nukleationstheorie nicht alle Prozesse berücksichtigt, die zur Nukleation beitragen.

Abstract

In this work the temperature dependence of heterogeneous nucleation of n-nonane vapor on sodium chloride seed particles was investigated. Nucleation is a statistical process of particle production from the vapor phase. In the case of heterogeneous nucleation the particles do not form spontaneously from the vapor phase but with help of a so-called seed particle. Previous experiments by Schobesberger[42] focusing on the temperature dependence of the process have shown a temperature trend opposite to the one predicted by the Kelvin equation and the Fletcher theory. For higher temperatures the Kelvin equation predicts activation of the seed particles at lower vapor saturation ratios. To find out whether the above mentioned opposite temperature trend is due to some strange behavior of the seed particles or maybe based on electrostatic interaction(Schobesberger used n-propanol and sodium chloride which both are polar substances) a nonpolar liquid was chosen.

The experiments were carried out by evaporating the working fluid, mixing it with nearly monodisperse NaCl particles, passing the particle-vapor mixture on into a cylindrical measurement chamber which was connected to a vessel kept at lower pressure. Connecting the chamber to the vessel results in an adiabatic pressure drop within the chamber leading to a higher saturation ratio. If the saturation ratio is high enough liquid droplets will form on the seed particle surface. This process was observed by laser light scattering.

The vapor was produced by passing n-nonane liquid through a micro orifice. The liquid beam, which was generated this way, was evaporated in a heated glass cylinder. For seed particle production in the nanometer size range the sodium chloride was placed in a tube furnace. Heating it up to about $630^{\circ}C$ causes a considerable amount of salt molecules to leave the bulk crystal and form a broad particle size distribution. With help of an electrostatic classifier an almost monodisperse fraction was cut out of the particle distribution. The particles classified that way were mixed with the vapor and passed on to the the Size Analyzing Nucleus Counter (SANC). The aerosol production is sensitively dependent on the mass flows. Small uncertainties in the liquid or the gas mass flow may have great influence on the nucleation process.

The SANC is a process controlled measurement system, where an adiabatic pressure drop takes place within the measurement chamber. Simultaneously pressure, temperature and scattered as well as transmitted light are recorded. Measurement of pressure and temperature combined with the knowledge of the liquid and gas mass flows allows to determine the saturation ratio after the pressure drop. Scattered and transmitted light measurement is used to determine the particle growth

and concentration using the Constant Angle Mie Scattering (CAMS) method. The latter is based on the Mie theory which describes the scattering of light by spherical particles of known refractive index. Comparing droplet growth calculations to the experimental droplet growth provides information on the significance of the experiment.

In the present experiments the number of activated seed particles was measured. Due to nucleation critical clusters are formed at the surface of the seed particles. Subsequently, the seed particles grow by condensation to visible sizes. The higher the saturation ratio is the higher the number of activated particles. As the number of seed particles is finite total particle activation will occur above a certain saturation ratio. The ratio of activated over total particle concentration defines the activation probability. The aim of the measurements was to determine the dependence of activation probability on the saturation ratio which is also referred to as activation probability curve. Much effort was put on the attempt to measure the activation probability curves at constant temperature as it forms a basis for further evaluations.

Activation probability curves were determined for three different seed particle diameters (7nm, 10nm and 15nm) and temperatures ($-10^{\circ}C$, $0^{\circ}C$ and $+10^{\circ}C$). Since these curves are quite steep it is easy to determine the onset saturation ratio, at which 50% of all particles are activated. The experimentally determined onset saturation ratios for a given particle size did not show a clear temperature trend whereas theoretical calculations based on the classical nucleation theory[7] predict smaller onset saturation ratios for higher temperatures. Furthermore, experimental onset saturation ratios appear to be much smaller than the theoretical ones. Possible reasons could be the so-called line tension or the surface diffusion concept which both are not considered in the classical nucleation theory. The Kelvin equation that does not depend on concepts like line tension predicts the saturation ratio at which a cluster of given size is in thermodynamic equilibrium with the surrounding gas. It predicts a temperature trend which was also found by evaluating the experimental data of this work.

These observations seem to suggest that the classical nucleation theory does not consider all processes that play a role in heterogeneous nucleation.

Contents

1	Introduction	1
2	Theory of unary heterogeneous nucleation	3
2.1	Unary homogeneous nucleation	3
2.2	Unary heterogeneous nucleation	8
2.3	Nucleation theorem	11
2.3.1	Application of the nucleation theorem	13
2.4	Assessment of the kinetic factor	15
3	Experimental setup	18
3.1	The SANC (Size Analyzing Nuclei Counter)	18
3.2	The SANC cycle	19
3.3	The CAMS (Constant Angle Mie Scattering) Method	22
3.4	Setup of aerosol generation	24
3.5	Particle production and classification	25
3.5.1	NaCl particle production	26
3.5.2	Particle classification	28
3.6	Vapor Production	31
4	Investigation of NaCl particle shrinkage in n-Nonane vapor	34
4.1	Measurement technique and results	35
4.2	Interpretation	35
5	Investigation of the temperature dependence of heterogeneous nucleation of nonpolar n-Nonane on polar NaCl seed particles	41
5.1	Accomplishment of the experiment	42
5.1.1	Data acquisition	43

5.1.2	Data evaluation	43
5.2	Results	44
5.2.1	7nm seed particles	44
5.2.2	10nm seed particles	50
5.2.3	15nm seed particles	54
5.3	Data analysis	59
5.3.1	Kelvin curves	59
5.3.2	Towards the application of the heterogeneous nucleation theorem	59
5.3.3	Fletcher calculations	67
5.3.4	Possible influence of "line tension"	77
5.3.5	A further way of vapor deposition	77
6	Conclusion	79
6.1	Summary of achievements	79
6.2	Problems	80
6.3	Future investigations	81
	Bibliography	82
	List of Figures	87
	Appendix	92

1 Introduction

In a general sense this work deals with aerosols. According to Hinds[12] an aerosol is defined in its simplest form as solid or liquid particles suspended in a gas. It consists of two phases and its properties strongly depend on particle size and concentration. Its lifetime ranges from a few seconds up to months and years. The airborne particles are present throughout our environment. They come in many different forms, such as dusts, fumes, mists, smoke, smog or fog. These aerosols affect visibility, climate, and our health and quality of life[12]. There are many different sources: resuspended soil particles, salt particles from sea spray, smoke from power plants, traffic or wood fires and many more. Clouds of water droplets or ice crystals also belong to aerosols. The size range starts at about $0,001\mu m$ and goes up to $100\mu m$ and concentrations vary from $10^{-3}ccm^{-1}$ (in a cleanroom) up to $10^{11}ccm^{-1}$ (in a chemical reactor).

Why studying the properties of aerosols? A better understanding of the aerosol behavior would help to describe cloud formation which is inextricably linked to the water cycle and the earths radiation balance. Aerosols also have many commercial applications. Further, the toxicity of particles depend on their chemical and physical properties. Broad knowledge of these properties would help to estimate health hazards. But aerosols may also be helpful. Physicians for example use the aforementioned to treat diseases like respiratory ailments.

What do we have to take into account while studying aerosols? The airborne particles are affected by different kinds of chemical and physical processes. A molecule may react in the gas phase or impact on a particle or droplet surface where it may be reflected or get stuck to the surface where it might chemically react. Particles may coagulate, may grow by absorption, may be incorporated into water droplets[43]. There are many processes that have to be taken into account while investigating aerosols.

In this work the focus is put on nucleation. Clustering processes in the first-order phase play an important role in a huge variety of processes in nature, and in scientific and technological applications. Their adequate theoretical description is therefore of considerable interest[41]. There exist two different forms of nucleation, homogeneous and heterogeneous. The former generally requires quite high vapor pressures and is comparatively well understood. Whereas in heterogeneous nucleation vapor pressures slightly above the saturation vapor pressure might be enough to form a cluster from the vapor phase. Heterogeneous nucleation may occur on soluble or insoluble seed particles. The latter will be treated in this work. Clusters forming from the vapor phase by statistical collisions of single molecules have to pass a certain radius to be in thermodynamic balance with the surrounding gas. This radius is referred to as the critical radius and is determined by the Kelvin

equation[16]. The aforementioned is based on the fact that the vapor pressure over a curved surface is higher than over a flat surface. It is much easier, or statistically spoken probable, to form a critical cluster with help of a wettable seed particle than directly from the vapor phase.

Heterogeneous nucleation was initially described by Fletcher[7] in 1958. Fletcher did not account for all processes affecting the heterogeneous nucleation. Till now some modifications were made[21][11]. As there is not much experimental data available on heterogeneous nucleation the original theory, named the classical heterogeneous nucleation theory, could not be satisfyingly enhanced.

This work's focus is put on the temperature dependence of heterogeneous nucleation. An earlier work by Schobesberger[42] has shown a temperature dependence contrary to the one predicted by the Fletcher theory, where both seed particles and working fluid were chosen polar. To find out whether this difference between theory and experiment may be connected to electrostatic interaction between the vapor molecules and the seed particle surface, in this work the working fluid was chosen nonpolar.

Heterogeneous nucleation of n-nonane vapor on insoluble sodium chloride seed particles is investigated. Experiments are carried out for three different particle sizes(7nm, 10nm and 15nm) and nucleation temperatures($-10^{\circ}C$, $0^{\circ}C$ and $+10^{\circ}C$). The main goal of this study is to find out whether the contrary temperature effect also appears for a nonpolar working fluid. This would imply an effect on heterogeneous nucleation caused by the component's polarity.

2 Theory of unary heterogeneous nucleation

This chapter treats the classical unary nucleation of condensable vapor on spherical seed particles. Theoretically treating nucleation is of great importance for this work since it provides the possibility to compare and interpret the measured data. Nucleation is not solely a phenomenon occurring in the laboratory. It is in general an essential part of particle and droplet formation and growth. The nucleation process may be described as a phase transition condensable vapor undergoes. The vapor molecules directly build up liquid or solid clusters from the vapor phase. This process is driven by the vapor saturation ratio $S(T)$:

$$S(T) = \frac{p}{p_s(T)} \quad (2.1)$$

where p is the actual vapor pressure of the condensable vapor and $p_s(T)$ is the saturation vapor pressure which is strongly dependent on the temperature T . The saturation vapor pressure is the vapor pressure that builds up over a plain surface of the condensed matter(it may be liquid or solid) in thermal equilibrium. In such a system it makes no difference to the Gibbs free energy of the molecules wheter they are part of the bulk material or in the vapor phase.

Nucleation is not restricted to one kind of vapor(i.e. unary nucleation). It may also feature several types of vapor but since experiments carried out for this work use only one kind of vapor (n-nonane) this chapter deals only with unary nucleation. To facilitate introducing the basics the deliberations start with homogeneous nucleation

2.1 Unary homogeneous nucleation

To describe the physics of droplet formation and evaporation one certainly has to deal with description of phases, their changes as well as phase equilibrium. Formally this is can be realized by using the thermo dynamical free energy functions. Since many of the processes in aerosol physics take place under conditions of given pressure and temperatur it is reasonable to describe the system's state by means of the Gibbs free energy function G which is defined by [8]:

$$G = U - ST + pV \quad (2.2)$$

where U designates the internal energy of the system, S is its entropy, T its absolute temperature, p its pressure and V its volume. Changes in the system can be described using the differentiation of equation 2.2. Applying the first law of thermodynamics 2.3 leads, with the assumption of ideal gases, to equation 2.4.

$$dU = TdS - pdV \quad (2.3)$$

where T is the absolute temperature, p is the pressure. dU , dS and dV are the changes in internal energy, entropy and volume, respectively.

$$dG = -SdT + VdP \quad (2.4)$$

It has to be mentioned that this equation shows an extremum for a system in equilibrium at constant temperature and pressure. As a result the Gibbs free energy G is stationary. Further, it can be shown that the extremum of G actually is a minimum.

For a closed system(i.e. the number of particles remains constant) containing n phases the Gibbs free energy G can be written as the sum over all gibbs potentials μ_i of phase i times the number of molecules N_i in phase i :

$$G = \sum_{i=1, \dots, n} \mu_i N_i \quad (2.5)$$

A change in G can be achieved by molecules that swop into another phase of the system. For a system consisting of only two phases Π_l and Π_v (where l and v stand for liquid and vapor, respectively) the number of particles that leave phase Π_l is equal to the increase in particle number that phase Π_v undergoes. If the phases are in equilibrium then $dG = 0$ therefore also $(\mu_l - \mu_v) dN_l = 0$. As a result the chemical potential of the phases have to be equal:

$$\mu_v = \mu_l \quad (2.6)$$

This means that there is no net flux of molecules from one phase to the other.

If we consider an isothermal change of state of a system in equilibrium, this will also lead to a change in chemical potential $d\mu : \mu_l \rightarrow \mu_v$. Using equation 2.5, 2.4 and taking into account that the change is isothermal(i.e. $dT = 0$) we get:

$$d\mu_v = \frac{V}{N_v} dp \quad (2.7)$$

where dp is the change in pressure. Assuming the gas to be ideal and integrating the equation determines the difference of the chemical potentials before and after the isothermal change of state as:

$$\mu_v - \mu_l = k_B T \ln S \quad (2.8)$$

where μ_v and μ_l are the the chemical potentials before and after the change, k is the Boltzmann constant, T is the absolute temperature and $S := \frac{p_v}{p_l}$ is the saturation ratio.

Regarding equation 2.8 three different situations arise:

- The saturation ratio $S < 1$ which is tantamount to $\delta\mu < 0$. Therefore the vapor pressure p_v is bigger than the saturation vapor pressure p_l . In case of a system containing a liquid and a vapor phase molecules of the liquid would evaporate into the vapor phase. Thus the vapor pressure increases and the difference between the chemical potential of a molecule in the vapor and a molecule in the liquid decreases.
- For $\delta\mu = 0$ no net molecule flux between liquid and vapor phase occurs. The vapor pressures of both phases are equal.
- Of biggest interest relating to nucleation processes is the case where $S > 1$. The vapor pressure is bigger than the saturation vapor pressure which means that molecules are more likely to be in the liquid phase than in the vapor phase.

If there is no liquid phase and the saturation ratio $S > 1$ then a liquid phase may be developed by forming a molecule cluster. The Gibbs free energy of such a cluster is somewhat higher than the energy of i molecules in the liquid phase because of the cluster's surface A_i :

$$G_i = i\mu_l + A_i\sigma \quad (2.9)$$

The energy needed to directly form a cluster of i molecules from the vapor phase is given by:

$$\Delta G_i = G_i - i\mu_v \quad (2.10)$$

It is the Gibbs free energy of the cluster reduced by the energy the vapor molecules have. By inserting equation 2.9 and 2.8 the energy needed to form cluster of i molecules can be written as:

$$\Delta G_i = A_i\sigma - ik_B T \ln S \quad (2.11)$$

This equation shows a positive surface depending term competing with a volume depending term. Assuming a spherical cluster allows further deliberations. The surface A_i as well as the volume depending i can be replaced by terms depending on the cluster radius:

$$\Delta G_i = 4\pi r_i^2 \sigma - \frac{4\pi}{3} n_l r_i^3 k_B T \ln S \quad (2.12)$$

where n_l is the number of molecules per volume in the liquid phase. In Figure 2.1 the formation energy of a cluster ΔG_i is plotted against the cluster radius r_i for different saturation ratios S . As already mentioned there are two competing terms controlling the cluster's building process. The surface depending O_i is in

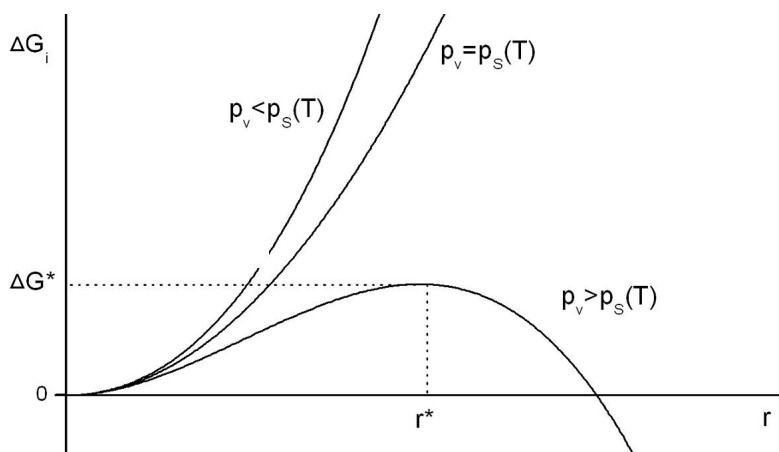


Figure 2.1: The formation energy ΔG_i as a functions of the cluster radius r for different saturation ratios.

proportion to r^2 whereas the volume depending Vol_i is in proportion to r^3 . For $S \leq 1$ ΔG_i is always positive since $Vol_i \leq 0$ which means that no cluster formation occurs or an existing cluster evaporates. If $S > 1$ the formation energy increases with particle radius due to the fact that $Vol_i > 0$ until it reaches at the critical radius r_i^* a critical value ΔG_i^* . For cluster radii exceeding the critical the formation energy starts to decline and as a result cluster growth occurs. To obtain the critical formation energy ΔG_i^* , formation energy is differentiated with respect to the cluster radius r . Setting $\frac{\partial \Delta G_i}{\partial r} = 0$ determines the critical radius r^* of a cluster:

$$r^* = \frac{2\sigma}{n_l k_B T \ln S} \quad (2.13)$$

This equation predicts the critical size of a cluster depending on surface tension, density per volume of the liquid, absolute temperature and the saturation ratio. A cluster of critical size r^* features a surface vapor pressure that is in equilibrium with the supersaturated surrounding. This equilibrium is quite unstable, though. If further vapor molecules are added to the cluster it will grow to bigger sizes. Droplet growth is solely stopped if the vapor molecules of the system are limited and therefore the saturation ratio in the system declines until a balance with the droplet has been achieved. In case that a single molecule leaves the critical cluster the vapor pressure on its surface will exceed the ambient vapor pressure and as a result the cluster will completely evaporate.

The saturation ratio S can also be expressed as a function of critical cluster curvature:

$$\ln S = \frac{2\sigma}{n_l k_B T r^*} \quad (2.14)$$

This equation is of great importance in nucleation and is referred to as Kelvin equation.

By applying the Kelvin equation to equation(2.12) of cluster formation energy ΔG^* can be expressed as function solely depending on surface tension σ and critical cluster radius r^* :

$$\Delta G^* = \frac{4\pi}{3}\sigma r^{*2} \quad (2.15)$$

The conditions under which a cluster may form have been explained. Now the question of formation rate arises: What is the number of clusters forming per unit time and volume that grow beyond critical size by the capture of vapor molecules? To treat this task particle kinetics have to be looked at. A system containing cluster concentrations n_i with $i = 1, \dots, g$ where i is the number of single molecules a cluster within n_i consists of is considered. Cluster growth or shrinkage is assumed to take place by adding and removing single monomers, respectively. This assumption is a good approach since the number of monomers is big compared to the number of clusters consisting of more than one molecule. For a stationary state of the system(Abraham [1] has calculated that a system featuring linear cluster kinetics reaches steady state within $\approx 10^{-6}$ seconds) the nucleation rate J can be written as:

$$J = c_i n_i - e_{i+1} n_{i+1} \quad (2.16)$$

where c_i is the capture rate and e_{i+1} is the escape rate of monomers of the related cluster concentration. A further assumption is made on the number concentration n_i . If the system is in equilibrium which is tantamount with $J = 0$ then the number concentration $n_i \rightarrow b_i$ and is Boltzmann distributed:

$$b_i = b_1 e^{-\frac{\Delta G_i}{k_B T}} \quad (2.17)$$

By applying this equation to the nucleation rate J and under consideration of the fact that $c_i b_i = e_{i+1} b_{i+1}$ one can write[8]:

$$J = K' e^{-\frac{\Delta G^*}{k_B T}} \quad (2.18)$$

where K' contains details on particle kinetics. The nucleation rate J represents the number of clusters growing beyond the critical size per time(s) and volume(cc). Since nucleation requires big amounts of monomers J is either strongly limited in time or nucleation takes place slowly enough that additional monomers can be provided. By applying equation 2.15 and 2.13 to equation 2.18 it turns out that the nucleation rate J strongly depends on the liquid surface tension, the temperature and the saturation ratio. Small fluctuations in this quantities yield to huge uncertainties of the nucleation rate.

2.2 Unary heterogeneous nucleation

Nucleation doesn't have to be homogeneous. Actually, it requires quite high saturation ratios to show appreciable nucleation rates. In case of water vapor at 273K and a saturation ratio of $S = 3$ approximately $2 * 10^{-17}$ particles exceed the critical radius per second and cubic centimeter. If for example homogeneous nucleation would be the only way to form clusters and droplets there would not be any precipitation at all. There is the possibility of nucleation rates several orders of magnitudes higher and at lower saturation ratios if nucleation takes place heterogeneously. Therefore the cluster which is referred to as embryo builds up on a preexisting particle, the so-called "seed particle". The principles of heterogeneous nucleation are schematically depicted in figure 2.2. The Gibbs free energy of an

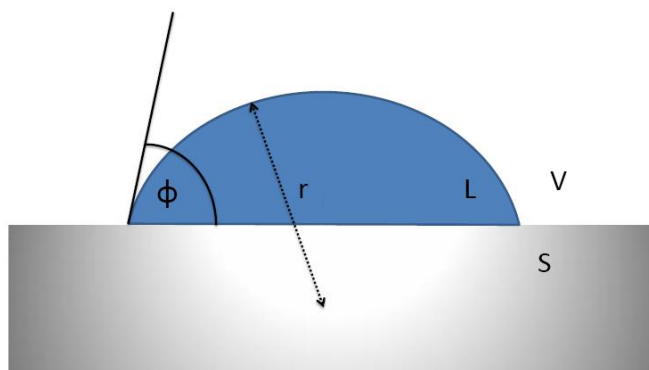


Figure 2.2: Depicts a three phase system: the vapor phase V, the solid phase S and the liquid phase L which is in fact the cap embryo. r is the radius implied by the surface curvature of the embryo and Φ denotes the contact angle between the solid and the liquid phase.

embryo can be expressed by:

$$G = i\mu_v - A_{lv}\sigma_{lv} + A_{ls}\sigma_{ls} \quad (2.19)$$

where A_{lv} , A_{ls} are the interfaces delimiting the liquid and the vapor phase, the liquid and the solid phase, respectively and σ_{jk} is the surface tension two phases j and k feature. The embryo forming on the particle removes some of the surface separating the solid and the vapor phase. The energy difference occurring during this process is now available to the embryo. Its formation energy can be written as:

$$\Delta G_i = G_i - i\mu_v - A_{sl}\sigma_{sv} \quad (2.20)$$

which by considering the Gibbs free energy and inserting equation 2.8 can be written as:

$$\Delta G_i = A_{lv}\sigma_{lv} - A_{sl}(\sigma_{sv} - \sigma_{sl}) - ik_B T \ln S \quad (2.21)$$

Since the surface tension between the solid and the vapor or the liquid phase is not easily determined the term $(\sigma_{sv} - \sigma_{sl})$ is to be replaced. At the triple line separating the three phases there has to be a mechanical equilibrium of the surface tensions. Therefore the components of the surface tension parallel to the solid plane are considered leading to *Young's law*:

$$\cos\Phi = \frac{\sigma_{sv} - \sigma_{sl}}{\sigma_{lv}} =: m \quad (2.22)$$

For a spherical cap embryo on a plane surface the formation energy is a function of r and Φ . By differentiating the formation energy $\Delta G_i(r, \Phi)$ with respect to radius r and setting $\frac{\partial \Delta G_i(r, \Phi)}{\partial r} = 0$ the critical embryo radius is obtained:

$$r^* = \frac{2\sigma}{n_l k_B T \ln S} \quad (2.23)$$

The critical radius is equal to the one obtained in case of homogeneous nucleation (see equation 2.13) since the curvature of the critical embryo or cluster is determined by the fact that the vapor pressure upon the liquid surface has to be in equilibrium with the ambient.

For the determination of the critical embryo formation energy the atmospherically more relevant case of heterogeneous nucleation upon a spherical seed particle is considered. Figure 2.3 schematically outlines the situation. The surface be-

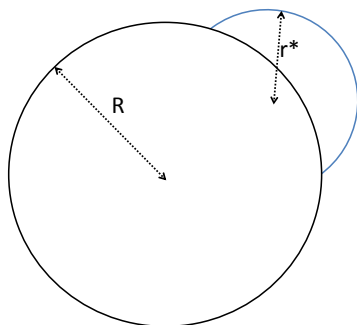


Figure 2.3: R is the radius for the spherical seed particle and r^* is the radius of the spherical cap embryo of critical size.

tween the solid and the liquid phase A_{sl} can be written as function of $x := \frac{R}{r^*}$

and m . Further, the contact area of the liquid and the vapor phase is given by $A_{lv} = 2\pi r^2(1 - m)$. Once again the function describing the formation work is deviated with respect to r and set to zero. One obtains the critical formation energy of an spherical cap embryo[8]:

$$\Delta G^* = \frac{4\pi}{3}\sigma_{lv}r^{*2}f(m, x) \quad (2.24)$$

where

$$2f(m, x) = 1 + \left(\frac{1 - mx}{g}\right)^3 + x^3 \left(2 - 3\left(\frac{x - m}{g}\right) + \left(\frac{x - m}{g}\right)^3\right) + 3mx^2 \left(\frac{x - m}{g} - 1\right) \quad (2.25)$$

with

$$g = \sqrt{1 + x^2 - 2mx} \quad (2.26)$$

For big contact angles ($m \rightarrow -1$) the function $f \rightarrow 1$ which means that heterogeneous nucleation approaches to homogeneous. Whereas for small contact angles Φ , especially if the seed particle radius R is smaller than the critical radius r^* , the formation energy of a critical embryo can be reduced significantly.

As in section 2.1 the question of the nucleation rate arises. For this purpose it is assumed that every seed particle serves for only one critical cluster. Further, the nucleation rate J_{het} does not give the rate of critical clusters forming per cm^3 (as in equation 2.18) but per cm^2 (area of the seed particles):

$$J_{het} = K'' e^{-\frac{\Delta G^*}{k_B T}} \quad (2.27)$$

where K'' includes the kinetics of the vapor molecules.

Since the heterogeneous nucleation rate is a quantity which is not easy to determine experimentally, the activation probability P_{act} is introduced:

$$P_{act} = \frac{N_{act}}{N_{inact}} \quad (2.28)$$

where N_{act} and N_{inact} is the number of seed particles per cc activated or not activated, respectively. The dependence of the heterogeneous nucleation rate J_{het} on the activation probability is given by:

$$dN_{inact} = -dN_{act} = -J_{het}AN_{inact}dt \quad (2.29)$$

The change of activated particles dN_{act} (which is in fact the negative change of inactivated particles dN_{inact}) is equal to the heterogeneous nucleation rate per seed particle $J_{het}A$ times the number of inactivated seed particles and the change in time dt . By integration J_{het} can be written as:

$$J_{het} = \frac{1}{A\Delta t} \ln \frac{1}{1 - P} \quad (2.30)$$

Δt denotes the nucleation time is typically short.

2.3 Nucleation theorem

The nucleation theorem allows the determination of the number of molecules in a critical cluster from the critical cluster formation work and in the sequel from the nucleation rate. There exists a thermodynamic relation between these quantities which is to be proved in this section. An important feature of the nucleation theorem is that its general form is independent of the nucleation model.

As it is known from section 2.1 the critical formation work ΔG^* of a spherical cluster homogeneously formed from the vapor phase can be written as:

$$\Delta G^* = \frac{4\pi}{3}\sigma r^{*2} \quad (2.31)$$

where the critical cluster radius r^* is given as:

$$r^* = \frac{2\sigma}{n_l k_B T \ln S} \quad (2.32)$$

where σ denotes the nucleus specific surface free energy, n_l is the number of vapor molecules per volume within the liquid, k_B is the Boltzmann constant and S the saturation ratio. For further details on these quantities see section 2.1. Using equation 2.8 and the fact that the number of molecules i within a sphere of volume V , radius r and molecule number density n_l is $i = n_l V = \frac{4\pi}{3}n_l r^3$ the critical formation work is transformed to:

$$\Delta G^* = \frac{1}{2}i^* \Delta\mu \quad (2.33)$$

with

$$i^* = \frac{32\pi\sigma^3}{3n_l^2 \Delta\mu^3} \quad (2.34)$$

It is easily proved that:

$$\frac{d\Delta G^*}{d\Delta\mu} = -i^* \quad (2.35)$$

which is a form of the nucleation theorem derived from the case of homogeneous nucleation. Nielson[28] who worked on classical nucleation from solutions also derived this equation. Equation 2.35 is apart of an additional term which can often be neglected already the general relation between ΔG^* and i^* . General means that it can be applied to all different kinds of nucleation models(classical[44], atomistic[26] or other).

To find the general form of the nucleation theorem let us consider the formation work of a cluster consisting of i molecules. It is the change of free energy within the system which happens when a cluster forms. In section 2.1 and section 2.2 this change in free energy has already been expressed for the homogeneous and

the heterogeneous case, respectively. The most general form of the formation work $\Delta G(i, \Delta\mu)$ is:

$$\Delta G(i, \Delta\mu) = -i\Delta\mu + F(i, \Delta\mu) \quad (2.36)$$

for $i > 1$ and $\Delta\mu > 0$. The right hand side of the equation features two terms that can practically be interpreted. The first term $-i\Delta\mu$ expresses the change in free energy that i molecules undergo when changing from the vapor phase into the liquid phase without taking into account the surface energy. The second term on the right hand side $F(i, \Delta\mu)$ is the so-called excess free energy of the cluster. Primarily it includes the enhancement of the cluster's free energy due to the creation of the surface. It may also feature further terms taking into account pressure or volume changes in the system. At the moment the actual form of F does not matter at all since the general form of the excess free energy can be determined from the formation work without knowing i or the $\Delta\mu$ dependence of F . The excess free energy may even remain a totally unknown function.

If the critical formation work ΔG^* and the excess free energy F are differentiable functions with respect to $\Delta\mu$ the nucleation theorem can be obtained by the differentiation of ΔG^* with respect to $\Delta\mu$:

$$\frac{d\Delta G^*}{d\Delta\mu} = -\frac{d[i^*(\Delta\mu)\Delta\mu]}{d\Delta\mu} + \frac{dF^*(i^*, \Delta\mu)}{d\Delta\mu} \quad (2.37)$$

where

$$\frac{d[i^*(\Delta\mu)\Delta\mu]}{d\Delta\mu} = i^* + \Delta\mu \frac{di^*}{d\Delta\mu} \quad (2.38)$$

$$\frac{dF^*(i^*, \Delta\mu)}{d\Delta\mu} = \frac{\delta F^*}{\delta \Delta\mu} + \frac{\delta F^*}{\delta \Delta\mu} \frac{di^*}{d\Delta\mu} \quad (2.39)$$

leading to:

$$\frac{d\Delta G^*}{d\Delta\mu} = -i^* - \left(\Delta\mu - \frac{\delta F^*}{\delta i^*} \right) \frac{di^*}{d\Delta\mu} + \frac{\delta F^*}{\delta \Delta\mu}. \quad (2.40)$$

Here the physical stepwise variable i^* which is the number of molecules in the critical cluster was assumed to be continuous. To remember: in section 2.1 and 2.2 the critical cluster formation work was derived by setting the differentiation of the formation work with respect to the cluster radius equal to zero: $\left(\frac{\delta \Delta G}{\delta r} \right)_{r=r^*} = 0$. Since the cluster radius r is proportional to the number of molecules i in the cluster the critical formation work can also be determined by the differentiation of ΔG with respect to i : $\left(\frac{\delta \Delta G}{\delta i} \right)_{i=i^*} = 0$. Applying these deliberations to equation 2.36 leads to:

$$\Delta\mu - \left(\frac{\delta F}{\delta i} \right)_{i=i^*} = 0 \quad (2.41)$$

which allows to eliminate the $(\Delta\mu - \frac{\delta F^*}{\delta i^*}) \frac{di^*}{d\Delta\mu}$ term in equation 2.40 bringing the nucleation theorem into a rather compact form:

$$\frac{d\Delta G^*}{d\Delta\mu} = -i^* + \frac{\delta F^*}{\delta \Delta\mu}. \quad (2.42)$$

This equation depicts the direct relation between nucleation work, nucleus size and as will be shown nucleation rate. In many cases the excess free energy of the cluster is negligibly dependent or even independent of $\Delta\mu$ which further simplifies the theorem.

2.3.1 Application of the nucleation theorem

As already stated in section 2.1 and 2.2 the nucleation rate J can be written as:

$$J = K e^{-\frac{\Delta G^*}{k_B T}} \quad (2.43)$$

where K includes besides others the kinetics of the vapor molecules. Simple transformation of this equation makes it possible to express the critical formation rate ΔG^* as an explicit function of the nucleation rate J :

$$\Delta G^* = k_B T \ln K - k_B T \ln J \quad (2.44)$$

Applying this function to equation 2.42 allows the determination of the number of molecules in the critical cluster as a function of the nucleation rate:

$$i^* = \frac{d(k_B T \ln J)}{d\Delta\mu} - \frac{d(k_B T \ln K)}{d\Delta\mu} + \frac{\delta F^*}{\delta \Delta\mu} \quad (2.45)$$

which is further simplified if the excess free energy is not $\Delta\mu$ dependent:

$$i^* = \frac{d(k_B T \ln J)}{d\Delta\mu} - \frac{d(k_B T \ln K)}{d\Delta\mu} \quad (2.46)$$

These considerations are still general and can be applied to all kinds of nucleation models (atomistic, homogeneous, heterogeneous etc.).

In the case that the formation work of the cluster features not only an excess free energy which is independent of $\Delta\mu$ but also a $\Delta\mu$ independent T and K the number of molecules in the critical cluster can be determined from the slope of a $k_B T \ln J$ vs. $\Delta\mu$ curve. This means that every point of the curve represents the critical nucleus size at given $\Delta\mu$. For a more accurate determination of i^* all terms of equation 2.45 have to be taken into account.

Monte Carlo simulations showing the applicability of the equations recently derived were carried out by Weeks and Gilmer[56]. Two-dimensional nucleation on a

perfect (100) crystal face was observed and showed good accordance to theory[15] where the excess free energy was virtually independent of $\Delta\mu$ and the kinetic factor was: $K = C_0 S$ with the saturation ratio $S = e^{\frac{\Delta\mu}{k_B T}}$. As a result the number of molecules in the critical cluster could be determined as $i^* = \frac{k_B T d \ln J}{d \Delta\mu} - 1$. Since a general form of the nucleation theorem was found some particular cases are to be looked at:

- Classical homogeneous nucleation in vapors
- Classical heterogeneous nucleation in vapors

In the case of classical homogeneous nucleation the kinetic factor K'' can be written as $K'' = C_0 S^2$ [15] where C_0 is independent of $\Delta\mu$. The excess free energy of a homogeneously formed cluster is $F = 4\pi r^2 \sigma$ or in terms of n where $n = n_l V = \frac{4\pi}{3} r^3 n_l \rightarrow F = \left(\frac{36\pi^2}{n_l}\right)^{\frac{1}{3}} n^{\frac{2}{3}} \sigma$. The surface free energy σ is regarded as $\Delta\mu$ independent and as a result equation 2.46 can be applied to calculate the critical cluster size:

$$i^* = \frac{k_B T d \ln J}{d \Delta\mu} - \frac{k_B T d \ln K}{d \Delta\mu} \quad (2.47)$$

The differentiation of the kinetic factor is done by introducing a new variable $x = \frac{\Delta\mu}{k_B T}$, $d\Delta\mu \rightarrow \frac{dx}{k_B T}$. The i^* of a classical homogeneously formed cluster finally determines as:

$$i^* = \frac{k_B T d \ln J}{d \Delta\mu} - 2 \quad (2.48)$$

The case of classical heterogeneous nucleation can be treated analogously to the one of classical homogeneous nucleation. For a three dimensional cap-shaped embryo on a spherical seed particle the kinetic factor K' can be expressed as $C_2 S$ [44]. The excess free energy of the embryo is a function of the contact angle, the surface free energy and the ratio of embryo radius and seed particle radius: $F(\Phi, \sigma, \frac{r}{R})$ [44]. Again, all these quantities are treated as $\Delta\mu$ independent. Equal to the case of homogeneous nucleation the kinetic factor is differentiated. Finally, i^* of a classical heterogeneously formed cap-shaped cluster is found as:

$$i^* = \frac{k_B T d \ln J}{d \Delta\mu} - 1 \quad (2.49)$$

In this work the dependence of the critical number of molecules on the nucleation probability P_{act} (see section 2.2) is of bigger interest since it is experimentally obtained, whereas nucleation rates would have to be calculated. The correlation between the nucleation probability and the nucleation rate is given by equation

2.30. To receive i^* as a function of P_{act} let us first consider the logarithm of the nucleation rate in terms of P_{act} :

$$\ln J = \ln \frac{1}{A\Delta t} + \ln \ln \frac{1}{1 - P_{act}} \quad (2.50)$$

The logarithmic nucleation rate can be expressed as a sum of two terms. The first one contains the seed particle surface A and the nucleation time Δt that are $\Delta\mu$ independent $\Rightarrow \frac{d \ln \frac{1}{A\Delta t}}{d\Delta\mu} = 0$ leaving i^* as:

$$i_{het}^* = k_B T \frac{d \left(\ln \ln \frac{1}{1 - P_{act}} \right)}{d\Delta\mu} - 1 \quad (2.51)$$

It is to mention that although the number of molecules within a cluster is treated as a continuous function equation 2.42 is also valid for a stepwise i since it may also be derived from the atomistic model where solely discrete changes of i are possible.

However, there is a fundamental problem with the comparison of experimental data with theoretical calculations: The equations used to determine e.g. the critical cluster radius or the number of molecules in the critical cluster use macroscopic thermodynamic quantities like the liquid density, the surface tension or the vapor pressure. Actually the clusters describe by these equations may contain only of a few molecules. It is doubtful if a liquid-cluster in the nanometer scale is properly described using macroscopic quantities. This may lead to considerable differences between calculations and experimental data.

2.4 Assessment of the kinetic factor

As shown in section 2.2 the heterogeneous nucleation rate can be written as:

$$J_{het} = K e^{-\frac{\Delta G^*}{k_B T}} \quad (2.52)$$

For information on the term $e^{-\frac{\Delta G^*}{k_B T}}$ see section 2.2. In this section a useful form of the kinetic factor K is to be derived. According to Stauffer[45] the kinetic coefficient is determined as:

$$K = R_{av} F Z \quad (2.53)$$

where R_{av} is the average condensation rate, Z is the Zeldovich factor and the meaning of F differs for various nucleation models. In case of homogeneous nucleation it would be the number of vapor molecules in the system or in case of ion induced nucleation it would be the total number of ions. In case of unary heterogeneous nucleation it can be approximated as the total number of vapor molecules adsorbed

per unit surface of the seed particle N_{ads} (i.e. the surface concentration)[46]. Accurate expressions for R_{av} and Z include second derivatives of the formation energy with respect to the total number of vapor molecules in the heterogeneous cluster. Approximations which turned out to be quite good make it possible to avoid the derivations of the formation energy[46]:

$$R_{av} = \frac{\beta_1\beta_2}{\beta_1\sin^2\Upsilon + \beta_2\cos^2\Upsilon} \quad (2.54)$$

where β_i are the rates of monomer collision of species i on the cluster and Υ is the direction angle of the growth vector. This expression is still accurate. Under the assumption that:

$$\Upsilon = \arctan\frac{x}{1-x} \quad (2.55)$$

where x is the mol fraction of species i and for unary heterogeneous nucleation R_{av} reduces to:

$$R_{av} = \beta \quad (2.56)$$

There are two commonly used approaches to describe β [46]:

- The direct vapor deposition approach
- The surface diffusion approach

The former takes into account the vapor molecules colliding directly with the cluster. It is also the one that is used for calculations in this work. This allows to express β which is also referred to as growth rate as:

$$\beta = \frac{SA_{lv}p_S}{\sqrt{2\pi mk_B T}} \quad (2.57)$$

where A_{lv} is the interface between the liquid cluster and the vapor[7], p_S is the vapor pressure, m is the mass of a single molecule, k is the Boltzmann constant and T is the temperature.

The accurate expression of the Zeldovich factor Z is also Υ dependent[46]. An approximation is given by the factor of the homogeneous case:

$$Z = \sqrt{\frac{\sigma}{k_B T}} \frac{v}{2\pi r^{*2}} \quad (2.58)$$

where σ is the surface tension of the condensed vapor molecules, v is the volume of a single molecule and r^* is the critical radius(see equation 2.13).

Assuming a steady state between the incoming and outgoing molecules the surface concentration for unary nucleation is determined by[58]:

$$N_{ads} = \frac{Sp_S}{\sqrt{2\pi mk_B T}} \frac{1}{\nu} e^{\frac{L}{k_B T}} \quad (2.59)$$

where S is the saturation ratio, ν is the vibration frequency of a molecule on the surface and L is the latent heat of vaporization per vapor molecule. To calculate the vibration between two molecules the nearest neighbor interaction is treated using the harmonic oscillator model[21]:

$$\omega = 2\pi\nu = \sqrt{\left(\frac{d^2U}{dr^2}\right)_{r=r_0} \frac{1}{m_\mu}} \quad (2.60)$$

where ω is the angular frequency, $\left(\frac{d^2U}{dr^2}\right)_{r=r_0}$ is the second derivative of the molecule potential at the distance of balance and m_μ is the reduced mass of the two molecules.

In this section an approximation of the kinetic factor K was derived. It is dependent on various thermodynamic quantities but may be obtained without excessive theoretical calculations. Further, results derived by using the approximation do not differ much from the values calculated with the accurate expression[46].

3 Experimental setup

The experimental setup includes a generator of a monodisperse aerosol and the so-called SANC (Size Analyzing Nuclei Counter). Aerosol production is accomplished by generating monodisperse sodium chloride particles (see section 3.5) which are combined with a well defined mixture of carrier gas and vapor (see section 3.6). Actually the SANC system serves as an expansion type condensation nucleus counter (CNC) which works under very well defined conditions. Monitoring the total aerosol number concentration down to the smallest detectable size is what a CNC provides. Within the CNC particles are grown by a factor up to 1000 and more until they are large enough to be detected by optical means[24].

Sizes down to a diameter of $10^{-9}m$ are detectable with the experimental device used in this work[57].

The original expansion type CNC was built by Aitken in the 19th century and involved a microscope to count the particles directly[2]. It's all water under the bridge. The SANC today is an indirect measurement instrument which means that particle number concentration is determined by evaluating the scattered as well as the attenuated light flux through the expansion chamber.

3.1 The SANC (Size Analyzing Nuclei Counter)

The heart of the SANC is a cylindrical chamber with a diameter of 5cm and a volume of $130cm^3$ where droplet growth is investigated by means of light scattering. This brazen chamber has an aerosol in- and outlet, four glass windows needed for the optics, two connections for cooling liquid, one for a Pt100 temperature sensor and one for a pressure sensor.

The aerosol flow through the chamber is remote controlled by a PC and described in detail in section 3.2.

A perpendicular polarized monochromatic light beam produced by a helium-neon laser enters the chamber through one of the glass windows. On the opposite side of the chamber another window is located where the attenuated light flux is measured. At an angle of 15^0 compared to the transmitted light there is a further window where the scattered light flux is measured. These three windows are essential, the additional fourth is integrated for illustration. It remains covered during the measurement. The beam path is illustrated in figure 3.2. The optics include amongst others a photomultiplier (PM) and a photodiode (PD) to measure the light intensity of scattered and transmitted light which yield to the particle concentration as well as to the speed of particle growth as explained in section 3.3.

Cooling or heating of the chamber is accomplished by a thermostat (RMS, Lauda) and monitored by a PREMA 3040 precision thermometer in combination with a Pt100 temperature sensor. It turned out that the temperature of the chamber is

kept quite stable throughout a measurement by the thermostat. Variation of the chamber temperature of more than 0.05K were unusual.

To perform an adiabatic pressure drop the inner pressure of a large vessel, compared to the chamber size, is set below the ambient by using a vacuum pump (RTV 2 DV, Rietschle). This vessel is connected to the chamber via a magnetic valve as figure 3.1 illustrates. When the magnetic valve opens the pressure in the chamber drops within some milliseconds and is monitored by amplifying the electric signal of a piezo pressure sensor installed in the chamber. The expansion is fast enough to be treated as adiabatic. Therefore the temperature after the expansion can be obtained by applying Poisson's law:

$$T_0 = \frac{T_1}{\left(\frac{p_1}{p_0}\right)^{\frac{\kappa-1}{\kappa}}} \quad (3.1)$$

The temperature T_1 and T_0 are the temperatures before and after the expansion, p_1 and p_2 are the total pressures before and after the expansion which are received by measuring the ambient air pressure as well as the pressure drop in the chamber. The adiabatic exponent κ for the gas-vapor mixture is given by the Richarz formula[36]:

$$\kappa = 1 + \left[\frac{1}{\kappa_g - 1} + \frac{p_v}{p} \left(\frac{1}{\kappa_v - 1} - \frac{1}{\kappa_g - 1} \right) \right]^{-1} \quad (3.2)$$

where κ_g is the adiabatic exponent of the carrier gas and κ_v is the vapor's adiabatic exponent. The total gas pressure is given by p and the vapor pressure by p_v .

The supersaturation can be calculated by:

$$S(T) = \frac{p_v}{p_s(T)} \quad (3.3)$$

where p_v is the partial vapor pressure and p_s is the saturation vapor pressure which strongly depends on the temperature as equation 3.4 depicts:

$$p_s(T_0) = \exp\left(A_1 - \frac{A_2}{T_0 - A_3} - A_4 \ln T_0 + A_5 T_0\right) \quad (3.4)$$

The coefficients A_1 to A_5 differ from vapor to vapor and can be obtained from literature.

3.2 The SANC cycle

The SANC cycle is remote controlled by the software program Acquire[23] developed by Aron Vrtala. It is run on an Intel 80486 PC system. The cycle consists of six consecutive "phases". Each characterized by the magnetic valves that are

open and closed respectively. The task of the cycle is to provide different pathways for the incoming aerosol through the measurement system by controlling the magnetic valves V1 to V6 (depicted in figure 3.1) and setting the pressure in the underpressure vessel R to the desired value. To observe well defined conditions it is important to have a steady aerosol flow through the system throughout the whole cycle. Consequently a new way through the system is provided before the preceding one is closed by a magnetic valve.

The first phase is the so-called "flushing" phase during which the magnetic valves V1, V3 and V6 are open. In this part of the cycle the underpressure builds up in the underpressure vessel R. The pressure difference between the inside of the vessel and the ambient air pressure is controlled by Acquire via a remote controlled butterfly valve and the differential pressure gauge shown in figure 3.1. It was varied in the range of 50mbar to 320mbar. Further the "flushing" phase serves to flush the chamber after an expansion event. There exists a rough-and-ready rule that demands to flush the chamber with a gas volume at least seven times its own volume. By a vacuum pump and a upstream critical orifice the flow was kept at $7,5\text{ l/min}$ throughout all expansion measurements of this work. The volume of the chamber is 130 cm^3 . This requires a flushing time of at least 7,3 seconds. Due to the shape of the chamber which cannot be seen as perfect for flushing and to be save the duration of this phase was set to 20 seconds in most cases. For high saturation ratios of the incoming aerosol, this means $S(T)$ bigger than 0.7, it was increased up to 45 seconds. During the next phase, which is called "delay", magnetic valves V1, V4 and V6 are left open. Corrections of the pressure in the vessel are still possible because V6 is still open. The aerosol is already situated in the chamber which usually has another temperature than the one of the incoming aerosol. For chamber temperatures below or above the aerosol's temperature the volume of the gas will decrease or increase respectively. Consequently conditions are not well defined any more. Leaving V1 open in this phase allows the gas to reach thermal equilibrium with the chamber while keeping the pressure constant. For first measurements this phase lasted for 20 seconds but it appeared that it was not enough in most cases. Therefore the duration was increased to at least 40 seconds up to 70 seconds depending on the temperature difference between the incoming aerosol and the chamber. The "pause" phase is very short. It lasts for 1 second and leaves only the magnetic valve V4 open. Pressure monitoring starts. The next step called "expansion" additionally opens the valve V2 and therefore connects the chamber to the underpressure vessel R. The adiabatic expansion takes place. Pressure drop and scattered light as well as transmitted light are measured. In the "pressure adjust" phase valves V4, V5 and V6 are open and ambient air pressure is restored within the chamber. The last step of the cycle the so-called "reset" phase leaves the valves V1, V4 and V6 open and prepares the system to start again with "flush-

ing". Running through the whole cycle once leads to a so-called "shot" which is a set of data containing the pressure drop, the scattered as well as the transmitted light through the chamber recorded during the adiabatic expansion. The cycle is described in detail in[29].

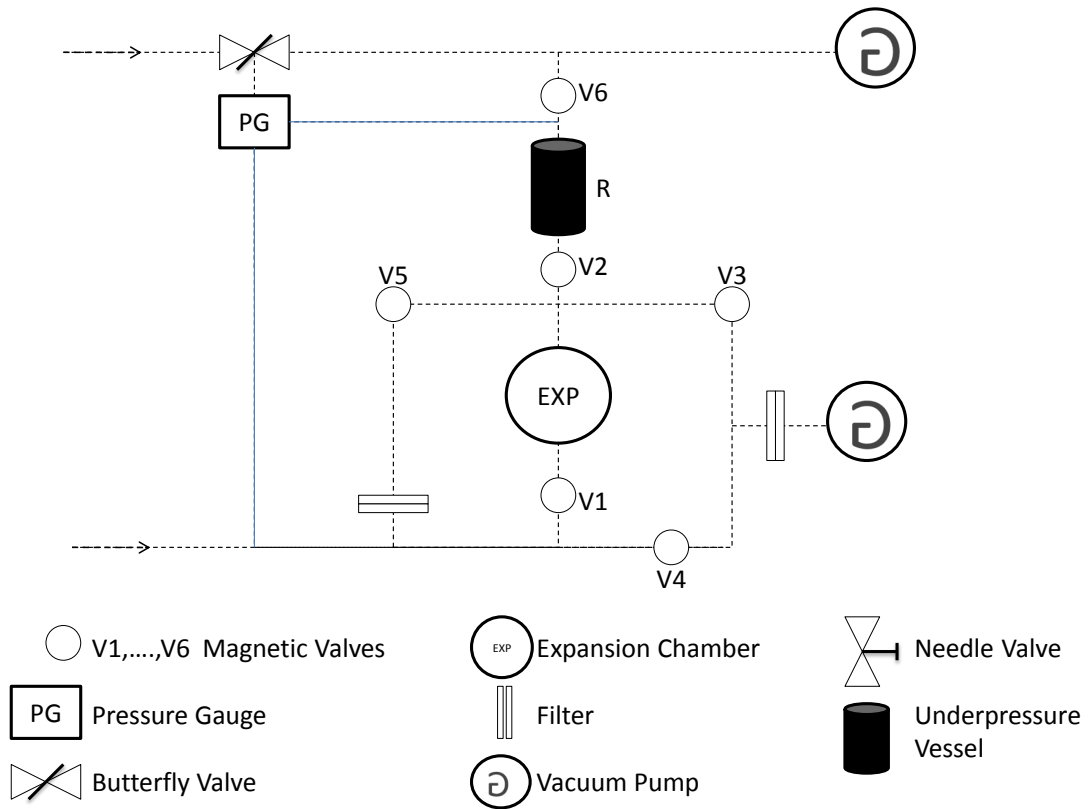


Figure 3.1: The SANC Cycle

3.3 The CAMS (Constant Angle Mie Scattering) Method

The CAMS method allows to investigate the droplet growth as well as the particle number concentration of colloidal systems by measuring the scattered and the attenuated light flux through a cylindrical chamber. The scattered light flux is measured at a constant angle to the attenuated light flux. It requires a system of approximately monodisperse and spherical particles that are not strongly absorbing.

Figure 3.2 depicts the light path through the chamber. A He-Ne laser (LGK 7628,

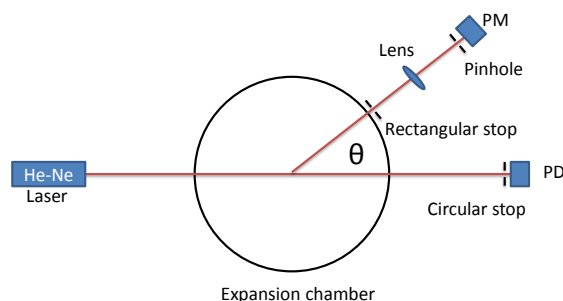


Figure 3.2: Light path through the chamber

Siemens) produces a beam of monochromatic light (wavelength $\lambda = 633nm$) that further is polarized perpendicular to the scattering plane. During the growth process of the droplets within the chamber the attenuated light flux is measured by a photodiode (PD). At the same time also the scattered light flux under a selectable constant angle Θ (it was kept at 15° throughout this work) is monitored by a photomultiplier (PM). From these two quantities the particle number concentration and the droplet size are determined.

The intersection of the laser beam and the observation cone of the photomultiplier which is set by the rectangular stop (shown in figure 3.2) determines the scattering volume. The intensity of the light flux scattered by every single particle within this volume is limited by a pinhole preceding the photomultiplier. The transmitted light flux is reduced by a circular stop.

During the droplet growth process the transmitted light flux decreases because of

extinction. Also the scattered light flux suffers from extinction. The more particles there are in the chamber and the bigger they grow the higher the light flux removed by extinction gets. If the particle concentration was obtained from merely measuring the scattered light the extinction would lead to a smaller concentration than the actual since the concentration is calculated using the height of the scattered light extremes. Due to the fact that the scattering volume is located in the middle of a cylindrical chamber the same percentage of the intensity of scattered and transmitted light is removed by extinction. Using Beer Lambert's law[12] extinction can be calculated:

$$\Phi_{trans} = \Phi_0 e^{-\sigma_{ext} x} \quad (3.5)$$

where Φ_{trans} is the transmitted light flux, Φ_0 is the incident light flux, x is the thickness of the scattering medium and σ is the extinction coefficient. In the case of spherical monodisperse particles the extinction coefficient can be written as[48]

$$\sigma_{ext} = \frac{\pi D_p^2}{4} N Q_{ext}(\xi, m) \quad (3.6)$$

where D_p is the particle diameter, N is the number concentration and $Q_{ext}(\xi, m)$ is the extinction efficiency factor depending on refractive index m and the size parameter $\xi = \frac{\pi D_p}{\gamma}$. γ is the wavelength of the incident light. The chamber diameter is known and the incident light flux Φ_0 can be obtained by measuring the transmitted light flux through the empty chamber. Measuring Φ_{trans} enables to calculate the extinction. By evaluating the normalized light flux which is the scattered light flux divided by the transmitted extinction is removed. As a result particle number concentration can be determined over a wide range of concentrations.

A typical normalized scattered light flux vs. time curve shows a row of consecutive maxima and minima which can be uniquely identified. The height of the scattering extremes relate linearly to the number concentration of the particles within the scattered volume. The size of the particles can be obtained from the position of the extremes. A quantitative evaluation of the experimental scattered light requires the knowledge of how the particles of a given size scatter light. For spherical particles with known refractive index this interaction is described by the so-called "Mie theory" developed by Debye[6] and Mie[25]. The light scattering of growing droplets and the subsequent illumination of the photomultiplier by the scattered light is described in detail by Wagner[53]. It turned out that the theoretical scattered light curve Φ_{theor} vs. particle size shows the same shape as the experimental scattered light curve Φ_{exp} vs. time curve. Every extreme of the theoretical curve can be assigned to the correlating extreme of the experimental curve. This provides information on the size of the particle at some given times. If enough extremes are matched a growth curve of the droplet is obtained. Particle number

concentration is obtained from evaluating the ratio of experimental scattered light flux and transmitted light flux. Therefore the photodiode (PD) and the photomultiplier (PM) have to be calibrated relative to each other which is described in detail by Peterson[29]. Practically number concentration is done by identification of the first maximum in the experimental scattered light curve. In the case of a scattering angle of $\Theta = 15$ the first maximum is relatively broad which makes it easy to determine the number concentration. The smaller the scattering angle Θ is chosen the simpler the structure of the corresponding light scattering curve gets. However it is not favorable to go to very small forward scattering angles because for decreasing angles Θ the amount of extremes decreases which is equivalent to the information on the particle growth[53].

Since the CAMS method does not refer to any empirical calibration or external standards it can be seen as an absolute method.

3.4 Setup of aerosol generation

This section deals with the production of a well defined aerosol which is necessary to receive expressive data from nucleation experiments. In this work the aerosol consists of a well known gas mass-flow carrying monodisperse sodium chloride particles in the nanometer size range and a well defined amount of n-Nonane vapor. The production process is depicted in figure 3.3. The gas serving as furnace feed flow, furnace dilution flow as well as dilution flow is dried and filtered before it enters the system. It is taken from the ambient air and has to pass an active carbon filter and a silica gel dryer. A subsequent micropore filter assures the required purity of the gas.

For the production of the monodisperse sodium chloride (Sodium chloride pro analysi, Merck) particles sodium chloride is placed in a tube furnace (ROR 1.8/18.5, Heraeus). As a consequence very small sodium chloride particles are removed from the bulk crystal by evaporation and taken out of the tube by the furnace feed flow. Right after leaving the furnace the aerosol is cooled and the furnace dilution gas flow is added. The NaCl starts to homogeneously nucleate to clusters in the nanosizerange and build up a broad size distribution which is passed on to the electrostatic classifier. The classifier enables to cut out the desired mobility of the broad primary sodium chloride mobility distribution.

Then the aerosol is either passed on to the analyzer which monitors the size distribution of the classified aerosol or it is neutralized and mixed with the vapor. Detailed information about the particle production and classification is given in section 3.5.

Vapor production is accomplished introducing a liquid beam into a glass cylinder which is heated causing the liquid to evaporate. It is schematically depicted in figure 3.3. A syringe pump (PHD 4400, Harvard Apparatus) pushes a defined

amount of C_9H_{20} (n-Nonane for synthesis, Merck) through a filter and a subsequent micro orifice which creates a liquid beam. This beam is injected into a heated glass cylinder where the liquid evaporates. At the same time the dried and filtered dilution air flow is added. In a subsequent 50L bottle the gas-vapor composite mixes homogeneously. More details about the vapor production are found in section 3.6. Finally the vapor and the particles carried by the gas flows are combined and enter the SANC system.

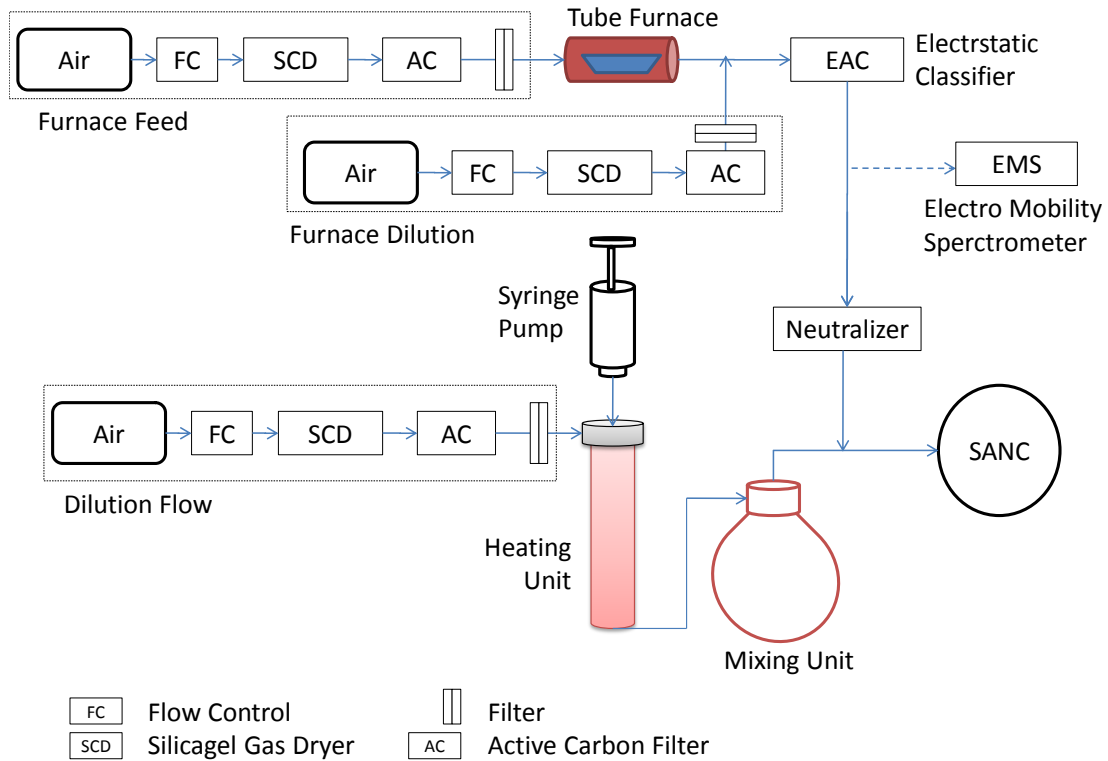


Figure 3.3: Experimental Setup

3.5 Particle production and classification

Carrying out heterogeneous nucleation experiments requires a steady supply of monodisperse and stable particles. During a measurement particle activation probability as a function of saturation ratio is investigated. As already outlined in chapter 2 particle activation is strongly related to the seed particle size. The particles produced by the tube furnace show a size distribution which is far off from

being monodisperse. Therefore the particles have to be "classified". The stability of the aerosol is also very important. If the aerosol is not stable throughout a measurement set (see section 3.2) the results are not meaningful. Further it has to be mentioned that for experiments using seed particles in the nanometer size range production rates have to be quite high because of enormous losses due to diffusion[12] and reduction during the classification process.

3.5.1 NaCl particle production

To generate the particles sodium chloride (Sodium chloride pro analysi, Merck) was deposited in an electrically heated high temperature tube furnace (ROR 1.8/18.5, Heraeus. Detailed information on the furnace is given by Scheibel and Porstendörfer[38]). This was done by introducing a glass "boat" carrying the bulk material into the furnace. The boat is not directly situated in the oven but in a quartz glass tube that is eased into the tube furnace. The furnace was kept at temperatures between 870K and 920K causing some of the sodium chloride molecules to evaporate and therefore leave the crystal. The higher the oven temperature, the higher the evaporation rate leading to bigger particles. The so-called "furnace feed" gas flow of about $1.2l/min$ carries these molecules out of the furnace. In a subsequent bubble-shaped glass vessel the molecules are cooled by adding about $1.7l/min$ dilution gas flow which is kept at room temperature. At the inlet of the dilution unit a bottleneck is located which was once (29.10.2009) clogged by salt deposition. As a consequence no more particles were produced and the gas flow decreased by the amount of the carrier gas flow. The clogging did not happen suddenly it was rather a slow process destabilizing the particle production rate and the gas flow. Three measurement days earlier the aerosol flow rate and the particle concentration already started to decrease slowly. At this time changes were within a range nearly usual but they showed a trend. Normally variations in the particle number concentration were not bigger than 4% within two hours. In the same period of time the aerosol gas flow rate usually varied by not more than 1%. The problem was solved by flushing the glass tube with clean water.

Further cooling is provided by a subsequent quartz glass tube that is cooled by water. This leads to homogeneous nucleation of the sodium chloride resulting in a relatively broad size distribution as shown in figure 3.4. The shape of this size distribution arrives some thirty minutes after switching on the tube furnace but it appeared that a stable particle concentration requires much longer timespans. For all experiments of this work the oven was switched on at least two hours before the first expansion measurements were performed.

It was tried to retain the dilution and furnace feed mass flow constant for expansion measurements of a particle size. This attempt was in fact not easy because changes of the room temperature and the ambient air pressure lead to changes of

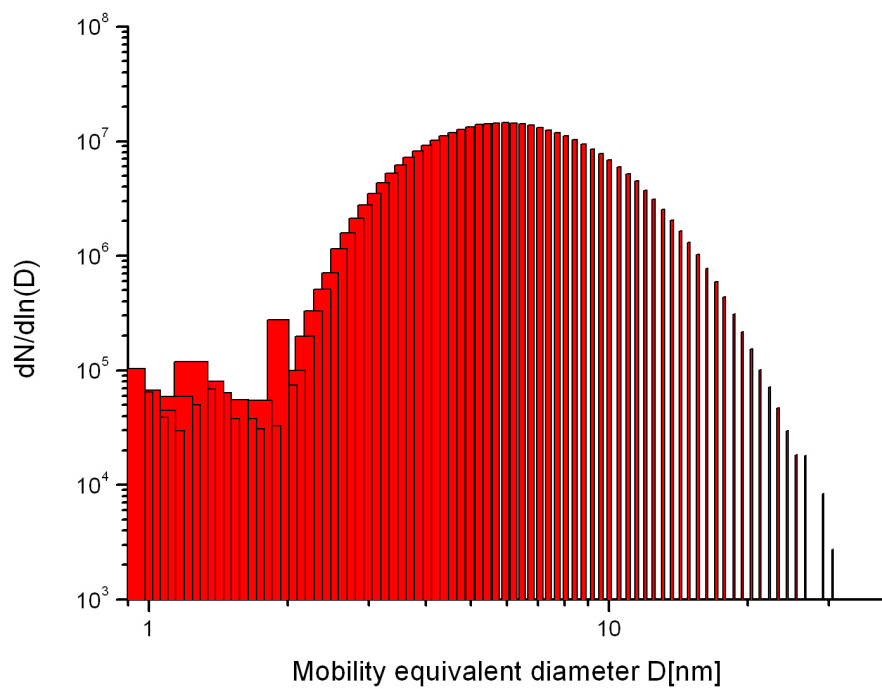


Figure 3.4: Aerosol size distribution produced by the tube furnace at $890K$. The abscissa shows the particle diameter $[D]$, the ordinate depicts the number concentration $\frac{dN}{d\ln(D)}$.

the gas flows. The room temperature was controlled by an air conditioning system and set to around 296K throughout all expansion measurements.

3.5.2 Particle classification

Since the particles produced by the oven show a relatively broad size distribution and making meaningful heterogeneous nucleation experiments requires particles as monodisperse as possible, these particles have to be classified. Classifying means extracting a certain particle size from within a particle size distribution. This is done by means of electrostatic classification (see figure 3.3: EAC) which is to be outlined in this section.

The Electrostatic Aerosol Classifier (EAC) consists of a particle charger and a subsequent Vienna-type Differential Mobility Analyzer (DMA)[34]. The structure of the charger is quite simple. Actually it is a tube featuring a Am^{241} source which provides big numbers of positive and negative ions leading to a bipolar charging of passing particles (see Fuchs [35]). The DMA mainly consists of two metal cylinders which are operated as a capacitor. The outer one is grounded whereas the inner one is set to a certain negative voltage. In between these cylinders, parallel to the center line a so-called "sheath air" gas flow of $24,7l/min$ is provided. It is run in closed loops and is continuously filtered and dried. The particles enter the DMA at the top of the outer cylinder and follow the streamlines of the sheath air. Since the particles are charged bipolarly the positively charged will be attracted by the inner cylinder while the negatively charged particles will move to the outer wall of the DMA. The bottom of the inner cylinder features the aerosol outlet where a gas flow equal in size compared to the incoming flow leaves the DMA. This gas flow carries the classified particles. They are all of nearly the same mobility Z due to the fact that the mobility is directly connected to the voltage of the inner cylinder. The resolution of the DMA is determined by the fraction of the gas flow carrying the particles (which was kept at about $2,9l/min$) and the sheath air flow of the DMA. Applying formula 3.7 the mobility equivalent particle diameter D_p can be obtained from the mobility and consequently from the voltage set at the cathode.

$$D_p = \frac{iC(D_p)}{const}V \quad (3.7)$$

D_p is the mobility equivalent diameter, i is the number of charges on the particle, $C(D_p)$ is the so-called slip correction factor[27] mainly depending on the particle size and the mean free path in the gas (the slip correction factor was first considered by Cunningham[4]), $const$ is a constant depending on the DMA's geometry and V is the voltage of the inner cylinder. Since the slip correction factor steadily decreases for increasing particle sizes and due to the assumption that every particle leaving the DMA carries only a single charge the mobility equivalent diameter

of a classified particle is solely a function of the voltage supplied on the cathode. Taking a look at Fuchs' charging theory and applying it to the primary particle size distribution produced by the tube furnace supports this assumption.

The particles classified by the EAC are neutralized before they are mixed with the vapor. This is done by a so-called "neutralizer" which works exactly the same way the charger does. The particles are passed through the neutralizer and are therefore brought into a well known charge equilibrium[35]. For particles in the size range observed in this work the probability to be uncharged exceeds 90% when leaving the neutralizer.

As heterogeneous nucleation experiments are very sensitive to cluster sizes the classified particle size distribution has to be "scanned", i.e. it has to be investigated. This is done by the Electro Mobility Spectrometer (EMS, see figure 3.3). The EMS also uses a Vienna-type DMA that is equivalent to the one performing the particle classification. Further it features a Faraday Cup Electrometer (FCE-08, tapcon und analysesysteme). In order to investigate the particles the EMS is placed downstream the EAC system. Since the particles leaving the electrostatic aerosol classifier are approximately all of the same mobility they will only reach the outlet of the analyzer if the cathode is set to the same voltage used for classifying. Leaving the aerosol outlet the particles hit the electrometer and trigger a signal because of the charge they carry. From counting the single charges detected by the Faraday cup the particle number concentration of a certain mobility is determined. Scanning the incoming aerosol is done by stepwise decreasing the voltage set at the cathode and simultaneously recording the measurement signal of the electrometer. To make dealing with the obtained data easier it is fitted using a gauss function. The main results of the investigation are among others the mean geometric diameter of the particles, the number concentration and the standard deviation of the gauss fitting function. A typical secondary particle size deviation is depicted in figure 3.5.

The EMS system was applied before and after every measurement to check the aerosol. Scanning the aerosol during the measurement is not possible because the particles are stuck in the Faraday cup. A possibility would be to scan a fraction of the classified aerosol and pass the other part on to the SANC. This would require high particle numbers. Since the shape of the size distribution and the number concentration of the classified particles turned out to be quite stable it is not necessary.

It turned out that the mean geometric particle diameter monitored by the EMS was decreasing in time. This sort of particle shrinkage was observed throughout all of the measurements. However, the shrinkage observed was quite small but significant as depicted in figure 3.6. The abscissa depicts the time in minutes and the ordinate shows the "normalized" particle diameter (i.e. the particle diameter

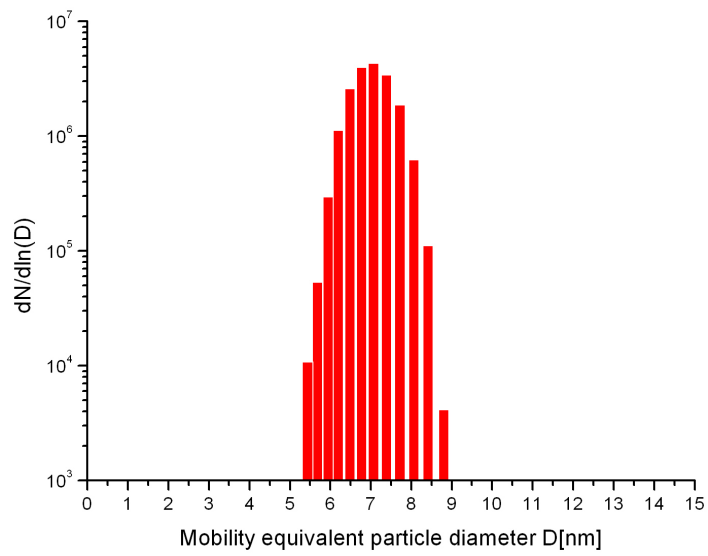


Figure 3.5: Aerosol size distribution produced by the tube furnace at $615^\circ C$. The abscissa shows the particle diameter $[D]$, the ordinate depicts the number concentration $\frac{dN}{d\ln D}$. The mean geometric diameter is $6,99nm$ and the standard deviation (referring to a Gauss-fit) $\sigma = 1,0355$.

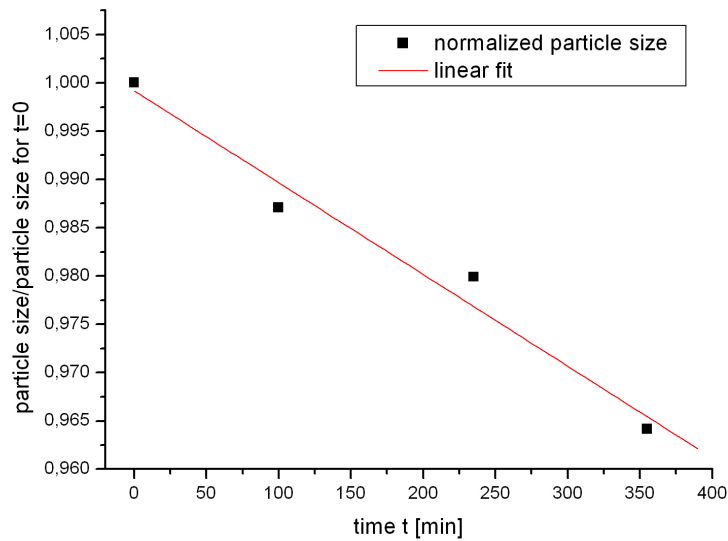


Figure 3.6: Decreasing particle mean geometric diameter monitored throughout a measurement day (17.09.2009).

D_t at a certain time t divided by particle diameter at $t = 0 \text{ min}$ D_0). A linear fit was applied to illustrate the trend. The equation determining the linear fit is given by: $D_t = D_0 + kt$, where $k = 9,505 (10)^{-6} [\text{min}^{-1}]$ is the slope of the fit. This means that the mobility particle diameter of particles leaving the classifier shrink by approximately 0,6% within an hour. Further the mean geometric diameter of the particles classified was not exactly the size desired. This is caused by the asymmetric shape of the primary aerosol.

3.6 Vapor Production

The vapor is needed to activate the sodium chloride particles. As already outlined in chapter 2 particle activation strongly depends on the saturation ratio S of the present vapor. Therefore the saturation ratio after the expansion has to be known as exactly as possible. As depicted in section 3.3 this requires knowledge of the vapor pressure p_v and the saturation vapor pressure $p_s(T)$. Formula 3.4 enables to calculate the saturation vapor pressure for a given temperature by using some coefficients that can be obtained from literature. The determination of partial vapor pressure of the n-Nonane vapor is carried out in this manner:

Under the assumption that the gas-vapor mixture can be treated as an ideal gas

equation 3.8 can be applied:

$$pV = Nk_bT \quad (3.8)$$

where p is the total pressure, V is the total volume, N is the amount of molecules, k_b is the Boltzmann constant and T is the temperature. Using Dalton's law[5] the total pressure can be written as a sum of the partial vapor pressures. This makes it possible to use the ideal gas equation for one constituent of gas:

$$p_iV = N_ik_bT \quad (3.9)$$

where p_i is the partial vapor pressure and N_i is the amount of particles. Dividing equation 3.9 by equation 3.8 leads to:

$$\frac{p_i}{p} = \frac{N_i}{N} \quad (3.10)$$

If the fraction of the particle numbers N is replaced by the fraction of the volume gas flows $Q = \sum Q_i$ one ends up with the partial vapor pressure of a constituent depending on the total pressure and the fraction of the volume flow rates:

$$p_i = p \frac{Q_i}{Q} \quad (3.11)$$

The total pressure is measured using a mercury barometer (GOLDTIME, i.b.o.). The partial gas flow of the carefully dried and cleaned carrier gas is measured using a gas meter (G4, S.Elster GmbH). The gas meter is capable of measuring gas volume flows from $0.7l/min$ up to $100l/min$ within a pressure interval from $500mbar$ up to $1500mbar$. But the total gas flow $Q = \sum Q_{dilution} + Q_{vapor}$ and the partial vapor gas flow Q_{vapor} have to be calculated (see equation 3.12) since the working liquid is introduced to the system in liquid form.

$$Q_{vapor} = \frac{V_{vapor}}{t} = \frac{V}{t} \frac{Q_{vapor}}{Q} = \frac{N_{vapor}}{t} \frac{k_bT}{p} \quad (3.12)$$

Using $N_{vapor} = \frac{V_{liquid}\rho_{liquid}N_A}{M}$ where V_{liquid} and ρ_{liquid} are volume and density of the substance in the liquid matter of state, M is the molar mass and N_A the Avogadro constant. The equation 3.12 can be written as:

$$Q_{vapor} = \frac{V_{liquid}T}{tp} \frac{\rho_{liquid}k_B N_A}{M} \quad (3.13)$$

Now the partial vapor pressure Q_{vapor} depends on a volume of liquid per time that is introduced into a system with a certain pressure and temperature. The liquid density ρ_{liquid} is obtained from literature[49].

To infuse the liquid into the system a syringe pump (PHD 4400, Harvard Apparatus) was used. Liquid infusion rates of 1nl/hr up to 220ml/min with an accuracy of 0,35% are provided by this device. Actually the upper infusion limit was determined by the volume of the syringe. To carry out a measurement set it is necessary to produce a constant beam over a period of at least one and a half hours. Hence the maximum infusion rate is about $1,55\text{ml/min}$. In this work infusion rates between $45\mu\text{l/min}$ and $0,305\text{ml/min}$ were applied. The liquid is pushed through a filter and reaches a micro orifice that produces a liquid beam. Three different micro orifices have been used throughout this work. The inner diameter of the biggest was $35\mu\text{m}$ and it was used for infusion rates higher than $0,15\text{ml/min}$. At lower infusion rates ($0,095\text{ml/min}$ to $0,15\text{ml/min}$) the medium size micro orifice was devoted. The smallest orifice with an inner diameter of only $10\mu\text{m}$ was used to produce infusion rates smaller than $55\mu\text{l/min}$. It turned out that measurements with the smallest micro orifice are extremely time consuming because producing a constant liquid beam is a tough task. The tiny aperture is clogged very easy by some liquid residuals. A clogged micro orifice is put into some isopropanol and positioned in an ultra sonic bath for at least ten minutes. This should restore normal operation of the orifice.

The liquid beam produced by the orifice is then injected into a glass cylinder (see figure 3.3: heating unit). The glass cylinder was kept at 420K to evaporate the liquid. Through a tube which was heated to 360K the gas-vapor mixture is passed on to a 50 liter mixing bottle. Depending on the dilution gas flow that was varied between $4,2\text{l/min}$ and 8l/min the gas is suspended in the bottle for at least 6 minutes ensuring a homogeneous mixing of gas and vapor. A subsequent tube leading to a crossing point where the vapor and the particles are mixed together was occasionally heated depending on the relative humidity of the vapor at ambient room temperature. By the carrier gas the vapor and the particles are passed on to the SANC system.

4 Investigation of NaCl particle shrinkage in n-Nonane vapor

Previous experiments[18, 29, 42]have shown that the mep(mobility equivalent particle) diameter of "dry" NaCl particles decreases when they get in contact with various types of vapor. In all of these experiments the particles were produced by means of nucleation. Krämer et al.[18] observed significant NaCl mep diameter shrinkage for particles interacting with water vapor. Peterson[29] and Schobesberger[42] used the same setup as applied throughout this work to produce nanosized NaCl particles (see section 3.5). They observed the particle shrinkage in a n-propanol humidified environment. The higher the saturation ratio of the n-Propanol the stronger the particle shrinkage was. Growth factors of mep diameters down to 0,84 were obtained (equivalent to a shrinkage of 15,6%) for vapor saturation ratio $S = 1$.

For this work particle shrinkage has also been considered. The setup of the investigation is schematically depicted in figure 4.1. The aerosol gas flow Q_{ae} carrying

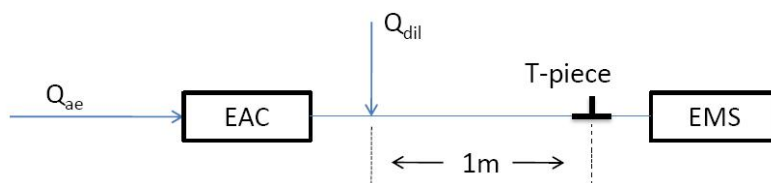


Figure 4.1: Setup of particle humidifying to observe possible reduction of the mobility equivalent diameter

the NaCl particles(see section 3.5.1) which are classified (according to section 3.5.2) within the Electrostatic Aerosol Classifier(EMS). Downstream the EMS the aerosol is diluted by the dilution air flow Q_{dil} . The dilution gas flow is either "dry" which means that it does not carry any n-nonane vapor for measurements of saturation ratios $S_{n-nonane}$ equal to zero. Or well defined saturation ratios are provided by this gas stream as outlined in section 3.6. For expansion measurements the saturation ratio S is calculated by the software program Acquire[23]. Since the saturation ratio at ambient pressure and air temperature is needed there is no expansion event for this experiment. Acquire is designed in a way that it only performs calculations of saturation ratios if an expansion event happens. Thus the pressure difference between ambient air and underpressure vessel (see section 3.2) was set to the smallest value possible which is $1mbar$. The result was the calculation of "S" for a system with a pressure about $1mbar$ below the one observed.

Also the temperature was lower. To avoid this a second calculation was carried out. Now the difference in pressure and temperature due to the pressure drop were added to the ambient. An expansion similar to the previous was carried out. Now the saturation ratio obtained from the program's calculation was a good approach for the "real" S within the setup.

The mixture of Q_{ae} and Q_{dil} is passed on to the "analyzer"(Electro Mobility Spectrometer) where the mep size distribution of the particles is monitored. Since the analyzer has to be operated at approximately the same gas flows as the classifier a preceding T-piece open to the ambient air is installed.

4.1 Measurement technique and results

To obtain the shrinkage of a particle its primordial size has to be known. As already mentioned in section 3.5.1 the mean geometric diameter of the particles classified is not exactly the size the classifier is set to. Thus the particles have to be investigated in a "dry" environment before considering their shrinkage. Three different particle sizes have been used: 7nm, 10nm and 15nm. First, the classifier(EAC) was set to 7nm particle diameter, then to 10nm and finally to 15nm. The actual mep diameter of the NaCl particles was measured at the same time using the analyzer(EMS). For every particle "size" about ten scans of the classified aerosol were performed. Then the vapor production is started(see section 3.6). This takes about 40min. The "wet" particles(i.e. the particles in contact with the vapor) are investigated in the same manner as the dry ones.

All the results obtained are listed in table 4.1.

As can be seen the particles showed a "shrinkage" of about 4% even though there was no vapor in the system. However, this behavior of the particles is depicted in section 3.5.1 and does not relate to the n-nonane vapor. The difference between the size set at the classifier and that measured by the analyzer also occurred when the particles did not pass passages that were in contact with n-nonane vapor. At earlier times(2008) the classifier came in contact with a n-propanol vapor which causes shrinkage to NaCl particles. But it has been well flushed since then. Further there seems to be a slight shrinkage with increasing n-nonane saturation ratios.

4.2 Interpretation

From the experimental data shown in table 4.1 no obvious trend is visible. The results for every particle size are plotted in figures (4.2,4.3,4.4). For visualization the data points have been fitted linearly. The fitting details are given by table 4.2:

Particle "size"	n-Nonane saturation ratio S	Growth factor
7nm	0%	0,951±0,008
		0,965±0,005
		0,967±0,009
		0,960±0,003
		0,966±0,008
10nm	68%	0,957±0,004
		0,966±0,005
		0,954±0,002
		0,960±0,006
		0,965±0,004
15nm	79%	0,961±0,008
		0,949±0,012
		0,960±0,004
		0,956±0,001
		0,955±0,005
15nm	84%	0,961±0,003
		0,957±0,005
		0,943±0,006
		0,956±0,002
		0,956±0,002

Table 4.1: Raw data of NaCl particle shrinkage investigation.

The fitted data show a slight increase in particle size(which is not significant) for

linear fit: $y = a + bx$		
size class	a	b
7nm	$0,961 \pm 0,003$	$0,003 \pm 0,007$
10nm	$0,960 \pm 0,003$	$-0,004 \pm 0,006$
15nm	$0,958 \pm 0,003$	$-0,008 \pm 0,006$

Table 4.2: Linear fit of particle shrinkage

the "7nm" particles, whereas the "10nm" and "15nm" show a slight decrease in particle size.

To provide more validity on the data points they have to be considered one by one. This is done based on figure 4.4. Hence the experiments were carried out simultaneously(in good approximation) this considerations can also be applied to the other particle sizes: Starting with the points at n-nonane saturation ratios $S_{n-nonane} = 0$ it has to be pointed out again that the particle sizes set at the classifier do not have exactly the size the analyzer shows. This explains the decrease in size of about 4% compared to 15nm set at the classifier. Furthermore these data points have not been measured at the same day. This shows how reproducible the aerosol generation is. The data points at saturation ratios $S_{n-nonane} \neq 0$ have been measured about 40min after the points for $S_{n-nonane} = 0$. Thus the time dependent particle shrinkage(see section 3.5.2) has to be taken into account. The shrinkage of the data points would be about 0,4% less if it was measured at the same time the $S_{n-nonane} = 0$ data points were recorded. The reduction of the shrinkage for the experiment with $S \approx 0,8$ is even higher since it was measured at the end of the experiment day(16⁴⁰) on 10.09.2009).

To summarize these considerations it has to be said that no significant shrinkage of NaCl particles interacting with n-nonane vapor has been observed. Further it rather looks like there was a slight increase in particle size in the case of the "7nm" particles.

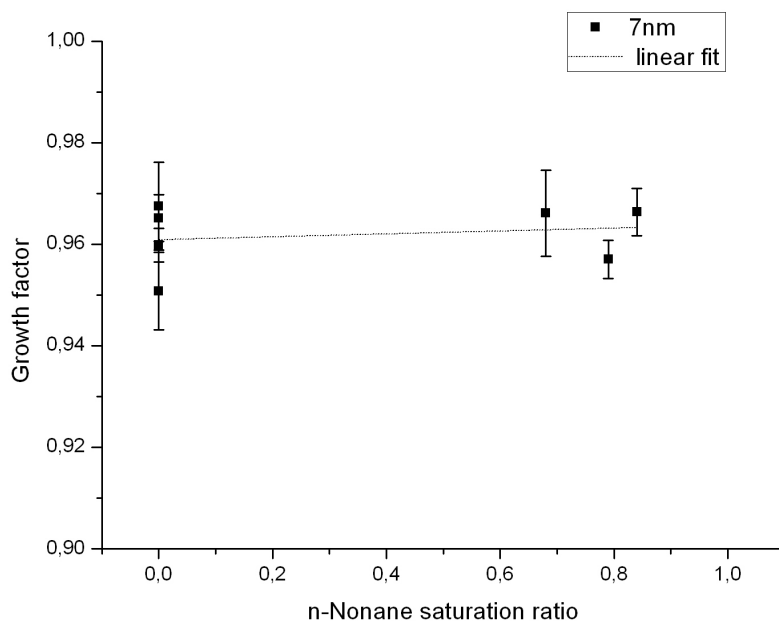


Figure 4.2: Result of measurements on sodium chloride particle shrinkage in n-nonane vapor. The electro mobility equivalent diameter of the particles was set to 7nm using the EAC(see chapter 3).

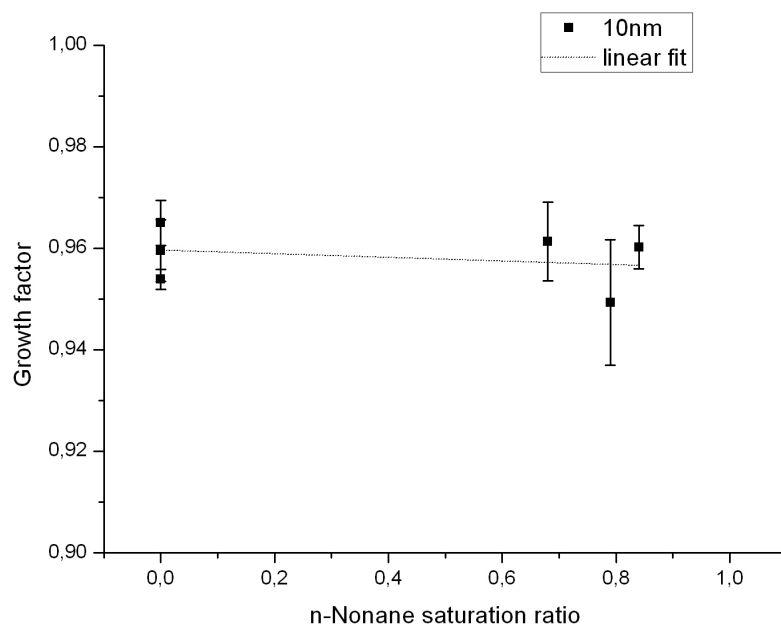


Figure 4.3: Result of measurements on sodium chloride particle shrinkage in n-nonane vapor. The electro mobility equivalent diameter of the particles was set to 10nm using the EAC(see chapter 3).

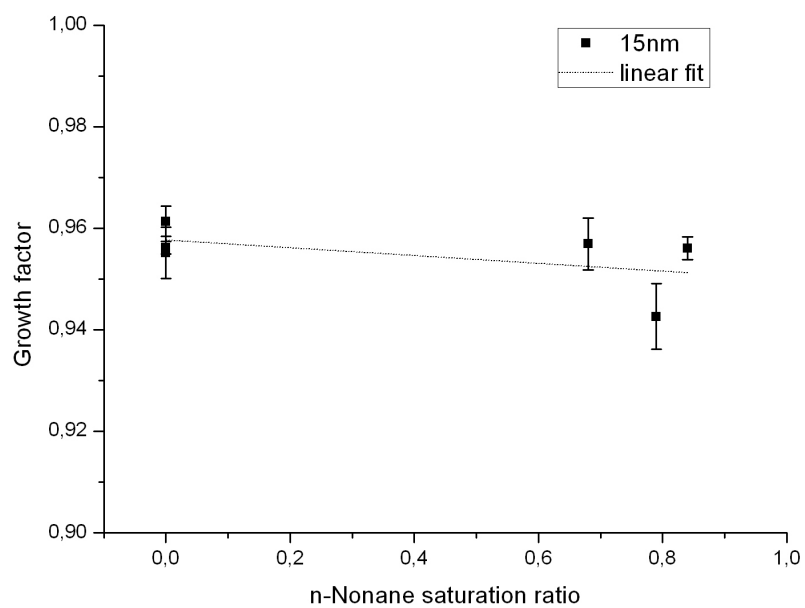


Figure 4.4: Result of measurements on sodium chloride particle shrinkage in n-nonane vapor. The electro mobility equivalent diameter of the particles was set to 15nm using the EAC(see chapter 3).

5 Investigation of the temperature dependence of heterogeneous nucleation of nonpolar n-Nonane on polar NaCl seed particles

To investigate the heterogeneous nucleation of n-Nonane vapor on NaCl seed particles an adiabatic expansion was applied to a cylindrical chamber(see section 3.1) causing n-Nonane vapor to nucleate upon the NaCl seed particles. The number concentration of the activated particles N_{act} at a known saturation ratio $S(T)$ was observed deploying the CAMS method(outlined in section 3.3). The heterogeneous activation probability P_{act} is determined by dividing the number concentration of the activated particles N_{act} by the total number concentration N_{tot} :

$$P_{act} = \frac{N_{act}}{N_{tot}} \quad (5.1)$$

Plotting the P_{act} against the saturation ratio at which it was obtained leads to the so-called "heterogeneous activation probability curve". For small saturation ratios the heterogeneous activation probability is zero which means no particle activation or more precisely particle growth was noticed. Actually the evaluation of the scattered light signal never leads to an activation $N_{act} = 0$ because of the noise of the detector. Since the signal of the detector is only evaluated if a significant particle growth is monitored N_{act} is assumed to be zero for lower saturation ratios. The higher the saturation ratio $S(T)$ the higher the particle number concentration gets until all particles are activated. As can be seen from equation 5.1 measurements at total activation are essential to calculate P_{act} . Further evaluations of the data is based on the heterogeneous activation probability curve.

In this work three different particle "size classes" are used to perform nucleation experiments: 7nm, 10nm and 15nm particles. Size class means that the particles did not have exact the size which is suggested by the name. There are two reasons for this: On the one hand the particle production does not lead to a physical diameter but to the so-called "mobility equivalent diameter"(outlined in section 3.5.1). On the other hand even the mobility equivalent diameter differs from the size implied by the size class name(reasons for this are also depicted in section 3.5.1). Precisely the diameter referred to in this chapter is named mean geometric mobility equivalent diameter.

Since this is quite inconvenient the mean geometric mobility equivalent diameter is simply called "diameter" throughout this chapter.

5.1 Accomplishment of the experiment

The technical details of the experiment are outlined in chapter 3 but the accomplishment of a measurement was barely treated in this work. Since a very important aspect of the measurements is that they are carried out under well defined conditions a typical structure throughout a measurement day immediately suggests itself:

At first the oven needed for particle production and the compressor which provides pressurized air are switched on. Then all the SANC components are turned on as well as the classifier and analyzer system(see 3.5). It takes about one and a half hours until the gas flows get stable. Then the dilution air flow(section 3.4) is measured twice. Each time for about ten minutes using the gas meter as described in section 3.6. At the same time the primary and afterwards the classified aerosol are monitored. If the gas dilution flow as well as the classified aerosol are stable the gasflow carrying the NaCl particles Q_{ae} is measured once. To reach the desired saturation ratio S and temperature T after the adiabatic expansion the liquid infusion rate can be calculated(see section 3.6) using the software program Acquire[23]. In other words the appropriate experimental settings have to be found. This requires knowledge of the chamber temperature, the ambient air pressure, the pressure drop during the expansion, the gas mass flow(i.e. volume and temperature), the liquid density, its surface tension and vapor pressure. All these data is entered into the software program and an expansion is performed simulating the experiment. The pressure drop is monitored and therefore the temperature after the expansion and the "theoretical"(since there is no vapor in the system yet) saturation ratio $S(T)$ after the expansion can be calculated. In this work experiments were carried out at three different temperatures after the expansion: $+10^{\circ}C$, $0^{\circ}C$ and $-10^{\circ}C$. This temperature can be influenced by the pressure drop and the temperature of the chamber(see section 3.1) and is found rather easily due to the fact that the pressure drop and the chamber temperature are nearly continuously variable over a wide range. To find proper settings for the gas and liquid flows is more challenging as there are some technical restrictions. The gas flow entering the SANC system has to be at least $7,5l/min$ at ambient air pressure(see section 3.2). Further variation of the liquid infusion rates are limited by the micro orifices used(depicted in section 3.6). While proper settings for the liquid infusion rate are calculated by trial and error the Q_{ae} gas flow is measured for a second time. Then the SANC cycle(section 3.2) is stopped and the infusion pump is switched on. It is essential to switch off the cycle before the infusion is started since the chamber should not get in contact with the vapor before the experiment is started. This might lead to an activation of the particles at saturation ratios lower than "normally" needed. After approximately one hour the vapor is ready(i.e. it is homogeneously mixed and of the desired relative humidity) and the experiment is started.

Five runs are measured each containing of five equal adiabatic expansions. The pressure drops of the first and second run are chosen in a way that not all of the particles are activated which means that they are on the slope of the heterogeneous activation probability curve. This of course already requires rough knowledge of the $P_{act}(S)$ dependence. The other runs are measured at comparatively high pressure drops to ensure all particles to be activated. The average of these concentrations is used to calculate the heterogeneous activation probability P_{act} applying equation 5.1.

5.1.1 Data acquisition

Ambient pressure, scattered and transmitted light are the quantities to be measured during the adiabatic expansion to receive data that serve as a basis for determination of heterogeneous activation probability curves $P_{act}(S)$ (for more details see section 3.3). As outlined in section 3.1 calculations on the saturation ratio requires amongst others knowledge of the pressure in the system. A pressure sensor provides time resolved information of the pressure in the expansion chamber. The scattered light and the transmitted light are measured by a photomultiplier(PM) and a photodiode(PD) respectively. The pressure sensor, the photo detector(PD) as well as the photomultiplier(PM) are connected to a Intel 80486 PC system. Time resolution as well as measurement time is set by the software program Acquire which also monitors pressure $p(t)$, scattered light $\Phi_{sca}(t)$ and transmitted light $\Phi_{trans}(t)$. Storage of the data to hard disk is optional and also performed by Acquire.

5.1.2 Data evaluation

The foundation of data evaluation is the analysis of the scattered and transmitted light curves leading to particle number concentration and particle growth. The principles for that are depicted in section 3.3.

Practically the evaluation of the signals measured by the photo detector and the photomultiplier are done using the software program Reduce[51] which was developed specifically for this application. As mentioned in section 5.1 every run consists of expansions the so-called shots. Using Reduce a run is evaluated by first selecting the shots that appear to be reasonable. If one of the shots differs from the others(e.g.: if the chamber is not properly flushed some liquid sticks to the walls and causes a higher saturation ratio $S(T)$ compared to subsequent shots leading to a faster droplet growth) then these shots need to be excluded from the evaluation. There are no objective rules which shot to include and which one to "skip". It requires experimental experience.

From the shots chosen the program calculates an average light signal. This average

light curve is then compared to a theoretical light curve to receive the particle number concentration and droplet growth (more details are given in section 3.3). Particle number concentration serves to generate the heterogeneous activation probability curve dependent on the saturation ratio. Whereas droplet growth provides a quality control of the measurement. Since the theory of droplet growth [31] is well-established it can be compared with the points (droplet size at given time) obtained from matching theoretical and experimental scattered light curve maxima and minima. If the theoretical droplet growth does not fit well to the points measured experimentally the data is excluded from further evaluation.

A further goal of data evaluation is to determine the onset saturation ratio S_{onset} which is the saturation ratio $S(T)$ causing 50% of all the particles to grow to detectable size.

5.2 Results

The data obtained from evaluating the scattered light curves by using the software program Reduce is showcased in this section. It was produced in a uniform manner (see section 5.1). Heterogeneous activation probability curves at constant temperature are presented in figures 5.1 to 5.10. The plots consist data points of different colors. Every color represents one data set including five adiabatic expansions. All data points showing an heterogeneous activation probability $0 < P_{act} < 0,95$ (data points on the slope) are within a temperature interval of $0,3^{\circ}C$. The dashed lines as well as the solid line in the plots are added to guide the eye.

Further, details on the aerosol and the related n-Nonane onset saturation ratios are plotted in the tables (5.2.1, 5.2.2, 5.2.3).

5.2.1 7nm seed particles

The 7nm NaCl particles used for this measurement were produced at tube furnace temperatures of approximately $620^{\circ}C$. Activating these small particles requires a relatively high n-nonane saturation ratio $S(T)$. For experiments investigating nucleation processes at $0^{\circ}C$ and $-10^{\circ}C$ moderate infusion rates were sufficient to reach the desired saturation ratio. Whereas experiments at $10^{\circ}C$ after the expansion had to be carried out at high infusion rates leading to "critical" relative humidity in the system. Critical in this context means that either values of relative humidity are high enough to cause vapor losses to tube walls before the aerosol enters the expansion chamber or the chamber is not properly cleaned after the expansion. If some of the vapor is lost to the walls because of condensation the experimentally obtained data points will differ from the theoretical droplet growth curve. Thereby the data is meaningless and the system has to be flushed thoroughly before the next measurement is to be prepared. Insufficient flushing of the

chamber engenders easier activation (i.e. at lower saturation ratios than usually necessary) of the seed particles. This effect can be observed in figure 5.3. Obviously total activation occurred at too low saturation ratios for some of the sets. Since the steepness of the slope seems to be okay and the saturation ratio at which $P_{act} = 1$ is not necessarily relevant to data evaluation it is possible to include this data.

D_p [nm]	T [$^{\circ}C$]	σ	S_{onset}
$6,94 \pm 0,02$	$-10,1 \pm 0,02$	$1,036 \pm 0,001$	$2,01 \pm 0,14$
$6,93 \pm 0,01$	$-0,1 \pm 0,02$	$1,036 \pm 0,001$	$2,02 \pm 0,14$
$6,94 \pm 0,01$	$+9,9 \pm 0,02$	$1,036 \pm 0,001$	$2,02 \pm 0,14$

Table 5.1: Experimental results for n-nonane nucleation on $7nm$ sodium chloride seed particles. Column 1 to 3 characterize the experimental conditions: particle diameter D_p , nucleation temperature T and the geometric standard deviation σ of the "monodisperse" aerosol size distribution. The last column features the onset saturation ratio S_{onset} . The errors of D_p , T and σ were statistically determined whereas the error of S was calculated from the geometric standard deviation σ of D_p using the Kelvin equation.

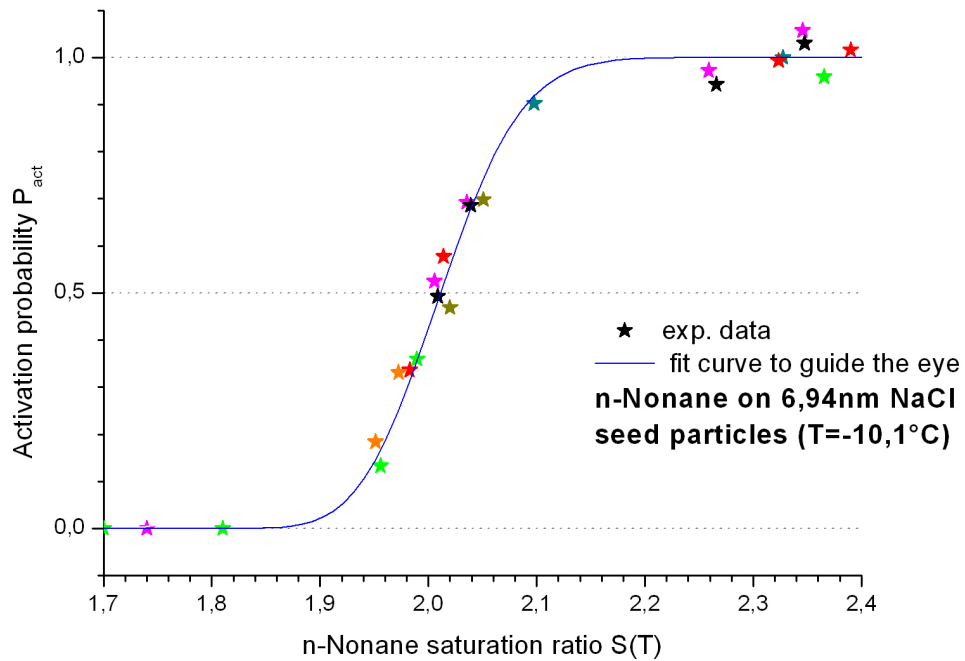


Figure 5.1: The heterogeneous activation probability curve of 7nm sodium chloride particles at $-10,1^{\circ}\text{C}$ determined by the experimental data points which are represented by the star-shaped symbols. Every measurement set is illustrated by a different color. At activation probabilities $P_{act} = [0; 50; 100]\%$ dashed lines are included for better orientation. The solid line represents a hyperbolic tangent function which was manually fitted to the experimental data points to guide the eye.

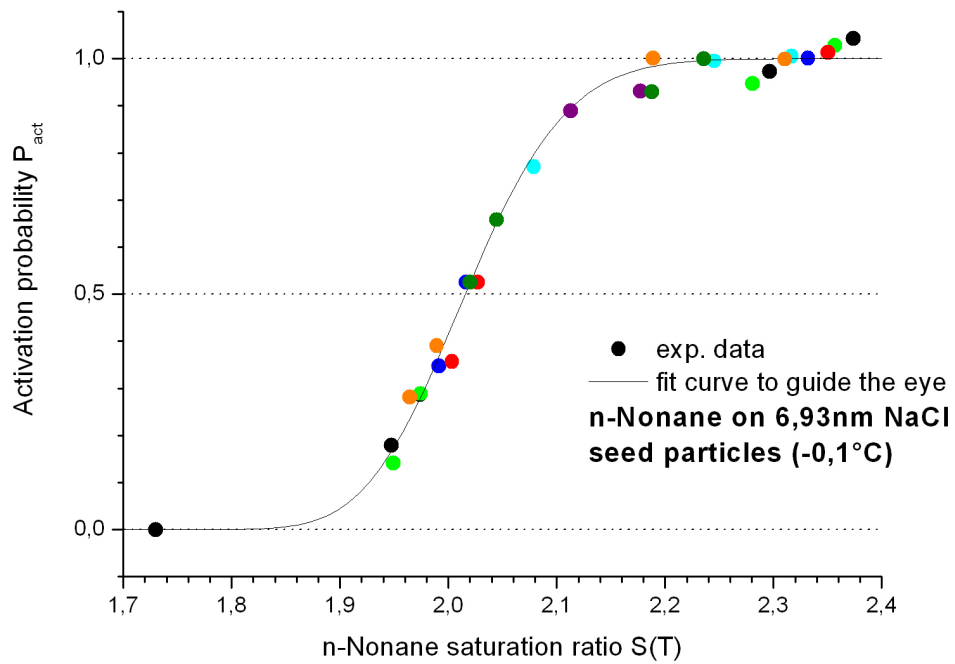


Figure 5.2: The heterogeneous activation probability curve of 7nm sodium chloride particles at $-0,1^{\circ}C$ determined by the experimental data points which are represented by the circular symbols. Every measurement set is illustrated by a different color. At activation probabilities $P_{act} = [0; 50; 100] \%$ dashed lines are included for better orientation. The solid line represents a hyperbolic tangent function which was manually fitted to the experimental data points to guide the eye.

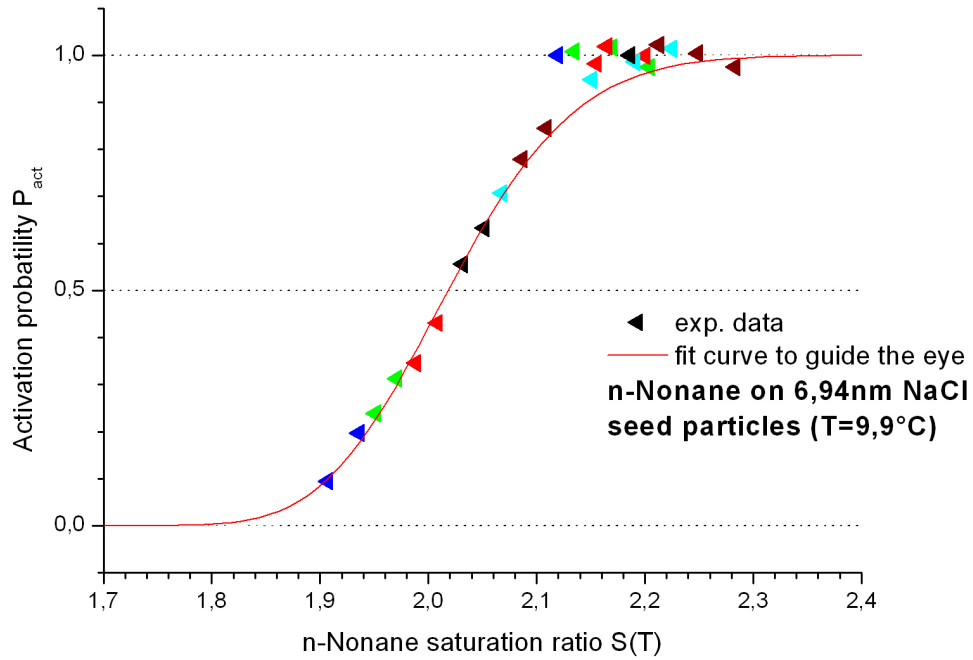


Figure 5.3: The heterogeneous activation probability curve of 7nm sodium chloride particles at $+9,9^{\circ}\text{C}$ determined by the experimental data points which are represented by the triangular symbols. Every measurement set is illustrated by a different color. At activation probabilities $P_{act} = [0; 50; 100]\%$ dashed lines are included for better orientation. The solid line represents a hyperbolic tangent function which was manually fitted to the experimental data points to guide the eye. The early total activation of the particles for some of the sets is discussed in this section.

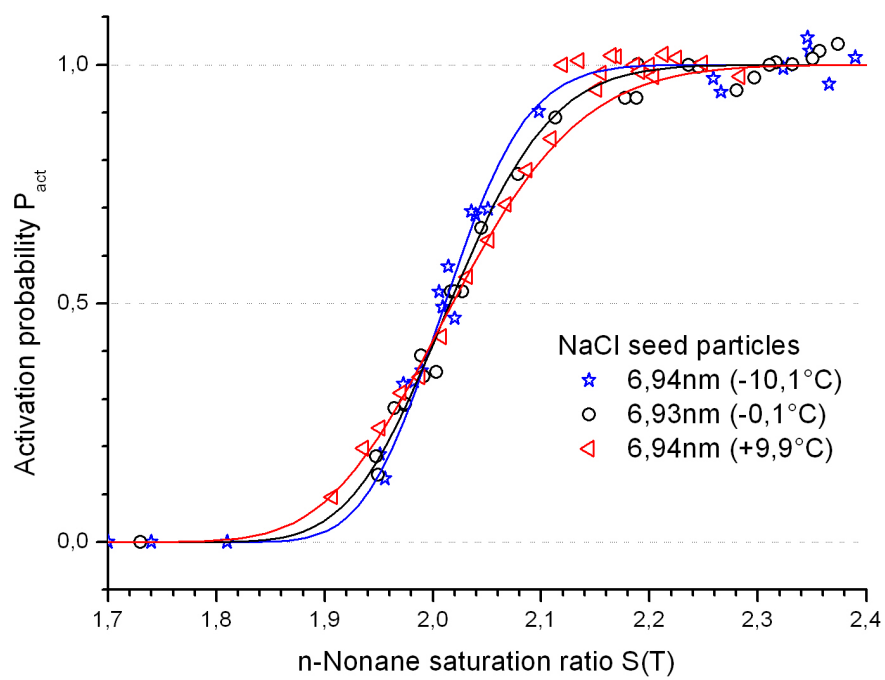


Figure 5.4: Superposition of figures 5.1, 5.2 and 5.3.

5.2.2 10nm seed particles

To produce sodium particles of 10nm in diameter the furnace temperature was set to 630°C throughout the measurement. Measurements at nucleation temperatures of +10°C and -10°C were performed. Starting-up difficulties impeded the experiments. It turned out that infusion rates necessary to obtain the required saturation ratio $S(T)$ were outside the range provided by the micro orifices used in this work(see section 3.6). The highest infusion rate of the smallest micro orifice is limited to about 55 μ l/min whereas the lower infusion rate limit of the micro orifice a size larger is at least 0,095ml/min. To realize the required liquid injection of about 0,9ml/min a vacuum pump was added to the setup removing some of the vapor-carrier gas mixture. The pump was placed just upstream the t-piece where the vapor is mixed with the particles (see figure 3.3). Consequently parts of the vapor were removed being tantamount to a lower infusion rate. Assuming that the gas-vapor mixture can be treated as an ideal gas this "effective" infusion rate is calculated from the infusion rate set using equations 5.2 and 5.4:

$$Q_{inf} = \frac{V}{t} \quad (5.2)$$

where Q_{inf} is the infusion rate of the n-nonane, V is the n-nonane volume which is injected per time t . Since the volume removed by the vacuum pump refers to a gas, the volume of the injected n-nonane in the gas phase is of interest:

$$V = \frac{m}{M} \frac{RT}{p} \quad (5.3)$$

where V is the volume, m is the total mass, M is the molar mass, R is the molar gas constant, T is the temperature in K and p is the pressure. Calculating the n-nonane gas flow rate and measuring the carrier gas flow rate(see section 3.6) provides the flow rate of the mixture Q_{mix} . The vacuum pump removes a fraction Q_{vac} of the flow rate Q_{mix} leading to a flow rate Q'_{mix} :

$$Q'_{mix} = \left(1 - \frac{Q_{vac}}{Q_{mix}}\right) Q_{mix} \quad (5.4)$$

Since the carrier gas and the vapor gas are assumed to be homogeneously mixed, a reduction of Q_{mix} by a factor of $\left(1 - \frac{Q_{vac}}{Q_{mix}}\right)$ is tantamount to a reduction of the carrier gas, the n-nonane in the gas phase as well as the liquid n-nonane infusion rate by the same factor. As a result the effective n-nonane infusion rate $Q_{inf,eff}$ is determined by:

$$Q_{inf,eff} = \left(1 - \frac{Q_{vac}}{Q_{mix}}\right) Q_{inf} \quad (5.5)$$

where Q_{inf} is the n-nonane infusion rate set at the syringe pump(see section 3.6).

D_p [nm]	T [$^{\circ}C$]	σ	S_{onset}
$9,84 \pm 0,02$	$-10,1 \pm 0,02$	$1,037 \pm 0,005$	$1,65 \pm 0,1$
$9,81 \pm 0,02$	$+9,8 \pm 0,02$	$1,0375 \pm 0,005$	$1,64 \pm 0,1$

Table 5.2: Experimental results for n-nonane nucleation on 10nm sodium chloride seed particles. Column 1 to 3 characterize the experimental conditions: particle diameter D_p , nucleation temperature T and the geometric standard deviation σ of the "monodisperse" aerosol size distribution. The last column features the onset saturation ratio S_{onset} . The errors of D_p , T and σ were statistically determined whereas the error of S was calculated from the geometric standard deviation σ of D_p using the Kelvin equation.

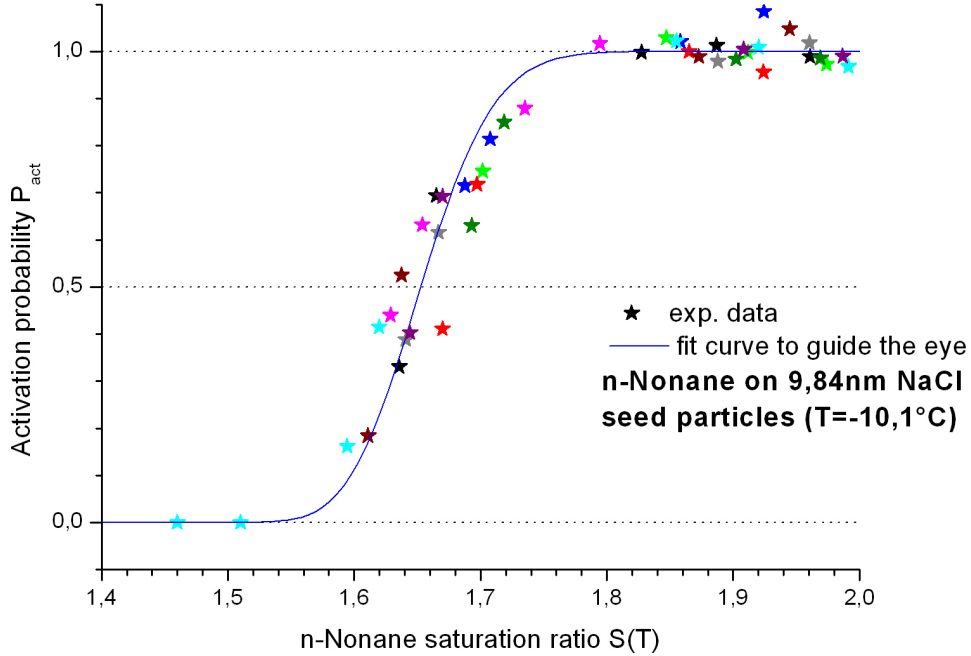


Figure 5.5: The heterogeneous activation probability curve of 10nm sodium chloride particles at $-10,1^{\circ}C$ determined by the experimental data points which are represented by the star-shaped symbols. Every measurement set is illustrated by a different color. At activation probabilities $P_{act} = [0; 50; 100]\%$ dashed lines are included for better orientation. The solid line represents a hyperbolic tangent function which was manually fitted to the experimental data points to guide the eye.

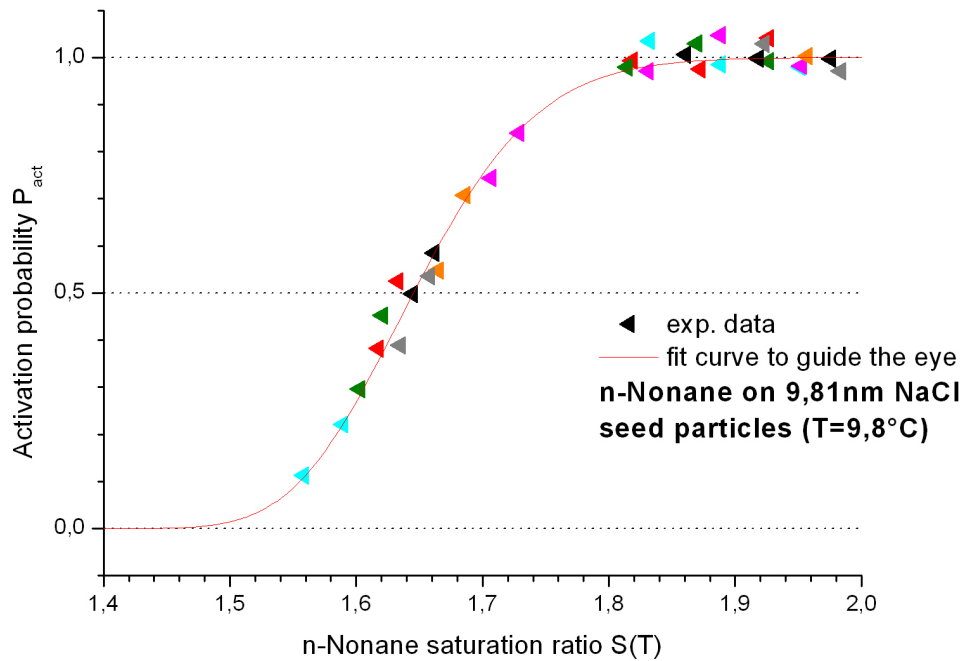


Figure 5.6: The heterogeneous activation probability curve of 10nm sodium chloride particles at $+9,8^{\circ}C$ determined by the experimental data points which are represented by the triangular symbols. Every measurement set is illustrated by a different color. At activation probabilities $P_{act} = [0; 50; 100] \%$ dashed lines are included for better orientation. The solid line represents a hyperbolic tangent function which was manually fitted to the experimental data points to guide the eye.

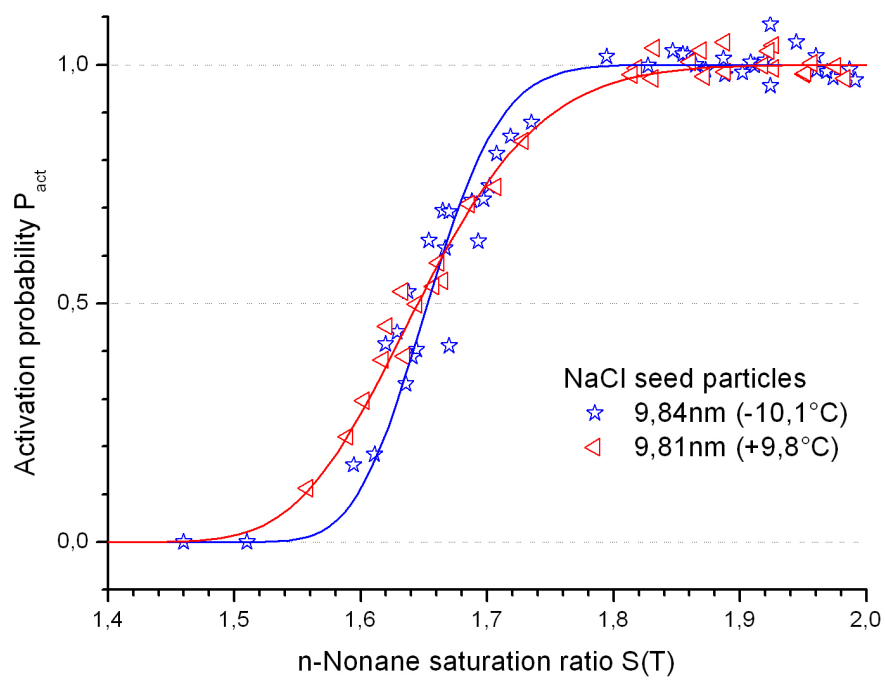


Figure 5.7: Superposition of figures 5.5 and 5.6.

5.2.3 15nm seed particles

The particles featuring a diameter of 15nm were produced at furnace temperatures of about 650°C . To achieve the n-nonane saturation ratios required to activate the particles at -10°C , 0°C and $+10^{\circ}\text{C}$ all three micro orifices have been used.

Table 5.2.3 which is added to give details of the measurement conditions shows that experiments at 0°C and -10°C used particles with nearly the same diameter whereas at $+10^{\circ}\text{C}$ the particle diameter used was somewhat smaller. However, this change in particle size was not intended but was the result of a problem with salt deposition and subsequent plugging of the oven. More information about the clogging of the furnace is given in section 3.5.1.

Figure 5.8 to 5.10 show the n-nonane saturation ratio $S(T)$ versus the heterogeneous activation probability P_{act} . Two of them namely figure 5.8 and 5.10 feature an phenomenon observed several times leading to activation probabilities that are too high. As mentioned before a set of data usually consists of five points on the heterogeneous activation probability curve: Two points on the slope and three at total activation. If the first point on the slope shows an heterogeneous activation probability nearly equal zero then the subsequent point(the second on the slope) may show an excessive particle activation. This is due to some "contamination" of the chamber that does not appear for points at higher heterogeneous activation probability though the flushing time(see section 3.2) remains the same.

D_p [nm]	T [$^{\circ}\text{C}$]	σ	S_{onset}
$14,66 \pm 0,04$	$-10,3 \pm 0,02$	$1,038 \pm 0,005$	$1,33 \pm 0,07$
$14,68 \pm 0,03$	$-0,1 \pm 0,02$	$1,038 \pm 0,005$	$1,37 \pm 0,07$
$14,2 \pm 0,08$	$+9,7 \pm 0,02$	$1,041 \pm 0,005$	$1,36 \pm 0,07$

Table 5.3: Experimental results for n-nonane nucleation on 15nm sodium chloride seed particles. Column 1 to 3 characterize the experimental conditions: particle diameter D_p , nucleation temperature T and the geometric standard deviation σ of the "monodisperse" aerosol size distribution. The last column features the onset saturation ratio S_{onset} . The errors of D_p , T and σ were statistically determined whereas the error of S was calculated from the geometric standard deviation σ of D_p using the Kelvin equation.

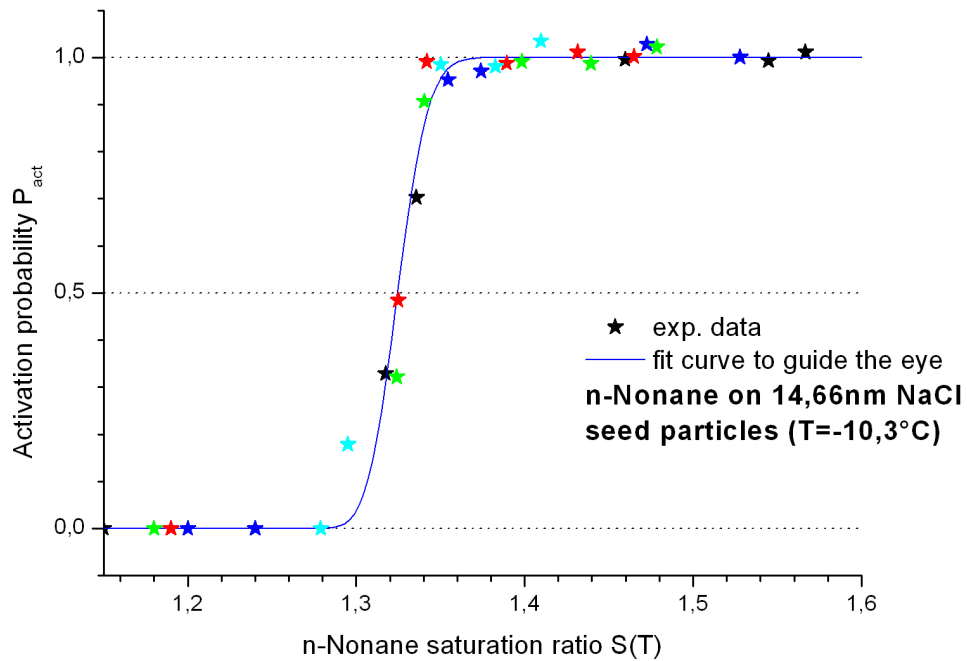


Figure 5.8: The heterogeneous activation probability curve of 15nm sodium chloride particles at $-10,3^{\circ}\text{C}$ determined by the experimental data points which are represented by the star-shaped symbols. Every measurement set is illustrated by a different color. At activation probabilities $P_{act} = [0; 50; 100]\%$ dashed lines are included for better orientation. The solid line represents a hyperbolic tangent function which was manually fitted to the experimental data points to guide the eye.

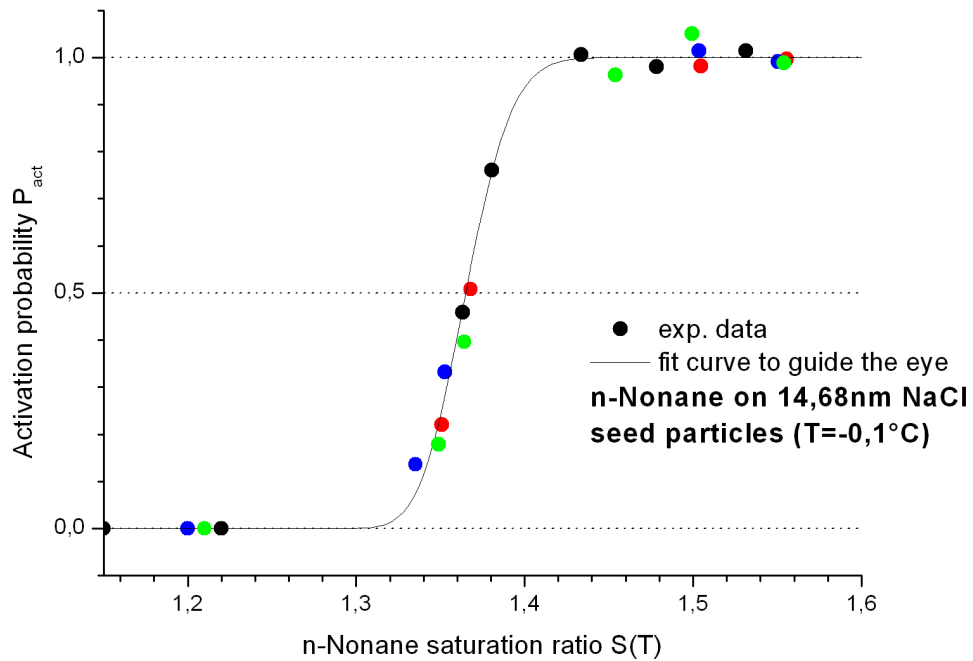


Figure 5.9: The heterogeneous activation probability curve of 15nm sodium chloride particles at $-0,1^{\circ}\text{C}$ determined by the experimental data points which are represented by the circular symbols. At Every measurement set is illustrated by a different color. activation probabilities $P_{act} = [0; 50; 100] \%$ dashed lines are included for better orientation. The solid line represents a hyperbolic tangent function which was manually fitted to the experimental data points to guide the eye.

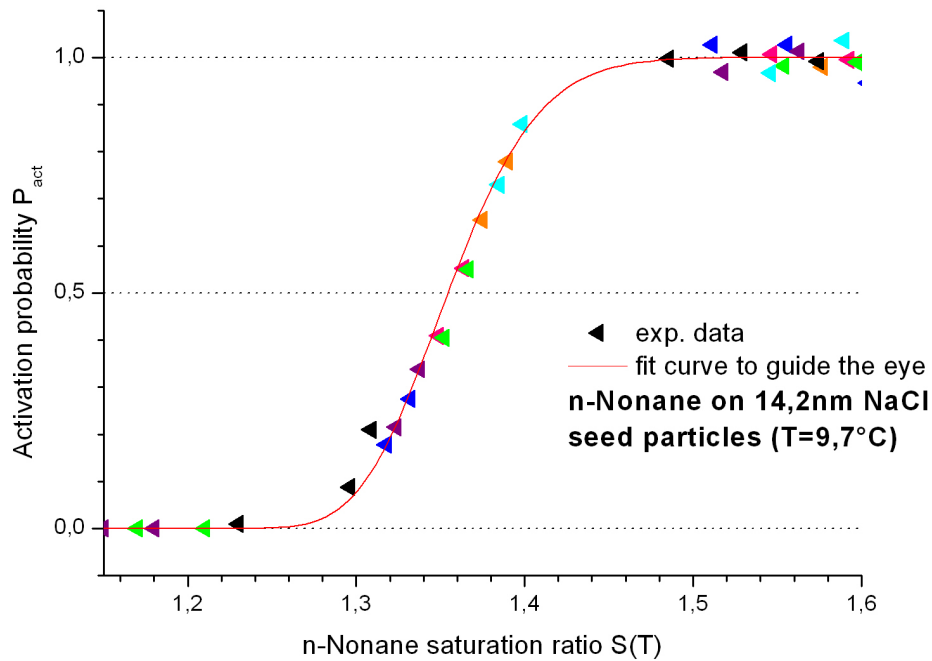


Figure 5.10: The heterogeneous activation probability curve of 15nm sodium chloride particles at $+9,7^{\circ}\text{C}$ determined by the experimental data points which are represented by the triangular symbols. Every measurement set is illustrated by a different color. At activation probabilities $P_{act} = [0; 50; 100]\%$ dashed lines are included for better orientation. The solid line represents a hyperbolic tangent function which was manually fitted to the experimental data points to guide the eye.

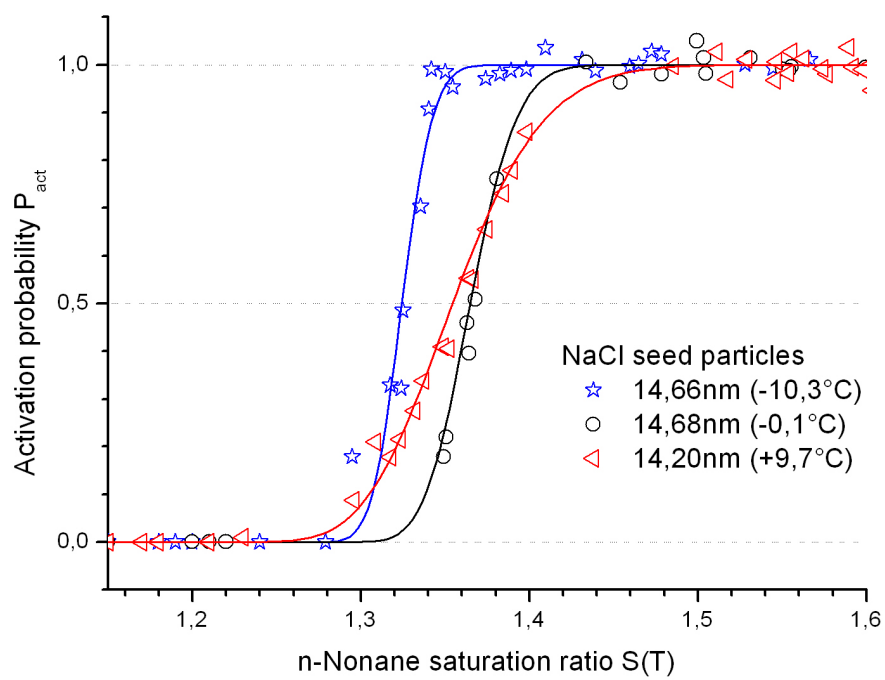


Figure 5.11: Superposition of figures 5.8, 5.9 and 5.10.

5.3 Data analysis

5.3.1 Kelvin curves

The easiest way to get a first impression of the experimental data is to perform Kelvin calculations. The Kelvin equation is extensively discussed in section 2.1. It was derived by considering the classical homogeneous nucleation model but is also valid for heterogeneous nucleation. This equation takes into account the surface tension σ of the liquid, the number of molecules per volume n_l (which is tantamount to the liquid density), the nucleation temperature T and the saturation ratio $S = \frac{p_v}{p_l}$ which is the ratio of vapor pressure p_v and saturation vapor pressure p_l . Solutions of the Kelvin curve describe liquid droplets that are in an unstable thermodynamic equilibrium with the vapor phase. The higher the curvature on the droplet surface (i.e. the smaller its radius) the higher the vapor pressure on the liquid surface. This is also the reason why its validity is not restricted to homogeneous nucleation: The curvature is independent of any seed particle. Figure 5.12 outlines the experimentally obtained onset saturation ratios at each seed particle size and furthermore Kelvin curves for the three different temperatures used for the experiments. It is obvious that the data points are far off the Kelvin curves. This is no surprise as the Kelvin curves predict the critical cluster radius. Still the Kelvin curves may be helpful for data interpretation as will be discussed in section 5.3.2.

5.3.2 Towards the application of the heterogeneous nucleation theorem

In section 2.3 the heterogeneous nucleation theorem was established. It shows the direct relation between nucleation work and critical cluster size. In the case of heterogeneous nucleation the correlation is given by[15]:

$$\frac{d\Delta G^*}{d\Delta\mu} = -i^* \quad (5.6)$$

where ΔG^* is the critical formation work of the cluster, $\Delta\mu$ is the difference in chemical potential (of liquid and vapor phase) and i^* is the number of molecules in the critical cluster. This equation holds true if the excess free energy is independent of $\Delta\mu$ which was found to be a good approximation[15].

Further, a relation between the steepness of the heterogeneous activation probability curve and the number of molecules in the critical cluster was found[50]:

$$i^* = k_B T \frac{d \left(\ln \ln \frac{1}{1-P_{act}} \right)}{d\Delta\mu} - 1 \quad (5.7)$$

where k_B is the Boltzmann constant, T is the temperature in Kelvin and P_{act} is the heterogeneous activation probability which strongly depends on the saturation

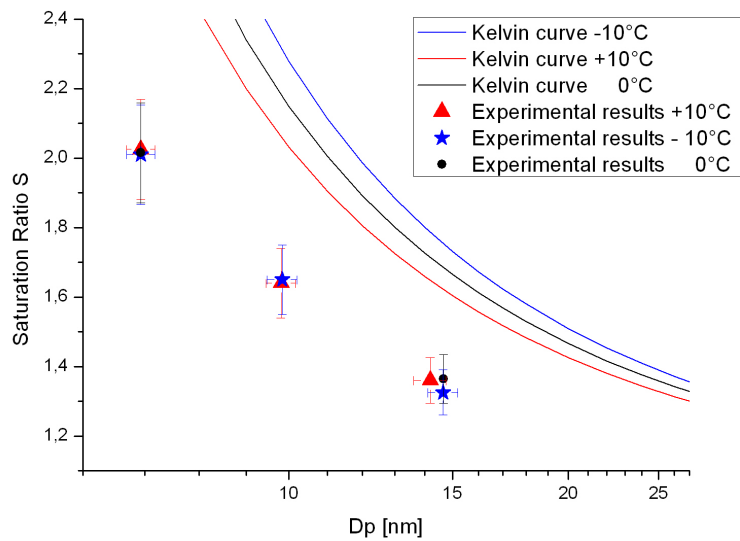


Figure 5.12: The colored lines depict the Kelvin curves showing the critical particle diameter at the critical saturation ratio S which were calculated at $+10^\circ$, 0° and -10° . The experimental data points show the seed particle diameter and the saturation ratio at which half of all seed particles are activated. The error of D_P was statistically determined whereas the error of S was calculated from the geometric standard deviation σ of D_P using the Kelvin equation (see tables 5.2.1 to 5.2.3). Further, the abscissa is in logarithmic scale.

ratio S . If the derivation with respect to $\Delta\mu$ is substituted by a derivation with respect to the natural logarithm of the saturation ratio ($\ln S$) the relation becomes even more obvious and compact:

$$i^* = \frac{d \left(\ln \ln \frac{1}{1-P_{act}} \right)}{d \ln S} - 1 \quad (5.8)$$

The higher the number of condensed molecules in the critical cluster is the steeper the heterogeneous activation probability curve has to be.

Direct application of the nucleation theorem to the experimental data is not possible yet since it requires previous treatment of the experimentally obtained data points. As shown by figure 3.5 in section 3.5.2 the particles used for nucleation experiments are not strictly monodisperse. Since equation 5.8 is valid only in the case of monodisperse seed particles the variance of the particle size has to be removed mathematically. Further a fit curve has to be applied to the data points simultaneously. These fits are currently not available but there is still a possibility to apply the heterogeneous nucleation theorem. Since the contact angle between NaCl and n-nonane was found to be 0° (Pinterich, T.[30]) the seed particle of an activated n-nonane cluster is completely within the liquid droplet as illustrated by figure 5.13.

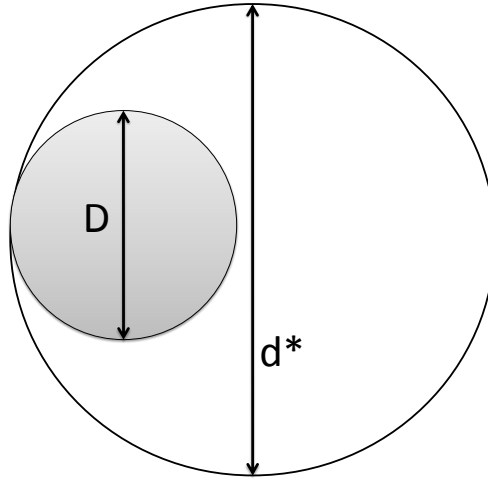


Figure 5.13: The cross section of a critical cluster of radius r^* (obtained using the Kelvin equation) containing a seed particle of diameter D . Due to the contact angle which is 0° between the n-nonane cluster and the NaCl seed particle surface the seed is totally covered with the liquid. The grey area stands for the seed particle whereas the white area depicts the liquid droplet.

Using this fact and further knowing the onset saturation ratio at which a seed particle of known size is activated allows the determination of the liquid volume

and consequently the number of molecules within the droplet(see figure 5.14):

$$i^* = \frac{4\pi}{3} (r^{*3} - R^3) \frac{\rho N_A}{M} \quad (5.9)$$

where r^* is the critical cluster radius obtained using the Kelvin equation(see section 2.1), R is the seed particle radius, ρ is the liquid density in $[gm^{-3}]$, N_A is the Avogadro constant and M is the molar mass.

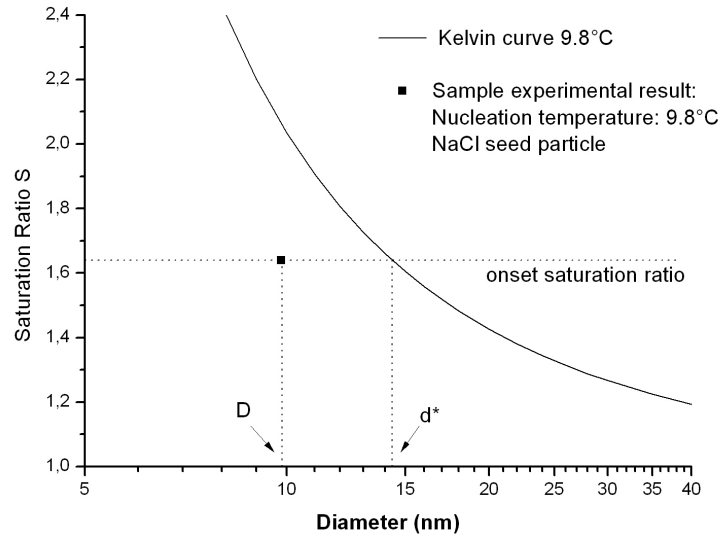


Figure 5.14: The experimentally determined onset saturation for a seed particle featuring diameter D enables the determination of the critical droplet diameter d^* . By way of illustration an experimental data point was picked randomly.

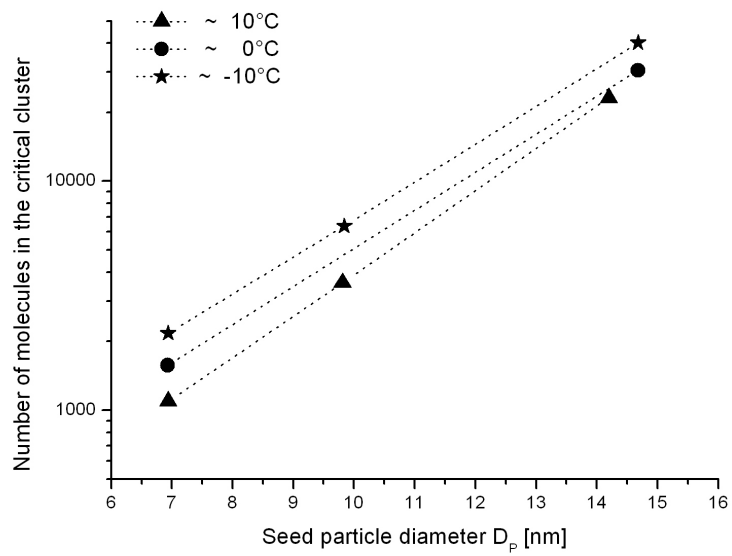


Figure 5.15: The onset saturation ratio at which a seed particle of diameter D is activated combined with the solution of the Kelvin equation at the onset saturation allows the determination of the molecule number in the critical cluster. The experimentally obtained data points for constant nucleation temperatures are linked with dashed lines to guide the eye.

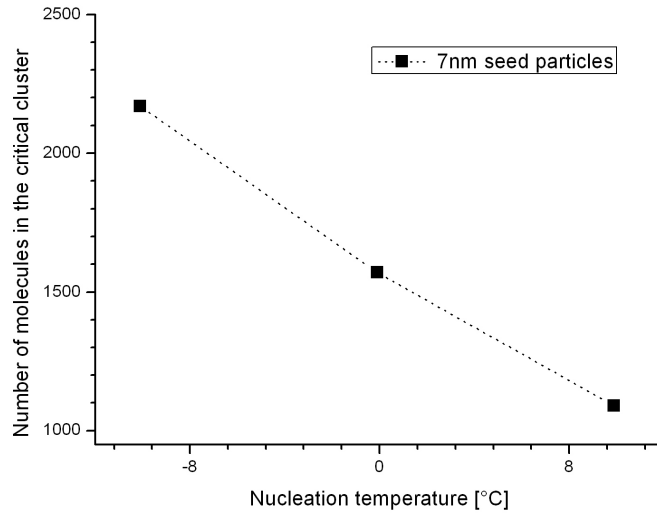


Figure 5.16: The number of molecules in the critical cluster versus nucleation temperature is plotted. The black squares stand for the experimentally investigated seed particle radii. They are linked with dashed lines for better illustration of the temperature trend.

In figure 5.15 the number of molecules in the critical cluster is plotted versus the seed particle diameter. The data points obtained at equal nucleation temperature are linked with dashed lines to guide the eye. It seems that the steepness of the lines is constant in the logarithmic scale. The fitting function might be represented by $i = k * D_P + C$. Beside the data point for "15nm" particles at +10° which appears to differ somehow it further looks like the factor k is the same for all nucleation temperatures. k may be interpreted as a growth factor of the critical cluster depending on the seed particle diameter. For a plot in linear scale (i.e. not logarithmic) this factor k would imply an exponential growth changing the fitting function to $i = C' e^{k * D_P} (T)$ where C' depends on the nucleation temperature whereas k is temperature independent.

Figures 5.16 to 5.18 show the temperature trend of the critical cluster liquid volume. The abscissa stands for the temperature at which the nucleation experiment was carried out and the ordinate depicts the number of molecules in the critical cluster. The latter was obtained in a manner which was discussed earlier in this section. Again the data points are linked with dashed lines to guide the eye. All three figures show a clear trend. The higher the temperature is the lower the number of molecules i^* gets. The progress of the curves seems not to be linear and

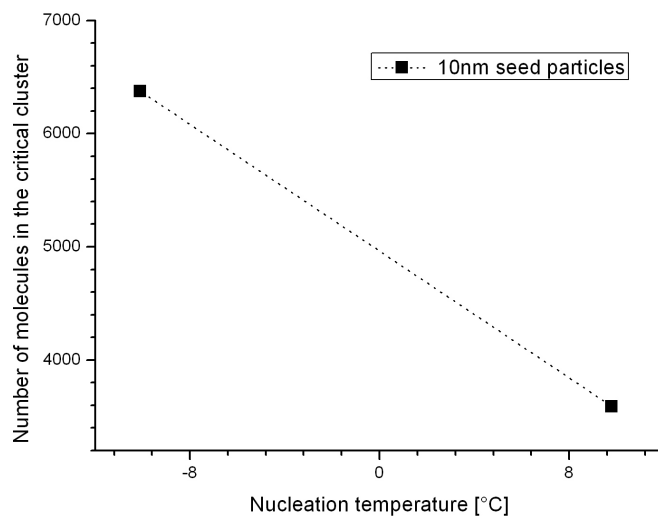


Figure 5.17: The number of molecules in the critical cluster versus nucleation temperature is plotted. The black squares stand for the experimentally investigated seed particle radii. They are linked with dashed lines for better illustration of the temperature trend.

there are too few data points to apply a reasonable fitting function but anyway the trend is clear.

Equation 5.8 depicts the dependence of i^* on the steepness of the heterogeneous activation probability curve. Figures 5.4, 5.7 and 5.11 compare the steepness of the heterogeneous activation probability curves for a given size class of particles. Again, it has to be mentioned that the slope of the heterogeneous activation probability curves still includes the polydispersity of the sodium chloride particles. Nevertheless the slopes may be interpreted since the width of the particle distribution is nearly equal for a given particle size. This means that mathematical removal of the polydispersity does not cause a big change in the slopes' steepness relative to each other.

Figure 5.4 depicts the measurement results for "7nm" particles. The steepest slope was observed for -10° nucleation temperature, the flattest slope in case of $+10^\circ$. As particle sizes were the same for $+10^\circ$, -10° as well as 0° the steepness of the slopes may be directly compared to the number of particles in the critical cluster. Figure 5.16 confirms the temperature trend implied by the heterogeneous activation probability slopes. The lower the nucleation temperature the higher the number of particles in the critical cluster. Equal considerations leading to the same trend can

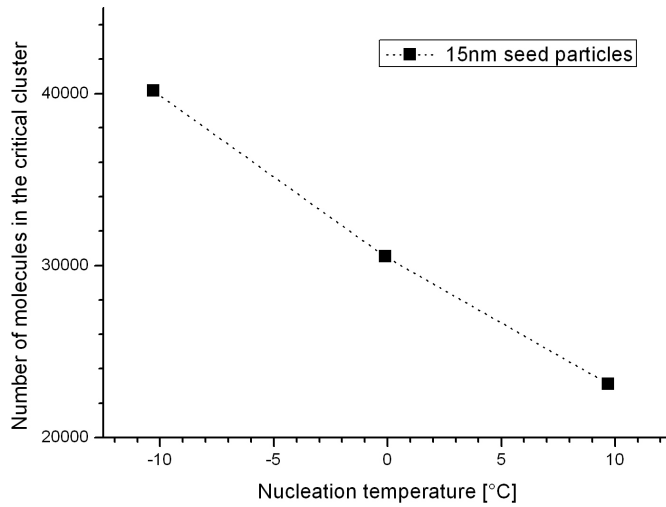


Figure 5.18: The number of molecules in the critical cluster versus nucleation temperature is plotted. The black squares stand for the experimentally investigated seed particle radii. They are linked with dashed lines for better illustration of the temperature trend.

be done for "10nm" particles. In the case of "15nm" particles it is more difficult because the particles are not all of the same (electro mobility equivalent) diameter. At nucleation temperatures of -10° and 0° the particle diameter is about 14.7nm but in case of $+10^\circ$ the particle diameter is 14.2nm. Since figure 5.15 predicts a lower i^* in case of smaller seed particle radii the direct comparison of the slopes is not possible. An option to solve this problem is by assessing i^* for a seed particle diameter of 14.7nm and $+10^\circ$. Figure 5.15 suggests a constant growth factor k in case of logarithmic ordinate. This factor was determined as $k = 0.376$. By multiplying $e^{k \cdot \delta D_P}$, where δD_P is the difference in size of the particles, with the number of molecules of the 14.2nm seed particle i^* for a 14.7nm particle may be estimated. Now the values of i^* for different nucleation temperatures may be compared directly. The trend observed in the cases of 7nm and 10nm is confirmed.

The Kelvin equation predicts smaller critical clusters for higher nucleation temperatures whereas the onset saturation ratios experimentally obtained did not show a clear temperature trend. But if the steepness of the slopes is also taken into account the experimental data show a temperature trend which is similar to that implied by the Kelvin equation.

5.3.3 Fletcher calculations

Performing Fletcher calculations enables the determination of the onset saturation ratio. These calculations allow a direct comparison to the experimental data. To derive the equation one starts with the Kelvin equation 2.13 which interrelates the saturation ratio and the critical cluster diameter. The next step is to insert critical cluster formation work in the Kelvin equation. Now the saturation ratio S depends on the formation work which is connected to the nucleation rate via 2.18. The last step is to insert equation 2.30 for the nucleation rate leading to following expression:

$$(\ln S)^2 = \frac{16\pi}{3} \left(\frac{\sigma_l}{k_B T} \right)^3 \left(\frac{M}{N_A \rho_l} \right)^2 f(m, X) \ln \left[\frac{4\pi R^2 K \Delta t}{-\ln(1-P)} \right]^{-1} \quad (5.10)$$

where σ_l is the liquid surface tension, k_B is the Boltzman constant, T is the absolute temperature in Kelvin, M is the molar mass of the liquid, N_A is the Avogadro konstant, ρ_l is the liquid density, $f(m, X)$ takes into account the ratio of seed particle radius and droplet radius $X = \frac{R}{r^*}$ and the contact angle between the seed particle surface and the liquid rectangular to the phase triple line(i.e.: the line where all three phases have contact). Further, K stands for the kinetic coefficient(see section 2.4), Δt for the nucleation time and P is the heterogeneous activation probability.

Solving this equations for many different $X = \frac{R}{r^*}$ values leads to the so-called Fletcher curves. Due to the fact that this equation is quite elongated and the implicit S dependence of X and K calculations have to be carried out with help of a PC. Therefore a software program was spificically developed. Based on some boundary conditions, the physical and chemical constants that have to be entered at the front page, the software starts an algorithm that converges within some ten repetitions to a value of S that is related to the heterogeneous activation probability set. This means if $P = 0.5$ is choosen the software determines the onset saturation ratio.

Figure 5.19 shows the front page of the Fletcher calculation program. There are four main fields:

- Substance
- Parameter
- X Range
- R Value

At the first field on the left hand side a liquid file is selected. If the desired liquid file does not exist there is the probability to create a new one. When pushing

the "ADD NEW SUBSTANCE" a window including several input fields pops up. Here the parameters for the liquid density, the surface tension and the molar mass are entered. Adding a name and pressing the button "ADD" saves the file to the database. As from now it appears on the front page.

The second field demands the input of the temperature, the nucleation time, the contact angle, the molar mass, the kinetic coefficient (see section 2.4 and the heterogeneous activation probability). There is the possibility to choose if the kinetic coefficient is either entered manually or calculated. This is useful since the calculation of the kinetic factor requires a whole series of physical and chemical parameters that are not easily available. Further, the saturation ratio calculated with help of the Fletcher equation does not strongly depend on the kinetic factor.

The next input field provides the possibility to choose the X-range and its increment used for the calculations. This on the one hand enables to have a look at certain areas of the Fletcher curves and on the other hand allows to set the desired resolution. With help of the R value the starting point of the algorithm is set.

On pressing the "CALCULATE" button a link to another page (which is illustrated in figure 5.20) opens and the calculation starts. On the top of the page is button called "Show/Hide Calculation". On pressing this button the calculation is shown step by step. Again pushing this button hides the data again. The table below shows the results obtained. The first row which is called " $r[nm]$ " indicates the Kelvin radius in nm, the second row shows the Fletcher radius R in nm. Both refer to saturation ratio S which is indicated in the third row. There is also the possibility to save the data to a .dat file. This is carried out by pushing the "DOWNLOAD results.dat FILE" button which is located at the bottom of the page.

SUBSTANCE

n-Nonan [ADD NEW SUBSTANCE](#)

PARAMETER

Temperature: Kelvin Density: 733034.115 g/m³

Nucleation time: sec Surface tension: 0.024804685 N/m

Contact angle: ° Grad

Molar mass (substance): g

Kinetic Coefficient: [MANUALLY](#) / [CALCULATED](#)

Heat of evaporation: kJ/kg

Vapor pressure: Pa

Parameter Lennard Jones Potential:

Sigma: Angström

Epsilon / Boltzmannkonstante: Kelvin

Stockmayer Potential: (for polar liquids)

Activation probability:

X Range]0;1[X=Rseed/r*

from to

Increment:

R Value

R =

Figure 5.19: Front page of the Fletcher calculation program.

RESULTS

Show/Hide Calculation

VALUES		
r [nm]	R [nm]	S
2.9325071484107	2.3460057187286	3.681551003687
3.0749797835723	2.4907336246936	3.4658119088742
3.2337026413528	2.6516361659093	3.2606879264279
3.4115839334201	2.8316146647387	3.0658090041141
3.6122671623311	3.0343044163581	2.880809766119
3.840378437766	3.2643216721011	2.7053301743141
4.1018805950765	3.5276173117658	2.5390161768429
4.4045920091875	3.8319950479931	2.3815203569366
4.7589668239249	4.1878908050539	2.2325026007478
5.1793040866816	4.6095806371466	2.0916308123429
5.68568809875	5.117119288875	1.9585817194434

DOWNLOAD results.dat FILE

Figure 5.20: From the results of the Fletcher calculations the program compiles a table(the values in the table shown above are arbitrary). The calculation may be viewed step by step optionally. Further, there is the possibility to download the data.

Fletcher calculations were carried out for three different nucleation temperatures: $-10, 2^{\circ}C$, $-0, 1^{\circ}C$ and $+9, 8^{\circ}C$ using the software program described in this section. The chemical and physical constants were calculated using the following equations:

- surface tension[54] in $\frac{N}{m}$: $\sigma = 0,05761 - T * 0,0001201$
- liquid density[19] in $\frac{kg}{m^3}$: $\rho = 942,786 - T * 0,7679$
- saturation vapor pressure[3] in Pa: $lnps = (48,33129 - \frac{6363,02}{T} - 3,602671lnT$
- latent heat of vaporization[40] in $\frac{J}{kg}$: $L = 4,124593 * 10^5 - T * 2,3355 * 10^3$
- The potential of two molecules was approximated using the Lennard-Jones potential U[47] in Joule: $U = 4\epsilon \left(\left(\frac{\sigma}{r} \right)^{12} - \left(\frac{\sigma}{r} \right)^6 \right)$ with $\frac{\epsilon}{k_B} = 912,04 - T^{0,5} * 17,918$

Further parameters used for the calculations are the contact angle between the seed particle surface and the liquid rectangular to the phase triple line (i.e.: the line where all three phases have contact) which is 0° [30], the molar weight $M = 128,26g$ and the nucleation time Δt . Approximation of the nucleation time was done by evaluating the experimental data. As explained in section 3.1 the saturation ratios necessary to activate particles are achieved by performing an adiabatic pressure drop. The experimental data includes information about the duration of the pressure drop as well as the time of appearance of the first scattering maximum (see section 3.3). The nucleation time is smaller than the time of appearance of the first maximum because at that time the droplets have already grown to a size about 100 times the size of the seed. Assessing the lower limit of the nucleation time is not as superficial since the pressure drop is no stepfunktion. In case of a stepfunktion it would be possible to calculate the time at which the clusters have exceeded the critical diameter by applying droplet growth theory for constant S. Times of appearance of the first scattering maximum were typically around 10ms to 20ms depending on the saturation ratio and the temperature. Δt was chosen as 15ms for the calculations. Calculations with nucleation times of double and half duration have not shown noticeable differences in the result.

Figure 5.21 compares the results of the Fletcher calculations with the Kelvin curves for the same nucleation temperatures. As can be seen the Fletcher curves predict particle activation at lower saturation ratios than the Kelvin curves. However, this is no surprise since the Kelvin curves indicate at which droplet surface curvature the vapor pressure above the surface is equal to the ambient vapor pressure. Therefore the droplet is situated in an unstable thermodynamic balance. Whereas the Fletcher curves predict the onset saturation ratio which is the saturation ratio

leading to a particle activation of 50%. More surprisingly the temperature trend is the same for both Fletcher and Kelvin curves. The latter predicts a slightly stronger temperature trend but apart from that and the foresaid higher saturation ratios of the Kelvin curve the curves look pretty resembling.

Figure 5.22 to 5.24 depict the onset saturation ratio at given particle size (i.e. the Fletcher curve) in comparison with the Kelvin curve and the experimental data. Each of the first-mentioned stands for a constant nucleation temperature. All of them show Fletcher curves that lie well below the Kelvin curve and the experimentally determined onset saturation ratios lie well below the Fletcher curves. Since the experimental data points show no appreciable temperature trend at all and the Fletcher curves predict a lower onset for higher temperatures the difference between them reduces for increasing temperature. The error bars in direction of the abscissa shown in this figures were set to the geometric standard deviation of the sodium chloride particle size (see section 5.1.2). The error bars parallel to the ordinate were calculated as described in section 5.1.2.

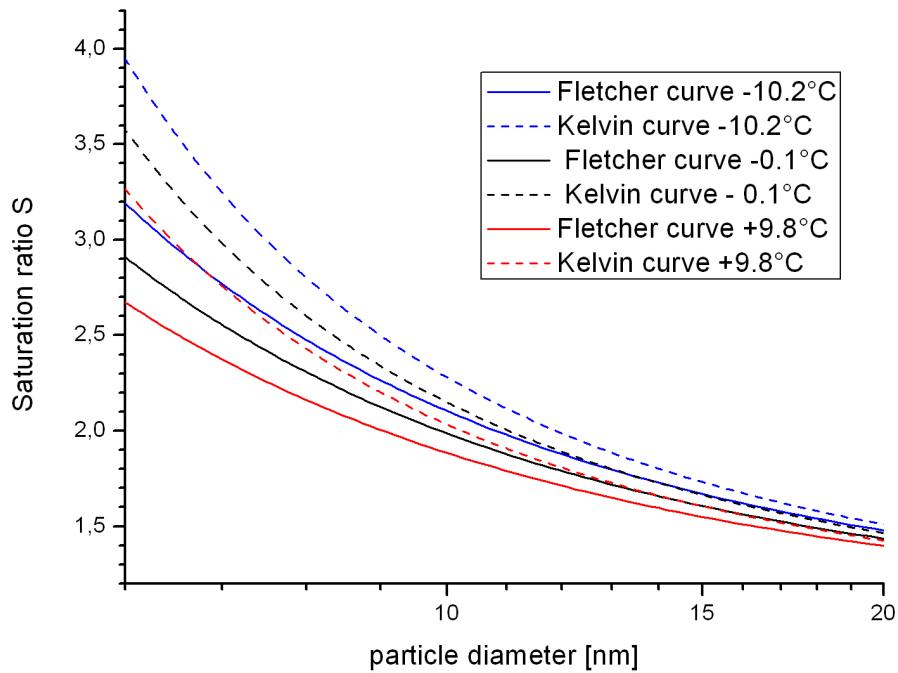


Figure 5.21: The Fletcher curves which are represented by the solid lines calculated with the programmed software are compared with Kelvin curves (dashed lines). Therefore nucleation temperatures entered in the equations were chosen equally to experimental. Both Kelvin and Fletcher curves were calculated for $-10,2^{\circ}\text{C}$, $-0,1^{\circ}\text{C}$ and $+9,8^{\circ}\text{C}$. The curves at high temperatures are illustrated by red color, the ones for $-0,1^{\circ}\text{C}$ are represented by the black lines and the blue lines stand for $-10,2^{\circ}\text{C}$.

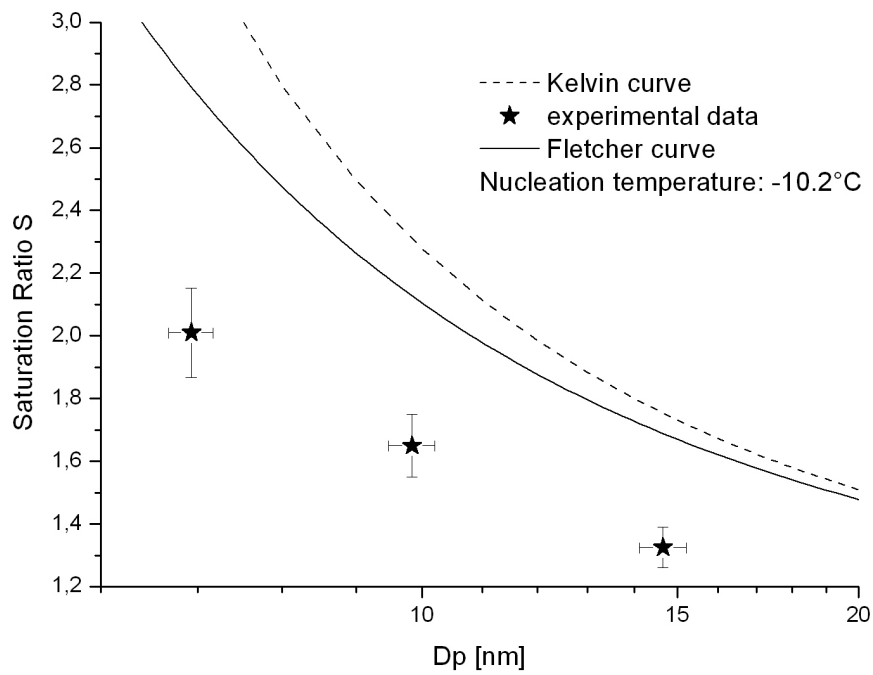


Figure 5.22: The saturation ratio S is plotted versus the seed particle diameter D_p . The solid line depicts the Fletcher curve calculated for a nucleation temperature of $-10, 2^\circ\text{C}$, the dashed line for the Kelvin curve at the same temperature. The black stars show the experimentally obtained data points, also for $-10, 2^\circ\text{C}$. The abscissa is logarithmically scaled.

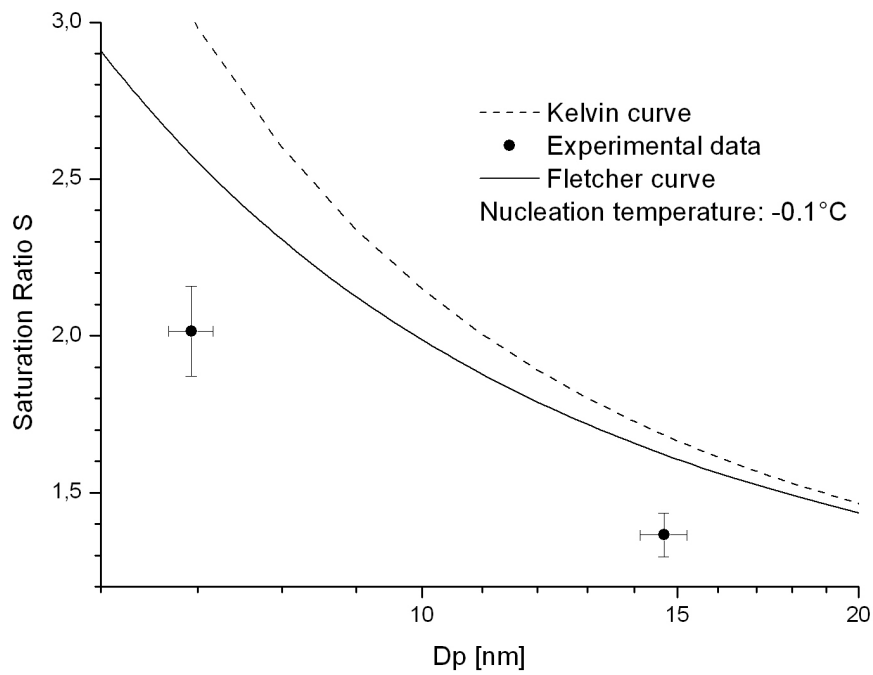


Figure 5.23: The saturation ratio S is plotted versus the seed particle diameter D_p . The solid line depicts the Fletcher curve calculated for a nucleation temperature of $-0,1^\circ\text{C}$, the dashed line for the Kelvin curve at the same temperature. The black stars show the experimentally obtained data points, also for $-0,1^\circ\text{C}$. The abscissa is logarithmically scaled.

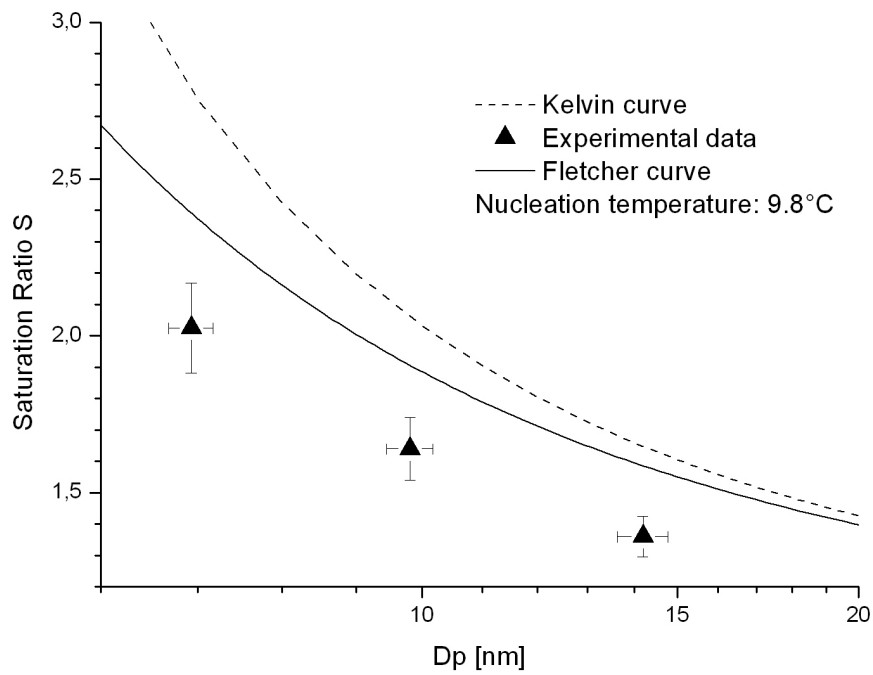


Figure 5.24: The saturation ratio S is plotted versus the seed particle diameter D_P . The solid line depicts the Fletcher curve calculated for a nucleation temperature of $9,8^\circ\text{C}$, the dashed line for the Kelvin curve at the same temperature. The black stars show the experimentally obtained data points, also for $9,8^\circ\text{C}$. The abscissa is logarithmically scaled.

5.3.4 Possible influence of "line tension"

The concept of line tension was first mentioned by Gibbs in 1875[10]. Rowlinson et al.[37] defined the line tension as "...the excess free energy in the three-phase system attributable to unit length of the three phase system." The effect of line tension on the microscopic contact angle and the excess free energy function is treated by Lazaridis[20]. He introduced a modification of Young's law(see equation 2.22):

$$\sigma_{lv}\cos\Phi = \sigma_{sv} - \sigma_{sl} - \frac{\sigma_t}{R\tan\Phi} \quad (5.11)$$

where Φ is the contact angle, σ_{ij} is the surface tension of the interface between phase i and j features, s stands for solid, v for vapor and l for liquid. The seed particle radius R also enters the equation. The modified law predicts bigger microscopic contact angles as long as σ_t is positive. As a result the excess free energy of the cluster increases leading to a lower nucleation rate. This is inconsistent regarding experimental results[22] which show higher nucleation rates than predicted by the classical nucleation theory. According to Scheludko et al.[39] the line tension may also be negative leading to nucleation rates that exceed the classical.

Wang et al.[55] estimated the characteristic influence length of the line tension to be about 10^{-8}m to 10^{-6}m but did not mention a dependence on the cluster radius. Whereas Hienola et al.[11] who estimated the line tension based on experimental data found that the modulus of the line tension rapidly decreases for critical cluster radii falling below 5nm. From $3,75 * 10^{-10}\text{N}$ at 12,77nm cluster radius to $3,4 * 10^{-13}\text{N}$ at 5,3nm cluster radius. Further, they found that the line tension vanishes for wetting(i.e. contact angle of 0°). Theoretic treatment of the aforementioned predicts values going to infinity[14]. However, a line tension equal zero for wetting appears to be more plausible than an infinite. Therefore it should not play a role in this work since the contact angle was determined as zero[30].

5.3.5 A further way of vapor deposition

The classical nucleation theory treated in chapter 2 considers direct vapor deposition as the only way of cluster growth. This means the cluster may increase its number of vapor molecules only by physically being hit by the last mentioned. The effect on this work appears in terms of the kinetic coefficient(see section 2.4) which determines the kinetics of droplet growth. But there is also another possibility of vapor deposition to the cluster. Surface diffusion takes into account the vapor molecules hitting the seed particle after which they diffuse to the liquid cluster. Earlier studies on surface diffusion[13],[32] have shown that in case of iodide nucleation on glass particles the critical clusters mainly formed from surface diffusion. This in fact is contrary to the classical nucleation theory stating direct deposition as the only way of vapor deposition.

Lazaridis[20] developed a term taking into account the surface diffusion. He described the vapor molecules on the particle surface as a two dimensional solution. This way he considered the restricted particle motion on the surface. In the case of direct vapor deposition the growth rate β was determined as (see section 2.4):

$$\beta = \frac{Ap_s}{\sqrt{2\pi mk_B T}} \quad (5.12)$$

For vapor deposition by surface diffusion this term is replaced by:

$$\beta = 2\pi R \sin\Phi d c^{ads} \nu e^{\frac{-L}{k_B T}} \quad (5.13)$$

where R is the seed particle radius, $\Phi = \arccos \frac{X-m}{g}$, d is the jump distance of a molecule, L is the latent heat of evaporation per molecule, c^{ads} is the concentration of monomers on the particle surface where they vibrate with frequency ν , k_B is the Boltzmann constant and T is the temperature in Kelvin. For further information on the variables see section 2.4. Calculations using the latter expression for β showed higher nucleation rates than the classical approach. The nucleation rates obtained this way were even higher than the classical taking into account the line tension[20]. The surface diffusion approach showed better agreement with experimental data than the classical nucleation theory[17]. It also seems to be a more realistic model.

6 Conclusion

6.1 Summary of achievements

In this work the temperature dependence of n-nonane nucleation on sodium chloride particles was investigated. Nucleation temperatures were chosen as -10°C , 0°C and $+10^{\circ}\text{C}$. Particle sizes ranged from 7nm to 15nm in diameter. Earlier experiments have shown that sodium chloride particles may shrink if they get in contact with the working fluid vapor[29],[42]. Thus particle shrinkage was also investigated in this work.

Experiments and results on particle shrinkage are depicted in chapter 4. As described in the section mentioned particles were mixed with a gas carrying the n-nonane vapor and passed on to the analyzer. The experiments were carried out at a quite high relative humidity (68% to 84%). There was no significant change in particle size observed. Further, the slight changes in size observed were within the statistical measurement uncertainty and were explained by the "natural" shrinkage which is introduced in section 3.5.1. It is due to the fact that the primary NaCl size distribution produced by the tube furnace experiences a shift throughout a measurement day[33]. This shift was observed every day. The particle size during an experiment was fitted by linear regression of the data measured before and after the experiment.

Particle activation probabilities (i.e. the ratio of activated over total particle concentration) were measured in dependence of the saturation ratio S . The onset saturation ratios of the curves were determined at 50% activation and compared with theoretically calculated onset saturation ratios[7] (also referred to as Fletcher curves). The latter were significantly higher for all nucleation temperatures. Further, the experimental onsets showed no clear temperature trend whereas the Fletcher curves predict earlier activation for higher temperatures. It has to be mentioned that the calculations are based on the classical nucleation theory and do not account for concepts like line tension or vapor deposition to the liquid cluster by surface diffusion (see sections 5.3.4 and 5.3.5).

Another possibility to interpret the data is to perform Kelvin calculations that predict the radius of a cluster in thermodynamic equilibrium with the ambient gas phase (also referred to as the critical cluster). The same temperature trend as calculated for Fletcher curves is forecast by the Kelvin equation. Direct comparison with the particle diameter at the onset is not possible as it is not the Kelvin diameter. The difference between the Kelvin diameter and the seed particle diameter is in case of 0° contact angle simply given by the number of liquid molecules in the

critical cluster. This number is linked via the 1.HNT(Heterogeneous Nucleation Theorem) to the slope of the activation probability curves[15]. Assessment of the number of molecules in the critical cluster(see section 5.3.2) confirms the temperature trend implied by Kelvin.

Further, there seems to be a linear dependence of the logarithmic number of molecules in the critical cluster on the seed particle diameter(see section 5.3.2).

6.2 Problems

One of the major problems dealt with was the low vapor pressure of the working fluid n-nonane. This affected the accomplishment of the experiment in various ways.

For experiments at $-10^{\circ}C$ and for 15nm seed particles infusion rates were extremely low. As explained in chapter 3 the liquid was pushed through a micro orifice producing a liquid beam. This beam was consequently evaporated in a heated cylinder. To produce a liquid beam of about $40\mu l min^{-1}$ a micro orifice with an inner diameter of $10\mu m$ was used. Due to the small aperture the orifice was clogged nearly every day. Sometimes it took up to several hours to create a liquid beam.

Another effect of the low vapor pressure is contamination of the measurement system which happens when the saturation ratio of the vapor gets too high in any part of the measurement system. If this happens, it takes long flushing periods with pure air to remove the n-nonane residuals. To avoid contamination the relative humidity has to be considered in every part of the measurement system and for every single experiment.

The time period needed to clean the chamber after an expansion had to be much longer than for other liquids. Especially since the flushing was carried out using the aerosol. The nucleation temperature is dependant on the pressure drop and the aerosol temperature in the chamber. For low chamber temperatures the incoming aerosol is comparatively warm leading to comparatively fast removal of the liquid residuals. Whereas for high nucleation temperatures the flushing gas entered the chamber at comparatively low temperature. As a result the saturation vapor pressure of the gas was lower and smaller amounts of liquid could evaporate into the gas. In case of n-nonane nucleation at $+10^{\circ}C$ effective flushing was not possible any more whereby the chamber was contaminated by the working fluid within some 15 expansions.

A quite time-consuming problem appeared in context with the heat conductivity of the aerosol. As mentioned before the nucleation temperature depends on the chamber temperature and the pressure drop. The size of the pressure drop is measured and the chamber temperature too. If the delay time of the gas within

the chamber is not long enough, the aerosol temperature differs from the chamber temperature making an accurate determination of the nucleation temperature impossible. Many measurement sets were carried out at too low delay times. This data is meaningless because the conditions were not well defined.

The last problem discussed in this section is about the scattered light. There was a breakdown observed in the scattered light making the signal vanish for several ms. This breakdown was observed for all experimental conditions but the time of appearance was not constant. Sometimes the first scattered light maximum was only partly visible. This was the worst case since it is the maximum which is most qualified to determine the particle concentration. Of course other maxima can also be used to evaluate particle concentration but the result is not as stable.

6.3 Future investigations

An accurate investigation of the activation probability curves would be very interesting. To do so, the experimental activation probability curves are plotted versus the saturation ratio. Then a function has to be fitted to the data points. In chapter 5 a hyperbolic tangent function was fitted to the experimental data. This function seems to be a good approximation at first glance, but it is not consistent from the physical point of view. Such a physically consistent fitting function was developed by Vrtala[52]. These fits could not be included into this work because of a lack of time, but as soon as possible, this time consuming fitting procedure will be carried out. Application of the first nucleation theorem to the physically constant fitting curves should establish clarity whether the experimental data supports the Kelvin equation or not. Further, there might be the possibility to apply the second nucleation theorem which gives information on the critical cluster energy[9].

As mentioned in section 5.3.5 in the classical nucleation theory only direct vapor deposition from the vapor phase contribute to cluster growth. Another possibility for vapor molecules to reach the cluster is by surface diffusion. They impact on the seed particle and reach the cluster by diffusion. Lazaridis[20] showed that vapor deposition caused by surface diffusion contributes significantly to cluster growth. As a result the classical heterogeneous nucleation theory overestimates the energy barrier a cluster has to overcome.

Including the surface diffusion to the Fletcher calculations would allow increased accuracy.

References

- [1] F.F. Abraham. Multistate kinetics in nonsteady-state nucleation: a numerical solution. *J. Chem. Phys.*, 51:1632, 1969.
- [2] J. Aitken. On the number of dust particles in the atmosphere. *Transactions of the Royal Society of Edinburgh*, 35:1, 1888.
- [3] The chemical Rubber Co. *CRC Handbook of Chemistry and Physics*. Cleveland, Ohio, 1979. 60th Edition.
- [4] E. Cunningham. On the velocity of steady fall of spherical particles through fluid medium. *Proc. R. Soc. Lond. A.*, 83:357–365, 1910.
- [5] J. Dalton. Experimental essays on the constitution of mixed gases; on the force of steam or vapor on water or other liquids in different temperatures; both in torecellian vacuum and in air; on evaporation; and on the expansion of gases by heat. *Mem. Manchester Lit. Phil. Soc.*, 5:535, 1802.
- [6] P. Debye. Lichtdruck auf kugeln von beliebigem material. *Annalen der Physik*, 30:57–137, 1909.
- [7] N.H. Fletcher. Size effect in heterogeneous nucleation. *J. Chem. Phys.*, 29:572, 1958.
- [8] N.H. Fletcher. *The Physics of Rain Clouds*. Cambridge University Press, 1962.
- [9] I.J. Ford. Properties of ice clusters from an analysis of freezing nucleation. *J. Phys. Chem. B*, 105:11649–11655, 2001.
- [10] J.W. Gibbs. *The Collected Papers of J. Willard Gibbs Vol. I*. London: Yale University Press, 1957.
- [11] A.I. Hienola, P.M. Winkler, P.E. Wagner, H. Vehkamäki, A. Lauri, I. Napari, and M. Kulmala. Estimation on line tension and contact angle from heterogeneous nucleation experimental data. *J. Chem. Phys.*, 126:94705, 2007.
- [12] W.C. Hinds. *Aerosol Technology*. John Wiley & sons, Canada, 1982.
- [13] K.C. Ho and J.R. Maa. Surface diffusion and heterogeneous nucleation on solid substrates. *Journal of Colloid and Interface Science*, 85:413–421, 1982.
- [14] J.F. Joanny and P.G. De Gennes. Role of long-range forces in heterogeneous nucleation. *J. Coll. Int. Sci.*, 111:94–101, 1986.

- [15] D. Kashchiev. On the relation between nucleation work, nucleus size, and nucleation rate. *J. Chem. Phys.*, 76:5098, 1982.
- [16] Lord Kelvin. On the equilibrium of vapour at a curved surface of a liquid. *Proc. Roy. Soc. Edinb.*, 7:63, 1870.
- [17] J.A. Koutsky, A.G. Walton, and E. Baer. Heterogeneous nucleation of water vapor on high and low energy surfaces. *Surface Science*, 3:165–174, 1965.
- [18] L. Krämer, U. Pöschl, and R. Niessner. Microstructural rearrangement of sodium chloride condensation aerosol particles on interaction with water vapor. *J. Aerosol Sci.*, 31:673, 2000.
- [19] M. Kulmala, T. Vesela, and J. Kalkinen. Data for phase transitions in aerosol systems. *Manuscript for laboratory use, University of Helsinki*, 1991.
- [20] M. Lazaridis. The effects of surface diffusion and line tension on the mechanism of heterogeneous nucleation. *J. Coll. Int. Sci.*, 155:386–391, 1993.
- [21] M. Lazaridis, M. Kulmala, and A. Laaksonen. Binary heterogeneous nucleation of a water-sulphuric acid system: the effect of hydrate interaction. *J. Aerosol Sci.*, 22:823, 1991.
- [22] P.C. Mahata and D.J. Alofs. Insoluble condensation nuclei: The effect of contact angle, surface roughness and adsorption. *Journal of the Atmospheric Sciences*, 32:116–122, 1975.
- [23] A. E. Majerowicz. *Experimental investigation of brownian coagulation processes of well-defined ultrafine aerosols in a steady state flow system*. PhD thesis, University of Vienna, 1993.
- [24] P.H. McMurry. A review of atmospheric aerosol measurements. *Atmospheric environment*, 34:1959–1999, (2000).
- [25] G. Mie. Beiträge zur optik trüber medien, speziell kolloidaler metallösungen. *Annalen der Physik*, 25:377, 1908.
- [26] A. Milcheva, Vassileva E., and Kertov V. Electrolytic nucleation of silver on a glassy carbon electrode: Part i. mechanism of critical nucleus formation. *Journal of Electroanalytical Chemistry*, 107:323, 1980.
- [27] A. Moshfegha, M. Shamsa, G. Ahmadib, and R. Ebrahimic. A novel surface-slip correction for microparticles motion. *Colloids and Surfaces A: Physico-chemical and Engineering Aspects*, 345:112–120, 2009.

- [28] A.E. Nielson. *Kinetics of Precipitation*. Pergamon, Oxford, 1964.
- [29] D. Peterson. *Experimental investigation on condensation of superaturated vapors on nanoparticles applying a newly developed laser scattering system*. PhD thesis, University of Vienna, 2001.
- [30] T. Pinterich. *Contact angle measurement between n-nonane and NaCl using the washburn method*. Boltzmannngasse, University of Vienna, 2010.
- [31] O. Preining, P.E. Wagner, F.G. Pohl, and W. Szymanski. *Aerosol Research at the Institute for Experimental Physics of the University of Vienna. Part III*, Institut of Experimental Physics, University of Vienna, 1981.
- [32] H.R. Puppacher and J.C. Pflaum. Some characteristics of ice-nucleation active sites derived from experiments with a ferroelectric substrate. *Journal of Colloid and Interface Science*, 52:543–552, 1975.
- [33] G.P. Reischl. *private communication*. 2010.
- [34] G.P. Reischl, J.M. Mäkelä, and J. Neced. Performance of vienna type differential mobility analyzer at 1.2 to 20nm. *Aerosol Sci. Tec.*, 27:651–672, 1997.
- [35] G.P. Reischl, H.G. Scheibel, and J. Porstendörfer. The bipolar charging of aerosols. *Colloid interface Sci.*, 91:272–275, 1983.
- [36] F. Richarz. Der wert des verhältnisses der beiden spezifischen wärmen für ein gemisch zweier gase, insbesondere für ozonhaltigen sauerstoff. *Annalen der Physik*, 19:639–648, 1906.
- [37] J.S. Rowlinson and B. Widom. *Molecular Theory of Cappillarity*. Oxford: Oxford University Press, 1989.
- [38] H.G. Scheibel and J. Porstendörfer. Generation of monodisperse ag- and nacl-aerosols with particle diameters between 2 and 300nm. *J. Aerosol Science*, 14:113, 1983.
- [39] A. Scheludko, V. Chakarov, and B. Toshev. Water condensation on hexadecane and linear tension. *Transactions of the Royal Society of Edinburgh*, 82:83–92, 1981.
- [40] T. Schmeling and R. Strey. Equilibrium vapor-pressure measurements for the n-alcohols in the temperature-range from $-30c$ to $+30c$. *Berichte Der Bunsen-Gesellschaft-Physical Chemistry Chemical Physics*, 87:871, 1987.

- [41] J.W.P. Schmelzter. *Nucleation Theory and Application*. Wiley-VCH, Weinheim, Deutschland, 2005.
- [42] S. Schobesberger. Experiments on the temperature dependence of heterogeneous nucleation of n-propanol vapor on nanosized nacl and ag particles, 2008.
- [43] J.H. Seinfeld. *Atmospheric Chemistry and Physics of air pollution*. California Institute of Technology, Pasadina, 1985.
- [44] R.A. Sigsbee. *Nucleation*. Dekker, New York, 1969. p.151.
- [45] D. Stauffer. Kinetic theory of two-component ("hetero-molecular") nucleation and condensation. *J. Aerosol Sci.*, 7:319, 1976.
- [46] D. Stauffer. Two komponent heterogeneous nucleation kinetics and application to mars. *J. Chem. Phys.*, 127:134710, 2007.
- [47] T. Sun and A.S. Teja. An equation of state for real fluids based on the lennard-jones potential. *J. Chem. Phys*, 100:17365–17372, 1996.
- [48] W.W. Szymanski and P.M. Wagner. Absolute aerosol number concentration measurement by simultaneous observation of extinction and scattered light. *J. Aerosol Science*, 39:441–451, 1990.
- [49] J. Timmermanns. *Physico-Chemical Constants of Pure Organic Compounds*. Elsevier, New York, 1965.
- [50] H. Vehkamäki, A. Määttänen, A. Lauri, M. Kulmala, P.M. Winkler, and P.E. Wagner. Heterogeneous multicomponent nucleation theorems for the analysis of nanoclusters. *J. Chem. Phys.*, 126:174707, 2007.
- [51] A. Vrtala. *REDUCE (SANC Data Reduction Software)*. Institut of Experimental Physics, University of Vienna, 3.1 edition, 2002.
- [52] A. Vrtala, P.M. Winkler, H. Vehkamäki, M. Kulmala, and P.E. Wagner. Description of heterogenous nucleation using a physically consistent heterogenous nucleation probability function(pchnpf). *18th International Conference, Nucleation and Atmospheric Aerosols, Prague, Czech Republic*, pages 508–511, 2009.
- [53] P.E. Wagner. A constant-angle mie scattering method (cams) for investigation of particle formation process. *Journal of Colloid and Interface Science*, 105:456–467, 1985.

- [54] P.E. Wagner and R. Strey. Measurements of homogeneous nucleation rates for n-nonane vapor using a 2-piston expansion chamber. *J. Chem. Phys.*, 80:5266–5275, 1984.
- [55] J.Y. Wang, S. Betelu, and B.M. Law. Line tension approaching a first-order wetting transition: Experimental results from contact angle measurements. *Phys. Rev. E*, 63:31601, 2001.
- [56] J.D. Weeks and G.H. Gilmer. Dynamics of crystal growth. *Advances in Chemical Physics*, 40:157, 1979.
- [57] P.M. Winkler, G. Steiner, A. Vrtala, H. Vehkamäki, M. Noppel, K.E.J. Lehtinen, G.P. Reischl, P.E. Wagner, and M. Kulmala. Heterogeneous nucleation experiments bridging the scale from molecular ion clusters to nanoparticles. *Science*, 319:1374–1377, 2008.
- [58] P.M. Winkler, G. Steiner, A. Vrtala, H. Vehkamäki, M. Noppel, K.E.J. Lehtinen, G.P. Reischl, P.E. Wagner, and M. Kulmala. Heterogeneous nucleation experiments bridging the scale from molecular ion clusters to nanoparticles (support material). *Science*, 319:1374–1377, 2008.

List of Figures

2.1	The formation energy ΔG_i as a functions of the cluster radius r for different saturation ratios.	6
2.2	Depicts a three phase system: the vapor phase V, the solid phase S and the liquid phase L which is in fact the cap embryo. r is the radius implied by the surface curvature of the embryo and Φ denotes the contact angle between the solid and the liquid phase.	8
2.3	R is the radius fo the spherical seed particle and r^* is the radius of the spherical cap embryo of critical size.	9
3.1	The SANC Cycle	21
3.2	Light path through the chamber	22
3.3	Experimental Setup	25
3.4	Aerosol size distribution produced by the tube furnace at $890K$. The abscissa shows the particle diameter $[D]$, the ordinate depicts the number concentration $\frac{dN}{dn(D)}$	27
3.5	Aerosol size distribution produced by the tube furnace at $615^\circ C$. The abscissa shows the particle diameter $[D]$, the ordinate depicts the number concentration $\frac{dN}{dnD}$. The mean geometric diameter is $6,99nm$ and the standard deviation (referring to a Gauss-fit) $\sigma = 1,0355$	30
3.6	Decreasing particle mean geometric diameter monitored throughout a measurement day (17.09.2009).	31
4.1	Setup of particle humidifying to observe possible reduction of the mobility equivalent diameter	34
4.2	Result of measurements on sodium chloride particle shrinkage in n-nonane vapor. The electro mobility equivalent diameter of the particles was set to $7nm$ using the EAC(see chapter 3).	38
4.3	Result of measurements on sodium chloride particle shrinkage in n-nonane vapor. The electro mobility equivalent diameter of the particles was set to $10nm$ using the EAC(see chapter 3).	39
4.4	Result of measurements on sodium chloride particle shrinkage in n-nonane vapor. The electro mobility equivalent diameter of the particles was set to $15nm$ using the EAC(see chapter 3).	40

5.1	The heterogeneous activation probability curve of 7nm sodium chloride particles at $-10, 1^{\circ}C$ determined by the experimental data points which are represented by the star-shaped symbols. Every measurement set is illustrated by a different color. At activation probabilities $P_{act} = [0; 50; 100] \%$ dashed lines are included for better orientation. The solid line represents a hyperbolic tangent function which was manually fitted to the experimental data points to guide the eye.	46
5.2	The heterogeneous activation probability curve of 7nm sodium chloride particles at $-0, 1^{\circ}C$ determined by the experimental data points which are represented by the circular symbols. Every measurement set is illustrated by a different color. At activation probabilities $P_{act} = [0; 50; 100] \%$ dashed lines are included for better orientation. The solid line represents a hyperbolic tangent function which was manually fitted to the experimental data points to guide the eye.	47
5.3	The heterogeneous activation probability curve of 7nm sodium chloride particles at $+9, 9^{\circ}C$ determined by the experimental data points which are represented by the triangular symbols. Every measurement set is illustrated by a different color. At activation probabilities $P_{act} = [0; 50; 100] \%$ dashed lines are included for better orientation. The solid line represents a hyperbolic tangent function which was manually fitted to the experimental data points to guide the eye. The early total activation of the particles for some of the sets is discussed in this section.	48
5.4	Superposition of figures 5.1, 5.2 and 5.3.	49
5.5	The heterogeneous activation probability curve of 10nm sodium chloride particles at $-10, 1^{\circ}C$ determined by the experimental data points which are represented by the star-shaped symbols. Every measurement set is illustrated by a different color. At activation probabilities $P_{act} = [0; 50; 100] \%$ dashed lines are included for better orientation. The solid line represents a hyperbolic tangent function which was manually fitted to the experimental data points to guide the eye.	51

5.6	The heterogeneous activation probability curve of 10nm sodium chloride particles at $+9, 8^{\circ}C$ determined by the experimental data points which are represented by the triangular symbols. Every measurement set is illustrated by a different color. At activation probabilities $P_{act} = [0; 50; 100] \%$ dashed lines are included for better orientation. The solid line represents a hyperbolic tangent function which was manually fitted to the experimental data points to guide the eye.	52
5.7	Superposition of figures 5.5 and 5.6.	53
5.8	The heterogeneous activation probability curve of 15nm sodium chloride particles at $-10, 3^{\circ}C$ determined by the experimental data points which are represented by the star-shaped symbols. Every measurement set is illustrated by a different color. At activation probabilities $P_{act} = [0; 50; 100] \%$ dashed lines are included for better orientation. The solid line represents a hyperbolic tangent function which was manually fitted to the experimental data points to guide the eye.	55
5.9	The heterogeneous activation probability curve of 15nm sodium chloride particles at $-0, 1^{\circ}C$ determined by the experimental data points which are represented by the circular symbols. At Every measurement set is illustrated by a different color. activation probabilities $P_{act} = [0; 50; 100] \%$ dashed lines are included for better orientation. The solid line represents a hyperbolic tangent function which was manually fitted to the experimental data points to guide the eye.	56
5.10	The heterogeneous activation probability curve of 15nm sodium chloride particles at $+9, 7^{\circ}C$ determined by the experimental data points which are represented by the triangular symbols. Every measurement set is illustrated by a different color. At activation probabilities $P_{act} = [0; 50; 100] \%$ dashed lines are included for better orientation. The solid line represents a hyperbolic tangent function which was manually fitted to the experimental data points to guide the eye.	57
5.11	Superposition of figures 5.8, 5.9 and 5.10.	58

5.12	The colored lines depict the Kelvin curves showing the critical particle diameter at the critical saturation ratio S which were calculated at $+10^\circ$, 0° and -10° . The experimental data points show the seed particle diameter and the saturation ratio at which half of all seed particles are activated. The error of D_P was statistically determined whereas the error of S was calculated from the geometric standard deviation σ of D_P using the Kelvin equation (see tables 5.2.1 to 5.2.3). Further, the abscissa is in logarithmic scale.	60
5.13	The cross section of a critical cluster of radius r^* (obtained using the Kelvin equation) containing a seed particle of diameter D . Due to the contact angle which is 0° between the n-nonane cluster and the NaCl seed particle surface the seed is totally covered with the liquid. The grey area stands for the seed particle whereas the white area depicts the liquid droplet.	61
5.14	The experimentally determined onset saturation for a seed particle featuring diameter D enables the determination of the critical droplet diameter d^* . By way of illustration an experimental data point was picked randomly.	62
5.15	The onset saturation ratio at which a seed particle of diameter D is activated combined with the solution of the Kelvin equation at the onset saturation allows the determination of the molecule number in the critical cluster. The experimentally obtained data points for constant nucleation temperatures are linked with dashed lines to guide the eye.	63
5.16	The number of molecules in the critical cluster versus nucleation temperature is plotted. The black squares stand for the experimentally investigated seed particle radii. They are linked with dashed lines for better illustration of the temperature trend.	64
5.17	The number of molecules in the critical cluster versus nucleation temperature is plotted. The black squares stand for the experimentally investigated seed particle radii. They are linked with dashed lines for better illustration of the temperature trend.	65
5.18	The number of molecules in the critical cluster versus nucleation temperature is plotted. The black squares stand for the experimentally investigated seed particle radii. They are linked with dashed lines for better illustration of the temperature trend.	66
5.19	Front page of the Fletcher calculation program.	69

5.20	From the results of the Fletcher calculations the program compiles a table(the values in the table shown above are arbitrary). The calculation may be viewed step by step optionally. Further, there is the possibility to download the data.	70
5.21	The Fletcher curves which are represented by the solid lines calculated with the programmed software are compared with Kelvin curves (dashed lines). Therefore nucleation temperatures entered in the equations were chosen equally to experimental. Both Kelvin and Fletcher curves were calculated for $-10, 2^{\circ}C$, $-0, 1^{\circ}C$ and $+9, 8^{\circ}C$. The curves at high temperatures are illustrated by red color, the ones for $-0, 1^{\circ}C$ are represented by the black lines and the blue lines stand for $-10, 2^{\circ}C$	73
5.22	The saturation ratio S is plotted versus the seed particle diameter D_P . The solid line depicts the Fletcher curve calculated for a nucleation temperature of $-10, 2^{\circ}C$, the dashed line for the Kelvin curve at the same temperature. The black stars show the experimentally obtained data points, also for $-10, 2^{\circ}C$. The abscissa is logarithmically scaled.	74
5.23	The saturation ratio S is plotted versus the seed particle diameter D_P . The solid line depicts the Fletcher curve calculated for a nucleation temperature of $-0, 1^{\circ}C$, the dashed line for the Kelvin curve at the same temperature. The black stars show the experimentally obtained data points, also for $-0, 1^{\circ}C$. The abscissa is logarithmically scaled.	75
5.24	The saturation ratio S is plotted versus the seed particle diameter D_P . The solid line depicts the Fletcher curve calculated for a nucleation temperature of $9, 8^{\circ}C$, the dashed line for the Kelvin curve at the same temperature. The black stars show the experimentally obtained data points, also for $9, 8^{\circ}C$. The abscissa is logarithmically scaled.	76

Appendix:

The main part of the Fletcher program's source code which was used to calculate onset saturation ratios (see chapter 5).

```

<!DOCTYPE html PUBLIC "-//W3C//DTD XHTML 1.0 Transitional//EN" "http://www.w3.org/TR/xhtml1/DTD/xhtml1-transitional.dtd">
<html xmlns="http://www.w3.org/1999/xhtml">
<head>
<meta http-equiv="Content-Type" content="text/html; charset=utf-8" />
<title>Untitled Document</title>
<script src="jquery.js"></script>
<script src="jquery.form.js"></script>

<script>
$(document).ready(function()
{

});

function showCalc() {
    $('#debug .content').slideToggle('fast');
}
</script>

<style type="text/css">
#tabelle {
background-color: #DDD;
width: 500px;
}
.style1 {
color: #FFF;
}
.btn {
color: #FFF;
background-color: #CCC;
height: 20px;
width: 200px;
border: 1px inset #333;
padding: 5px;
background-image: url(btn.jpg);
font-family: Verdana, Geneva, sans-serif;
text-decoration: none;
font-size: 10px;
font-weight: bold;
}
#container {
width: 650px;
margin-right: auto;
margin-left: auto;
margin-top: 80px;
}
#container #header {
font-family: Verdana, Geneva, sans-serif;
font-size: 24px;
font-style: italic;
color: #000;
margin-top: 20px;
margin-bottom: 20px;
}

```

```

file {
margin-top: 20px;
}
#tabelle {
margin-top: 20px;
margin-bottom: 20px;
}
#container #tabelle .title {
font-family: Verdana, Geneva, sans-serif;
font-size: 16px;
font-weight: bold;
color: #FFF;
background-image: url(btn.jpg);
padding: 5px;
border: 1px solid #333;
}
</style>
</head>

<body>
<div id="container">
<div id="header">RESULTS</div>
<div id="debug">
<div class="title"><a id="btn_calc" href="#" class="btn" onclick="showCalc();">Show/Hide Calculation</a></div>
<div class="content" style="display: none;">
  <?

//Auslesen der Eingaben-----
$temp = $_POST["temp"];           //Nukleationstemperatur
$kin = $_POST["kin"];             //bei manueller Eingabe Vorfaktor des kin. Faktors
$kin2 = $_POST["kin2"];          // Exponent bei Basis 10 für kin Faktor
$mol = $_POST["mol"];            // Molmasse der Flüssigkeit in g/mol
$nuk = $_POST["nuk"];            //Nukleationszeit
$winkel = $_POST["winkel"];      //Kontaktwinkel
$aktiv = $_POST["aktiv"];        //Aktivierungswahrscheinlichkeit

$dichte = $_POST["dichte"];       //Dichte der Flüss.
$spannung = $_POST["spannung"];   //Oberflächenspannung

//Eingaben für Algorithmus:
$xa = $_POST["xa"];              //untere Schranke
$xb = $_POST["xb"];              //obere Schranke
$dx = $_POST["dx"];              //Schrittweite
$rseed = $_POST["rseed"];        //Startwert Seed

$kinmodus = $_POST["kinmodus"];   //Kinetischen Faktor berechnen oder manuell eingeben
$jsigma = $_POST["jsigma"];       //Sigma von Lennard Jones
$jepsilon = $_POST["jepsilon"];   //Epsilon von Lennard Jones
$dampfdruck = $_POST["dampfdruck"]; //Dampfdruck der Flüssigkeit
$latentew = $_POST["latentew"];   //Latente Wärme
$stock = $_POST["stock"];         //Stockmayr Potential

```

```

// -----
// Es werden simultan (für die Übersättigung) zwei Berechnungen durchgeführt:
// -mit Gleitkommadarstellung (Genauigkeit ca. 8 Stellen)
// -über String mit beliebiger Genauigkeit
// typischerweise wird eine Variable in Gleitkommadarstellung mit $x bezeichnet und in String-Form mit $xx
// -----

// -----VARIABLEN DEFINITION -----

$genauigkeit = $_POST["genauigkeit"]; //Anzahl der Stellen für Berechnung mit Strings
$gen = '80';
bcscale($gen); //legt die Genauigkeit für die Stringfunktionen global fest

$winkel = bcdiv($winkel, '360');
$winkel = bcmul($winkel, bcmul('2', M_PI));
$sigma = $spannung;
$k = bcmul('1.380650424', bcpow('10', '-23')); //boltzmann
// $k = bcmul('1.381', bcpow('10', '-23')); //boltzmann Kulmala
$T = $temp;
$N = bcmul('6.0221417930', bcpow('10', '23')); //avogadro
// $N = bcmul('6.024096386', bcpow('10', '23')); //avogadro kulmala

$M = $mol; //in g/mol
$rho = $dichte; //in g/m^3
$phi = $winkel; //in rad
$R = $rseed; //in m
$RR = $rseed; //neu //in m
$ps = $aktiv;
$dt = $nuk; //in s
$x = ix;

//KINETIK VARIABLEN
$SIGMA = bcmul($sigma, bcpow('10', '-10'));
$epsilon = $jepsilon;
$epsilon = bcmul($epsilon, $k);
$ps = $dampfdruck;
$latente = $latentew;
$JL = bcmul($latente, bcdiv($M, $N)); //umrechnen der latenten wärme von kj/kg in J/molekül
if($skinmodus=="man") { $K = bcmul(bcmul($kin, bcpow('10', $kin2)), bcpow('100', '2')); } //K in SI umwandeln!

//AUSGABE DER EINGABEN:
echo "variables: <br>
-----<br>
Lennard Jones potential:<br>
SIGMA: SIGMA=$SIGMA m<br>
epsilon: epsilon=$epsilon J<br> <br>
constants:<br>
boltzmann k=$k J/K<br>
avogadro N=$N<br><br>
Variables:<br>
vapor pressure: ps=$ps Pa<br>

```

latent heat: latentew=\$latentew KJ/kg

 molar mass: M=\$M g

 density: rho=\$rho g/m^3

 contact angle: phi=\$phi radian measure

 seed particle radius: R=\$R m

 activation probability: p=\$p

 nucleation time: dt=\$dt s

;

\$index = 0;

```
// -----SCHLEIFE FÜR X-----
for($ix = bcadd($xa, '0'); $ix<=$xb; $ix=bcadd($ix, $dx))
{
  $x = bcadd($ix, '0');
  $countx = ($x - $xa + $dx)/$dx;
  echo "<br>
-----<br />
values X: $x <br>
phi: $phi <br>
-----<br />
<br>";
```

```
// -----FORMEL-f-Faktor-----
// Der f-Faktor beschreibt den Einfluss des Kontaktwinkels auf die Keibildungsenergie
// Hab f getestet für extremwerte, für 60° bei x=1 und mit Fletcher verglichen! Hat gepasst!
```

\$m=cos(\$phi);
 \$m=bcdiv(\$m, '1');

//\$g = sqrt(1+ pow(\$x,2) - 2*\$x*\$m) (so solls funktionieren)

\$g = bcpow(\$x, '2');
 \$g = bcadd('1', \$g);
 \$g = bcsub(\$g, bcmul('2', bcmul(\$x, \$m)));
 \$g = bcsqrt(\$g);

\$ff = bcpow(bcdiv(bcsub('1', bcmul(\$x, \$m)), \$g), '3');
 \$ff = bcadd('1', \$ff);
 \$f = 1 + pow((1-\$x*\$m)/\$g, 3);
 \$k = bcdiv(bcsub(\$x, \$m), \$g);
 \$ff = bcadd(\$ff, bcmul(bcpow(\$x, '3'), bcsub('2', bcsub(bcmul('3', bcdiv(bcsub(\$x, \$m), \$g)), bcpow(\$k, '3')))));
 \$f = \$f + pow(\$x, 3) * (2 - 3*((\$x-\$m)/\$g) + pow((((\$x-\$m)/\$g), 3));
 \$ff = bcadd(\$ff, bcmul('3', bcmul(\$m, bcmul(bcpow(\$x, '2'), bcsub(bcdiv(bcsub(\$x, \$m), \$g), '1')))));
 \$f = \$f + 3*\$m*pow(\$x, 2) * ((\$x-\$m)/\$g - 1);
 \$ff = bcdiv(\$ff, '2');
 \$f = \$f*0.5; //Hab ich mit Taschenrechner nachgerechnet!! für x=0.5 und m=0.2 =>
 f=0.857408523

```

echo "
f-factor(including x=R/r and contact angle):<br>
f=$f<br>
ff=$ff<br><br>";

//-----FORMEL-KINETIK-----
// Berechnet den kinetischen Faktor K

if($skinmodus=="calc") { //ausführen, falls berechnen des kin. Faktors gewählt wurde!
$X = bcdiv('1', '6');
$X = pow(2, $X);
$V = bcpow($SIGMA, '2');
$V = bcsb(bcdiv('156', bcmul(bcpow($X,'14'), $V)), bcdiv('42', bcmul(bcpow($X, '8'), $V)));
$V = bcmul($V, bcmul('4', $epsilon));
//zweite Ableitung des Potentials bei Gleichgewichtsabstand

$mmu = $M;
$mmu = bcdiv(bcdiv($mmu, $N), '1000');
//umrechnen von g/mol in kg/molekül
$mmu = bcdiv(bcmul($mmu, $mmu), bcadd($mmu, $mmu));
//reduzierte Masse von 2 Molekülen!!
$nuu = bcdiv(bcsqrt(bcdiv($V, $mmu)), bcmul('2', M_PI));
//Frequenz der Schwingung im LJ-Potential
$nu = bcmul(bcdiv('1', '1.13'), bcpow('10','12'));

$R=$rseed;
//setze R=Eingabe (Gleitkommaform der Variable)
$RR = $rseed;
//setze RR=Eingabe (Stringform der Variable)
$rr=bcdiv($R, $x);
//Durchmesser des krit. Radius aus Eingabe von R
$r=$rr;
$S = bcdiv(bcmul('2', bcmul($sigma, $M)), bcmul($rho, bcmul($N, bcmul($k, bcmul($T, $rr))));
//muss hier eine 1. Schätzung für S angeben (Kelvin)
$S = pow(M_E, $S);
//2. Teil der Schätzung

$d = bcsqrt(bcadd(bcpow($R, '2'), bcsb(bcpow($r, '2'), bcmul('2', bcmul($r, bcmul($R, $m))))));
//(R*R - r*r - 2rRm)exp(1/2)
$cospsi = bcmul('-1', bcdiv(bcsb($rr, bcmul($RR, $m)), $d));
$FI = bcmul('2', bcmul(M_PI, bcmul(bcpow($rr, '2'), bcsb('1', $cospsi)));
//Oberfläche des Tröpfchens, hab ich mit Hilfe des Extremfalls R=0 bzw phi=0 verifiziert!

$ab = bcmul($k, bcdiv(bcdiv($M, $N), '1000'));
$Nads = bcdiv(bcmul($S, $ps), bcsqrt(bcmul('2', bcmul(M_PI, bcmul($T, $ab))));
//bei Nads und beta ist die masse in kg pro Molekül angegeben!!
$Nads = bcmul($Nads, bcdiv(pow(M_E, bcdiv($L, bcmul($k, $T))), $nu));

//surface concentration of adsorbed molecules
$ppp = bcmul(M_PI, bcmul($rho, bcmul($N, bcpow($rr, '2')));
$Z = bcmul(bcsqrt(bcdiv($sigma, bcmul($k, $T))),bcdiv($M, bcmul('2', $ppp)));
//Zeldovich Faktor
$beta = bcdiv(bcmul($S, bcmul($ps,$FI)),bcsqrt(bcmul('2', bcmul($T, bcmul(M_PI, $ab))));
//impingement rate

$K = bcmul($beta, bcmul($Z, $Nads));
//kinetischer Faktor, wie im Science Paper
}

```

```

//-----FORMEL-FLETCHER-RADIUS-----
// Hier hab ich zuerst alles in gleitkommadarstellung eingetippt,
// aber dann hab ich an der Genauigkeit gezweifelt
// Hab dann alles nochmals in Stringform eingegeben! Einzige Schwäche:
// Stringform lässt nur Ganzzahlige Exponenten zu!
// Deshalb: Bei Berechnung des Sättigungsverhältnisses geht die ganze Genauigkeit wieder verloren,
// sollte aber nicht so schlimm sein

$UU = bcmul('16', bcmul(bcdiv(M_PI, '3'), bcpow(bcdiv($sigma, bcmul($k, $T)), '3')));
$U = (16*M_PI/3) * pow(($sigma/($k*$T)),3);
$UU = bcmul($UU, bcpow(bcdiv($M, bcmul($N, $rho)), '2'));
$U = $U * pow(($M/($N*$rho)),2);
$bc = bcmul(M_PI, bcmul($K, bcmul($dt, bcpow($RR, '2'))));
$UU = bcmul($ff, bcmul($UU, bcdiv('1', log(bcdiv(bcmul('4', $bc), log(bcdiv('1', bcsb('1', $p))))))));
$U = $f * $U * 1/(log( (4*M_PI*pow($R,2)*$K*$dt) / log(1/(1-$p))));

$SS = pow(M_E, bcsqrt($UU));
$S = pow(M_E, sqrt($U));
$rr = bcdiv(bcmul('2', bcmul($sigma, $M)), bcmul($rho, bcmul($N, bcmul($k, bcmul($T, log($SS))))));
$R = (2*$sigma*$M)/($rho*$N*$k*$T*log($S));
$RR = bcmul($x, $rr);
$R = $x*$R;

//-----SCHLEIFE-----
// Die ganze Prozedur von oben wird nun so lange wiederholt bis: zur Zeit: 10mal,
// ändere ich aber noch auf anderes Kriterium
// einzig der f-Faktor ändert sich nicht

for($i=0;$i<10;$i++){

if($kinmodus=="calc") { //kinetischer Faktor
$X = bcdiv('1', '6');
$X = pow(2, $X);
$V = bcpow($SIGMA, '2');
$V = bcsb(bcdiv('156', bcmul(bcpow($X, '14'), $V)), bcdiv('42', bcmul(bcpow($X, '8'), $V)));
$V = bcmul($V, bcmul('4', $epsilon));
//zweite Ableitung des Potentials bei Gleichgewichtsabstand
$mmu = $M;
$mmu = bcdiv(bcdiv($mmu, $N), '1000');
//umrechnen von g/mol in kg/molekül
$mmu = bcdiv(bcmul($mmu, $mmu), bcadd($mmu, $mmu));
//reduzierte Masse von 2 Molekülen!
$nu = bcdiv(bcsqrt(bcdiv($V, $mmu)), bcmul('2', M_PI));
$nuu = bcmul(bcdiv('1', '1.13'), bcpow('10', '12'));
//Frequenz der Schwingung im LJ-Potential

$d = bcsqrt(bcadd(bcpow($RR, '2'), bcsb(bcpow($rr, '2'), bcmul('2', bcmul($rr, bcmul($RR, $m))))));
//(R*R - r*r - 2rRm)exp(1/2)
$cospsi = bcmul('-1', bcdiv(bcsb($rr, bcmul($RR, $m)), $d));

```

```

$Fl = bcmul('2', bcmul(M_PI, bcmul(bcpow($rr, '2'), bcsb('1', $cospsi))));
//Oberfläche des Tröpfchens, hab ich mit Hilfe des Extremfalls R=0 bzw phi=0 verifiziert!

```

```

$Nads = bcdiv(bcmul($S, $ps), bcsqrt(bcmul('2', bcmul(M_PI, bcmul($T, $ab))));
//bei Nads und beta ist die masse in kg pro Molekül angegeben!!
$Nads = bcmul($Nads, bcdiv(pow(M_E, bcdiv($L, bcmul($k, $T))), $nu));

```

```

//surface concentration of adsorbed molecules
$cd = bcmul('2', bcmul(M_PI, bcmul($rho, bcmul($N, bcpow($rr, '2'))));
$Z = bcmul(bcsqrt(bcdiv($sigma, bcmul($k, $T))), bcdiv($M, $cd));
//Zeldovich Faktor
$beta = bcdiv(bcmul($S, bcmul($ps, $Fl)), bcsqrt(bcmul('2', bcmul($T, bcmul(M_PI, $ab))));
//impingement rate

```

```

$K = bcmul($beta, bcmul($Z, $Nads));
}

```

```

//AUSGABE: _____

```

```

echo "<br>
beta=$beta 1/s<br>
Nads=$Nads 1/m^2<br>
Z=$Z<br>
kinetic factor K=$K 1/(sm^2)
";

```

```

$UU = bcmul('16', bcmul(bcdiv(M_PI, '3'), bcpow(bcdiv($sigma, bcmul($k, $T)), '3')));
$U = (16*M_PI/3) * pow(($sigma/($k*$T)),3);
$UU = bcmul($UU, bcpow(bcdiv($M, bcmul($N, $rho)), '2'));
$U = $U * pow(($M/($N*$rho)),2);
$Uc = bcpow($RR, '2');
$Ub = bcmul('4', bcmul(M_PI, bcmul($K, bcmul($dt, $Uc))));
$Ua = log(bcdiv($Ub, log(bcdiv('1', bcsb('1', $p))));
$UU = bcmul($ff, bcmul($UU, bcdiv('1', $Ua)));
$U = $f * $U * 1/(log( (4*M_PI*pow($R,2)*$K*$dt) / log(1/(1-$p))));
//die ganze U und S und r sache hab ich mit Taschenrechner nachgerechnet und passt!

```

```

$SS = pow(M_E, bcsqrt($UU));
$S = pow(M_E, sqrt($U));

```

```

$rr = bcdiv(bcmul('2', bcmul($sigma, $M)), bcmul($rho, bcmul($N, bcmul($k, bcmul($T, log($SS))));
$r = (2*$sigma*$M)/($rho*$N*$k*$T*log($S));
$RR = bcmul($x, $rr);
$R = $x*$r;

```

```

echo "<br>
saturation ratio:<br>
S=$S<br>
SS=$SS<br>

```

```

Kelvin radius:<br>
rr=$rr m<br>
r=$r m<br>
Fletcher radius:<br>
R=$R m<br>
RR=$RR m<br>
";

} // Ende Näherung

// Array -> Ausgabe

$results[$index]["R"] = $R*pow(10,9);
$results[$index]["r"] = $r*pow(10,9);
$results[$index]["S"] = $S;
$index = $index+1;

} // ENDE x-SCHLÖEIFE

?>
</div>
</div>

<div id="tabelle">
<div class="title">VALUES</div>
<table width="100%" border="0" cellspacing="1" cellpadding="1">
<tr class="style1">
<td width="32%" align="center" bgcolor="#666666"><strong>r [nm]</strong></td>
<td width="41%" align="center" bgcolor="#666666"><strong>R [nm]</strong></td>
<td width="27%" align="center" bgcolor="#666666"><strong>S</strong></td>
</tr>

<? for($i=0;$i<count($results);$i++)
{
?>
<tr>
<td><? echo $results[$i]["r"];?></td>
<td><? echo $results[$i]["R"];?></td>
<td><? echo $results[$i]["S"];?></td>
</tr>
<?
}
?>

</table>
</div>

<div id="file">
<div class="title"><a class="btn" href="results.dat">DOWNLOAD results.dat FILE</a></div>
<div id="filedownload" class="content">
<?
$fp = fopen("results.dat","w");
fclose($fp);
$fp = fopen("results.dat","a");
foreach($results as $item)

```

```
{
  $str = implode(",",$item);
  $str = $str."\n";
  fwrite($fp,$str);
}
fclose($fp);

?></div>
</div>
</div>

</body>
</html>
```

Curriculum Vitae

Lukas Pichelstorfer
Hechtstr. 52
5201 Seekirchen

Phone: 0650/5588447
Lukas.pichelstorfer@univie.ac.at

Date of birth: 1.12.1985
Place of birth: Oberndorf, Salzburg



Education

1992-1996	Volksschule Seekirchen
1996-2004	Bundesgymnasium Seekirchen (secondary school)
from 2005	Student of physics

Further education

6. – 12. Juli 2009:	Vienna Summer School “Basic Aerosol Science“
10. – 14. August 2009:	Participation at the 18 th International Conference “ Nucleation and Atmospheric Aerosols”

Professional experience

Seit WS 2008/2009	Tutor
2004-2005	Civilian service (Lebenshilfe Salzburg)